



Reza Allahvirdizadeh Modelling of the seismic behaviour of TRM-strengthened rammed earth walls

Portugal | 2017



ADVANCED MASTERS IN STRUCTURAL ANALYSIS OF MONUMENTS AND HISTORICAL CONSTRUCTIONS

# Master's Thesis

Reza Allahvirdizadeh

Modelling of the seismic behaviour of TRM-strengthened rammed earth walls



University of Minho



University of Padova



Education and Culture

## Erasmus Mundus





ADVANCED MASTERS IN STRUCTURAL ANALYSIS  
OF MONUMENTS AND HISTORICAL CONSTRUCTIONS



# Master's Thesis

**Reza Allahvirdizadeh**

**Modelling of the seismic behaviour of  
TRM-strengthened rammed earth walls**

This Masters Course has been funded with support from the European Commission. This publication reflects the views only of the author, and the Commission cannot be held responsible for any use which may be made of the information contained therein.

## DECLARATION

Name: Reza Allahvirdizadeh  
Email: allahvirdizadeh@gmail.com

Title of the M.Sc. Dissertation: Modelling of the seismic behaviour of TRM-strengthened rammed earth walls

Supervisor(s): Daniel V. Oliveira, Rui A. Silva

Year: 2017

I hereby declare that all information in this document has been obtained and presented in accordance with academic rules and ethical conduct. I also declare that, as required by these rules and conduct, I have fully cited and referenced all material and results that are not original to this work.

I hereby declare that the MSc Consortium responsible for the Advanced Masters in Structural Analysis of Monuments and Historical Constructions is allowed to store and make available electronically the present MSc Dissertation.

University: Universidade do Minho  
Date: July 17<sup>th</sup>, 2017  
Signature: \_\_\_\_\_

This page is left blank on purpose.

*To Negar for her endless love  
and to my parents for their unwavering kindness and support*

This page is left blank on purpose.

## ACKNOWLEDGMENTS

This present work was developed within the framework of SAHC Erasmus Mundus Master Course ([www.msc-sahc.org](http://www.msc-sahc.org)) and the project of POCI-01-0145-FEDER-016737 (PTDC/ECM-EST/2777/2014), financed by FEDER funds through the Competitvity Factors Operational Programme - COMPETE and by national funds through FCT – Foundation for Science and Technology. They are both kindly acknowledged.

I would like to thank Professor Oliveira for giving me this unforgettable chance to cooperate with them on this incredible project and for his trust and belief in my abilities. His calm, kindness and support encouraged me to do my best during all tough moments, which made this work a forever lasting valuable experience.

I also would like to thank Dr. Rui Silva for his kindness, patience and constant support. He always replied my questions and dedicated many times for me to solve issues. I believe that without his guidance, there was no way to finish this work.

I want to thank the Consortium for the amazing privilege of receiving the scholarship that allowed me to attend the SAHC program. This experience deeply changed me, not only from professional point of view, but mainly personally, in the way I learnt how to approach team-work and sharing different points of view.

I would like to thank all my friends both in Padova and Guimarães. Living and working with all of them made hard moments of last year to be tolerable and they are all now friends forever. I really learned a lot from all of them. My special thank should go to Giwrgos Vlahakis for all our discussions, tea times and for his great personality, to Ali Haghi a friend who was always supportive, kind and a good listener and to Georgios Zarmboutis and Francesca Contrafatto for all their kindness and help.

Finally, I would like to thank Negar. Without her supports and sacrifices, it was not possible for me even to start the program; and to my parents who always encourage me and picture a better future; and to my family, who their love is the best reason to live.



This page is left blank on purpose.

## ABSTRACT

Earthen constructions constitute a considerable part of the existing heritage and a large percentage of the World population is still living or working in buildings built with this structural system. Like other types of masonry structures, rammed earth constructions are acceptably stable under gravity loads, although they are significantly vulnerable to earthquakes. Therefore, a precise understanding of their behavior in case of being subjected to ground motions and the proposing of effective strengthening techniques achieved a great interest both in research and practice. Strengthening methods should be not only to enhance capacity and ductility of the building, but also to satisfy a variety of criteria such as being compatible with the substrate, economical and reversible. Considering all, the low-cost textile reinforced mortar (LC-TRM) strengthening is introduced, and its efficiency on rammed earth walls is studied numerically in the present thesis.

In the current study, the seismic performance of both unstrengthened and strengthened rammed earth structural components is investigated. In this regard, in-plane and out-of-plane behaviors are studied by means of different constructed nonlinear finite element models. At first, pushover analysis by mass-based lateral load pattern is conducted on unstrengthened walls to evaluate their capacity and understand possible failure mechanisms. Furthermore, the outcomes of these analyses are employed to select the most proper modeling approach from shell or solid elements and the walls with appropriate geometrical dimensions. In the following, pushover analyses are conducted on strengthened walls to choose between different strengthening materials and assess the effectiveness of the adopted strengthening technique. Furthermore, the frequency change of the walls with the damage states (lateral displacement levels) is studied to represent the initiation and propagation of damage in unstrengthened walls and to evaluate the effectiveness of TRM strengthening method.

Finally, an artificially generated ground motion record was applied to both unstrengthened and strengthened walls to perform nonlinear time-history analyses. The outcomes were used to compare the dynamic behavior of the walls against the results of the pushover analyses.

**Keywords:** *Rammed earth, TRM strengthening, FEM modeling, Pushover analysis, Nonlinear time-history analysis, In-plane behavior, Out-of-plane behavior*

This page is left blank on purpose.

## RESUMO

As construções de terra constituem uma parte considerável do património construído e uma grande parte da população mundial ainda vive ou trabalha em edifícios construídos com este sistema estrutural. Como outros tipos de estruturas de alvenaria, as construções de terra são estáveis face a cargas gravíticas, embora sejam significativamente vulneráveis a sismos. Portanto, a compreensão do seu comportamento perante a ocorrência de movimentos do solo e a proposta de técnicas efetivas de reforço despertam um grande interesse, tanto a nível da investigação como na prática. Os métodos de reforço devem ser adequados não só para aumentar a capacidade e a ductilidade da construção, mas também para satisfazer uma variedade de critérios, como a compatibilidade com o substrato, custo económico e reversibilidade. Considerando todos estes aspetos, apresenta-se uma técnica baseada em argamassa reforçada com malhas têxteis de baixo custo (LC-TRM), cuja eficiência em paredes de terra é estudada na presente tese do ponto de vista numérico.

No presente trabalho, investiga-se o desempenho sísmico de componentes estruturais de taipa não reforçados e reforçados. A este respeito, estudam-se os comportamentos no plano e fora do plano, por meio de diferentes modelos de elementos finitos não lineares. Em primeiro lugar, realiza-se a análise pushover proporcional à massa em paredes não reforçadas para avaliar sua capacidade e compreender possíveis mecanismos de colapso. Adicionalmente, estes resultados são utilizados para selecionar a técnica de modelação mais apropriada (elementos de casca ou sólidos) e as dimensões geométricas mais apropriadas. De seguida, realiza-se a análise pushover em paredes reforçadas para escolher de entre diferentes materiais de reforço e avaliar a eficácia da técnica de reforço adotada. Além disso, a variação das frequências das paredes com os estados de dano (níveis de deslocamento lateral) é estudada para identificar o início e a propagação de dano em paredes não reforçadas e avaliar a estabilidade do método de reforço baseado na técnica TRM.

Finalmente, selecionou-se um registro sísmico artificial para realizar análises temporais não lineares de paredes simples e reforçadas. Os resultados são utilizados para comparar o comportamento dinâmico das paredes com os resultados da análise pushover.

**Palavras-chave:** *Taipa, Reforço com TRM, Modelação MEF, Análise pushover, Análise temporal não linear, Comportamento no plano, Comportamento para fora do plano*

This page is left blank on purpose.

## چکیده

سازه‌های ساخته شده از خاک بخش قابل توجهی از بناهای تاریخی موجود را تشکیل می‌دهند. از سوی دیگر هنوز جمعیت کثیری از مردم جهان در ساختمان‌هایی از این دست زندگی کرده و یا مشغول فعالیت هستند. سازه‌های ساخته شده از تراکم کردن خاک<sup>۱</sup> همانند دیگر انواع سازه‌های بنایی از توانایی قابل قبولی در انتقال بارهای ثقلی برخوردارند، ولی عملکرد آنها تحت اثر بارهای لرزه‌ای دارای نقاط ضعیف عدیده‌ای است. از اینرو و در سال‌های اخیر، فهم دقیق و صحیح از رفتار این قبیل سازه‌ها تحت اثر بارهای لرزه‌ای و ارائه روش‌های مقاوم‌سازی مناسب برای آنها، توجه بسیاری از محققین و فعالان این حوزه را به خود جلب نموده است. اهمیت تاریخی درصد قابل توجهی از سازه‌های از این دست، منجر به ارائه معیارهای متعددی بمنظور پذیرش روش‌های مقاوم‌سازی پیشنهادی شده است. این ضوابط شامل افزایش ظرفیت باربری و شکل‌پذیری سازه، سازگاری (هم از نظر فیزیکی و هم از نظر شیمیایی) با مصالح موجود، اقتصادی بودن و قابلیت برگشت‌پذیری آن بدون آنکه آسیبی به ماهیت اصلی سازه وارد آورد، می‌باشند. یکی از روش‌های شدت در حال گسترش، استفاده از ملات‌های ارزان قیمت مسلح شده توسط الیاف<sup>۲</sup> است. مطالعه حاضر شامل بررسی عددی کارایی این روش در دیوارهای ساخته شده به روش تراکم کردن خاک می‌باشد.

در این مطالعه، عملکرد لرزه‌ای این دیوارها در حالات ساده و تسلیح شده بررسی شده است. در این راستا، رفتار درون صفحه و برون صفحه آنها توسط مدل‌های اجزای محدود ساخته شده، مورد مطالعه قرار گرفت. ابتدا، تحلیل استاتیکی غیرخطی (بارافزون) با الگوی بار جانبی متناسب با جرم دیوار بر روی دیوارهای ساده انجام شد. نتایج این تحلیل‌ها منجر به برآورد ظرفیت بار جانبی آنها و نیز شناسایی مودهای محتمل تخریب گردید. علاوه بر این، از نتایج این تحلیل‌ها جهت انتخاب مناسب‌ترین شیوه مدلسازی از میان مدل‌های مختلف ساخته شده با المان‌های پوسته یا مکعبی استفاده شد. از سوی دیگر و از آنجایی که نمونه‌ای از دیوارهای مورد مطالعه در این نوشتار در آینده نزدیک بر روی میز لرزه آزمایش خواهند گردید؛ بنابراین، از نتایج تحلیل‌های بارافزون جهت انتخاب مناسب‌ترین ابعاد این دیوارها بهره گرفته شد. این ابعاد باید بگونه‌ای تنظیم می‌گردیدند که تضمین‌کننده مواردی چون شرایط واقعی ساخت، محدودیت‌های میز لرزه و نیز مودهای شکست مورد انتظار باشند. در ادامه تحلیل‌های بارافزون بر روی دیوارهای مقاوم‌سازی شده نیز انجام گردید. نتایج این تحلیل منجر به انتخاب بهترین گزینه از این میان دو مصالح مدنظر و بررسی

<sup>1</sup> Rammed earth buildings

<sup>2</sup> Low-cost textile reinforced mortar (LC-TRM)

کارایی این شیوه در بهبود عملکرد لرزه‌ای دیوارها گردید. در ادامه، تغییرات فرکانس دیوارها و مشخصات دینامیکی آنها (مانند جرم موثر هر مود ارتعاش) در تغییر مکان‌های جانبی مختلف بررسی گردید تا میزان خسارات وارده بر دیوارها و نیز پایداری روش مقاوم‌سازی استفاده شده، مشخص گردد.

در نهایت، تحلیل غیرخطی تاریخچه زمانی بر روی مدل‌های ساخته شده در هر دو حالت مقاوم‌سازی شده و ساده تحت اثر یک رکورد زلزله مصنوعی انجام گردید. این رکورد زلزله براساس شرایط زمین‌شناختی جنوب پرتغال و نیز معیارهای آیین‌نامه زلزله این کشور تولید شده است. شایان ذکر است منطقه اخیر دارای نمونه‌های متعددی از ساختمان‌هایی با سیستم مورد بررسی در این نوشتار می‌باشد. در ادامه، نتایج این تحلیل جهت مقایسه پاسخ‌های استاتیکی و دینامیکی دیوارها مورد استفاده قرار گرفت.

**کلیدواژه:** سازه‌های خاکی ساخته شده از تراکم خاک، مقاوم‌سازی با ملات‌های تسلیح شده با الیاف، مدل‌سازی اجزای محدود،

تحلیل بارافزون، تحلیل غیرخطی تاریخچه زمانی، رفتار درون صفحه، رفتار برون صفحه

## TABLE OF CONTENTS

<b>Chapter 1 Introduction .....</b>	<b>1</b>
1.1. Context and motivation.....	1
1.2. Objectives and methodology .....	2
1.3. Thesis outline .....	2
<b>Chapter 2 Literature Review .....</b>	<b>5</b>
2.1. General overview.....	5
2.2. Rammed earth from soil to wall.....	8
2.3. Mechanical characteristics of rammed earth.....	11
2.4. Structural behavior of rammed earth under lateral loads .....	13
2.5. Numerical studies .....	15
2.6. Strengthening techniques.....	20
<b>Chapter 3 Pushover Analysis of Unstrengthened Rammed Earth Walls .....</b>	<b>31</b>
3.1. Introduction.....	31
3.2. Geometry of the models .....	31
3.3. Rammed earth material properties .....	34
3.4. Finite element modelling .....	36
3.5. Mesh refinement.....	37
3.6. Model validation for self-weight.....	38
3.7. Modal analyses.....	39
3.8. Pushover analyses .....	43
3.8.1. In-plane models .....	44
3.8.2. Out-of-plane models .....	49
3.9. Influence of the damage on the dynamic properties .....	53
3.10. Concluding remarks .....	55
<b>Chapter 4 Pushover Analysis of Strengthened Rammed Earth Walls .....</b>	<b>57</b>
4.1. Introduction.....	57
4.2. Properties of the strengthening material .....	57
4.3. Finite element modelling of the strengthening .....	62
4.4. Strengthening selection.....	63
4.5. Modal analyses.....	64
4.6. Pushover analyses .....	64
4.6.1. In-plane model.....	65
4.6.2. Out-of-plane model.....	69
4.7. Influence of the damage on the dynamic properties .....	76
4.8. Concluding remarks.....	78
<b>Chapter 5 Time-history analyses of unstrengthened and strengthened rammed earth walls.....</b>	<b>81</b>
5.1. Introduction.....	81
5.2. Seismic input .....	81
5.3. Damping ratio .....	85
5.4. Time-integration method .....	86
5.5. Time-history analyses.....	88
5.5.1. In-plane models .....	88
5.5.2. Out-of-plane models .....	91
5.6. Concluding remarks.....	94
<b>Chapter 6 Conclusions and Further Research .....</b>	<b>95</b>
6.1. Main conclusions.....	95
6.2. Opportunities for further research .....	97
<b>APPENDIX A: Outcomes of Modal Analysis.....</b>	<b>103</b>
<b>APPENDIX B: Outcomes of Pushover Analyses.....</b>	<b>109</b>



This page is left blank on purpose.

## LIST OF FIGURES

Figure 1- Geographical distribution of earth constructions around the world (De Sensi, 2003) .....	5
Figure 2- Woodley Park center in Lancashire, UK constructed in 1999 (Maniatidis and Walker, 2003) ..	6
Figure 3 - Earthquake hazard in regions with earth constructions (De Sensi, 2003).....	6
Figure 4 - Development map of rammed earth construction (Jaquin <i>et al.</i> , 2007).....	7
Figure 5 - Arg-e-Bam (UNESCO world heritage as the largest adobe site): (a) before and (b) after earthquake in 2003.....	7
Figure 6 - Example of particle size distribution for rammed earth construction (Silva <i>et al.</i> , 2014a).....	8
Figure 7 - Particle size distribution proposed in the literature: (a) lower-bound (b) upper-bound (Maniatidis and Walker, 2003).....	9
Figure 8 - Rammed earth construction process (Minke, 2006).....	9
Figure 9 - Rammed earth construction phases (Minke, 2006).....	10
Figure 10-Different ramming techniques: (a) manual ramming (b) pneumatic ramming (Minke, 2006)	10
Figure 11 - Uniaxial compression test of rammed earth wallets (Miccoli <i>et al.</i> , 2014 and Miccoli <i>et al.</i> , 2015) .....	12
Figure 12 - Diagonal compression test of rammed earth wallets (Miccoli <i>et al.</i> , 2014 and Miccoli <i>et al.</i> , 2015) .....	12
Figure 13 - Mostly observed damages in rammed earth building subjected to earthquake (Wang <i>et al.</i> , 2016) .....	14
Figure 14 – Plan view and constructed rammed earth model to be tested on shaking table (Wang <i>et al.</i> , 2016).....	14
Figure 15 - Developed crack patterns at unreinforced rammed earth building tested on shaking table (Wang <i>et al.</i> , 2016).....	14
Figure 16 - Simplified models used to evaluate the out-of-plane wind capacity of rammed earth walls: (a) elastic analysis approach (b) ultimate strength method (Ciancio and Augarde, 2013) .....	15
Figure 17 - Comparison between macro- and micro-modeling approaches used to simulate diagonal compression tests (Miccoli <i>et al.</i> , 2015) .....	17
Figure 18 - DE modeling of a rammed earth wallet tested under diagonal compression (Bui <i>et al.</i> , 2015) .....	17
Figure 19 - Blind prediction of the out-of-plane capacity of a brick masonry model (Candeias <i>et al.</i> , 2016 and Mendes <i>et al.</i> , 2017).....	18
Figure 20 - Sensitivity of wall strengthened by TRM to tensile strength and fracture energy of matrix (Basili <i>et al.</i> , 2016).....	19
Figure 21 - Macro-modeling approach to model TRMs (Mininno, 2016) .....	20
Figure 22 - Typical damages in vernacular dwellings subjected to earthquakes (Correia <i>et al.</i> , 2015)	20
Figure 23 - Typical out-of-plane failures of vernacular dwellings (Correia <i>et al.</i> , 2015).....	21
Figure 24 - Grout injection used to repair of cracks (Figueiredo <i>et al.</i> , 2013).....	21
Figure 25 - General flow-chart to characterize properties of employed mortars in strengthening and restoration of historical construction (Schueremans <i>et al.</i> , 2011) .....	22
Figure 26 - Cyclic behavior of a model strengthened with wooden elements (Yamin <i>et al.</i> , 2004) .....	22
Figure 27 - Construction and strengthening of an adobe masonry wall in Aveiro University (Figueiredo <i>et al.</i> , 2013).....	23

Figure 28 - Efficiency of the strengthening with synthetic mesh applied to a damaged adobe wall: (a) changes in the natural frequency (b) comparison between cyclic responses (Figueiredo <i>et al.</i> , 2013)	23
Figure 29 - Examples of FRP-composites application on existing buildings (Valluzzi <i>et al.</i> , 2014)	24
Figure 30 - Fabric sheets of TRM made of steel, carbon, and PBO (Mininno, 2016)	25
Figure 31 - TRMs failure modes and corresponding force-slip curve (Ascione <i>et al.</i> , 2015 and Mordanova <i>et al.</i> , 2016)	25
Figure 32 - Stress-strain curves of SRG, CTRM, and BTRM (Felice <i>et al.</i> , 2014)	26
Figure 33 - Load-displacement curves of SRG, CTRM and BTRM from lap-shear tests (Felice <i>et al.</i> , 2014)	26
Figure 34 - Strengthening layout by FRCM and crack patterns in strengthened and un-strengthened adobe wall (Mordanova <i>et al.</i> , 2016)	27
Figure 35 - Influence of mortar-based composites on out-of-plane response of masonry walls (Mordanova <i>et al.</i> , 2016)	27
Figure 36 - Numerical model of a typical rammed earth building in Alentejo region, Portugal (Librici, 2016)	28
Figure 37 - Influence of ring beam and FRCM on response of rammed earth building (Librici, 2016)	29
Figure 38 - Plan view and dimension of surveyed rammed earth buildings (units in m) (adopted from Correia, 2007)	32
Figure 39 - LNEC's shaking table: (a) schematic plan view (Mendes, 2012); (b) dimensions of the foundation slab (units in m)	33
Figure 40 - Models of the walls (units in m): (a) In-plane wall with 80 cm wing length (b) In-plane wall with 50 cm wing length (c) Out-of-plane wall	34
Figure 41 - Adopted stress-strain relationships for rammed earth: (a) multilinear relationship in compression (b) exponential relationship in tension	35
Figure 42 - Elements used in the preparation of the unstrengthened models (DIANA FEA BV, 2017): (a) 20 nodes solid element (b) 8 nodes shell element	36
Figure 43 - Schematic view of the shell models: (a) in-plane model (b) out-of-plane model	36
Figure 44 - Different considered mesh sizes of out-of-plane solid model: (a) mesh size = 25 mm (b) mesh size = 50 mm (c) mesh size = 100 mm	37
Figure 45 - Reactions of the models under self-weight loading: (a) in-plane solid model (b) out-of-plane solid model	38
Figure 46 - Highest contributing modes of the in-plane solid model with 80 cm wing and comparison with the design spectrums: (a) spectrum type 1 (far-field earthquake) (b) spectrum type 2 (near-field earthquake)	40
Figure 47 - Highest contributing modes of the in-plane solid model with 50 cm wing and comparison with the design spectrums: (a) spectrum type 1 (far-field earthquake) (b) spectrum type 2 (near-field earthquake)	40
Figure 48 - Highest contributing modes of the out-of-plane solid model and comparison with the design spectrums: (a) spectrum type 1 (far-field earthquake) (b) spectrum type 2 (near-field earthquake)	41
Figure 49 - Highest contributing modes of the in-plane shell model with 80 cm wing and comparison with the design spectrums: (a) spectrum type 1 (far-field earthquake) (b) spectrum type 2 (near-field earthquake)	42
Figure 50 - Highest contributing modes of the in-plane shell model with 50 cm wing and comparison with the design spectrums: (a) spectrum type 1 (far-field earthquake) (b) spectrum type 2 (near-field earthquake)	42

Figure 51 - Highest contributing modes of the out-of-plane shell model and comparison with the design spectrums: (a) spectrum type 1 (far-field earthquake) (b) spectrum type 2 (near-field earthquake) ....	43
Figure 52 - Pushover curves of the unstrengthened in-plane models with 80 cm wings: (a) shell model (b) solid model.....	45
Figure 53 - Pushover curves of the unstrengthened in-plane models with 50 cm wings: (a) shell model (b) solid model.....	45
Figure 54 - Damage representation of the solid in-plane model with 50 cm wings at the damage initiation step: (a) principal compressive stress (b) principal tensile strain .....	46
Figure 55 - Total lateral displacements at the peak capacity of the in-plane models with 80 cm wings: (a) shell model (b) solid model .....	46
Figure 56 - Total lateral displacements at the peak capacity of the in-plane models with 50 cm wings: (a) shell model (b) solid model .....	46
Figure 57 - Principal compressive stresses at the peak capacity for the in-plane models with 80 cm wings: (a) shell model (b) solid model.....	47
Figure 58 - Principal compressive stresses at the peak capacity for the in-plane model with 50 cm wings: (a) shell model (b) solid model.....	47
Figure 59 - Principal tensile strains at the peak capacity of the in-plane models with 80 cm wings: (a) shell model (b) solid model.....	48
Figure 60 - Principal tensile strains at the peak capacity of the in-plane models with 50 cm wings: (a) shell model (b) solid model.....	48
Figure 61 - Pushover curves of the unstrengthened out-of-plane models pushed in the negative direction: (a) shell model (b) solid model .....	49
Figure 62 - Pushover curve of the unstrengthened out-of-plane models pushed in the positive direction: (a) shell model (b) solid model .....	50
Figure 63 - Total lateral displacements at the peak capacity of the out-of-plane models pushed in the negative direction: (a) shell model (b) solid model.....	50
Figure 64 - Total lateral displacements at the peak capacity of the out-of-plane models pushed in the positive direction: (a) shell model (b) solid model .....	51
Figure 65 - Principal compressive stresses at the peak capacity of the out-of-plane models pushed in the negative direction: (a) shell model (b) solid model.....	51
Figure 66 - Principal compressive stresses at the peak capacity of the out-of-plane models pushed in the positive direction: (a) shell model (b) solid model .....	52
Figure 67 - Principal tensile strains at the peak capacity of the out-of-plane models pushed in the negative direction: (a) shell model (b) solid model.....	52
Figure 68 - Principal tensile strains at the peak capacity of the out-of-plane models pushed in the positive direction: (a) shell model (b) solid model .....	53
Figure 69 - Reduction in frequencies of the unstrengthened models during the pushover analyses: (a) in-plane model with 50 cm wing (b) out-of-plane model pushed in the negative direction (c) out-of-plane model pushed in the positive direction .....	54
Figure 70 - Changes in the effective modal masses of the unstrengthened models during the pushover analyses: (a) in-plane model with 50 cm wing (b) out-of-plane model pushed in the negative direction (c) out-of-plane model pushed in the positive direction .....	55
Figure 71 - Load-strain curves of low-cost textiles obtained from direct tensile tests: (a) glass fiber mesh G2 (b) nylon mesh G8 (Barroso, 2017) .....	58
Figure 72 - Setup for the uniaxial tensile tests on composite mortar-mesh specimens (Ascione <i>et al.</i> , 2015) .....	59

Figure 73 - Uniaxial tensile stress-strain curves of composite LC-TRM band specimens (Barroso, 2017): (a) G2 mesh (b) G8 mesh .....	59
Figure 74 - Trilinear numerical curves based on the experimental tensile stress-strain curves of TRM composite specimens: (a) G2 mesh (b) G8 mesh .....	60
Figure 75 - Adopted compressive stress-strain curve of the TRM composite: (a) average experimental behavior (b) numerical compressive behavior with descending post peak branch .....	61
Figure 76 - Applicability of the conventional parabolic compressive behavior in the modeling of the mortar: (a) adopted parabolic compressive behavior in DIANA FEA software (b) comparison between the numerical parabolic behavior and the experimental behavior of the mortar .....	62
Figure 77 - Adopted stress-strain composite behavior for the LC-TRM: (a) mesh G2 (b) mesh G8.....	62
Figure 78 - Interface element employed in the preparation of the strengthened models (DIANA FEA BV, 2017) .....	63
Figure 79 - Comparison between the different LC-TRM strengthening solutions on the seismic response of the in-plane model: (a) control node at the middle section of the web (b) control node at top of the right wing .....	63
Figure 80 - Pushover curves of the strengthened in-plane model in comparison of those of the unstrengthened one .....	65
Figure 81 - Lateral displacements of the in-plane models: (a) unstrengthened model at its peak capacity (b) strengthened model at the peak capacity of the unstrengthened model (c) strengthened model at its peak capacity .....	66
Figure 82 - Principal compressive stresses of the in-plane models: (a) unstrengthened model at its peak capacity (b) strengthened model at the peak capacity of the unstrengthened model (c) strengthened model at its peak capacity .....	67
Figure 83 - Principal tensile strains of the in-plane models: (a) unstrengthened model at its peak capacity (b) strengthened model at the peak capacity of the unstrengthened model (c) strengthened model at its peak capacity .....	68
Figure 84 - Damage of the LC-TRM composite in the in-plane strengthened model at its peak capacity: (a) principal compressive stress (b) principal tensile strain .....	69
Figure 85 - Pushover curve of the strengthened out-of-plane model pushed in the negative direction in comparison of the unstrengthened one .....	69
Figure 86 - Lateral displacements of the out-of-plane models pushed in the negative direction: (a) unstrengthened model at its peak capacity (b) strengthened model at the peak capacity of the unstrengthened model (c) strengthened model at its peak capacity .....	70
Figure 87 - Principal compressive stresses of the out-of-plane models pushed in the negative direction: (a) unstrengthened model at its peak capacity (b) strengthened model at the peak capacity of the unstrengthened model (c) strengthened model at its peak capacity .....	71
Figure 88 - Principal tensile strains of the out-of-plane models pushed in the negative direction: (a) unstrengthened model at its peak capacity (b) strengthened model at the peak capacity of the unstrengthened model (c) strengthened model at its peak capacity .....	72
Figure 89 - Damage state of the TRM composite on the out-of-plane strengthened model pushed in the negative direction at its peak capacity: (a) principal compressive stress (b) principal tensile strain .....	72
Figure 90 - Pushover curve of the strengthened out-of-plane model pushed in the positive direction in comparison of the unstrengthened one .....	73
Figure 91 - Lateral displacements of the out-of-plane models pushed in the positive direction: (a) unstrengthened model at its peak capacity (b) strengthened model at the peak capacity of the unstrengthened model (c) strengthened model at its peak capacity .....	74

Figure 92 - Principal compressive stresses of the out-of-plane models pushed in the positive direction: (a) unstrengthened model at its peak capacity (b) strengthened model at the peak capacity of the unstrengthened model (c) strengthened model at its peak capacity..... 74

Figure 93 - Principal tensile strains of the out-of-plane models pushed in the positive direction: (a) unstrengthened model at its peak capacity (b) strengthened model at the peak capacity of the unstrengthened model (c) strengthened model at its peak capacity..... 75

Figure 94 - Damage state of the TRM on the out-of-plane strengthened model pushed in the positive direction at its peak capacity: (a) principal compressive stresses (b) principal tensile strains ..... 76

Figure 95 - Changes in frequencies of the strengthened models during the pushover analyses: (a) in-plane model (b) out-of-plane model pushed in the negative direction (c) out-of-plane model pushed in the positive direction..... 77

Figure 96 - Changes in the effective modal mass of the strengthened models during the pushover analyses: (a) in-plane model (b) out-of-plane model pushed in the negative direction (c) out-of-plane model pushed in the positive direction ..... 78

Figure 97 - Portuguese seismic hazard map for earthquakes with 475 years returning period (site in study marked with a black dot): (a) type 1 (far-field earthquakes) (b) type 2 (near-field earthquakes) (Norma Portuguesa, 2009)..... 82

Figure 98 - Definition of the parameters for generating ground motion records: (a) design spectrum for type 1 and 2 earthquakes (b) schematic backbone of the artificially generated records ..... 83

Figure 99 - Sample of generated artificial ground motion records: (a) type 1 (b) type 2 ..... 84

Figure 100 - Compatibility of the generated type 1 ground motion records with: (a) spectral design acceleration (b) spectral design displacement ..... 84

Figure 101 - Compatibility of the generated type 2 ground motion records with: (a) spectral design acceleration (b) spectral design displacement ..... 85

Figure 102 - Variation of damping ratio with the frequency of the modes (a) in-plane model (b) out-of-plane model..... 86

Figure 103 - Time-history of the displacements of the in-plane model: (a) unstrengthened (b) strengthened..... 89

Figure 104 - Time-history of the load factor of the in-plane model: (a) unstrengthened (b) strengthened ..... 90

Figure 105 - Hysteretic behavior of the in-plane models: (a) strengthened (b) unstrengthened ..... 90

Figure 106 - Maximum principal tensile strains experienced by the in-plane models subjected to the ground motion: (a) unstrengthened (b) strengthened ..... 91

Figure 107 - Time-history of the displacements of the out-of-plane model: (a) unstrengthened (b) strengthened..... 91

Figure 108 - Hysteretic behavior of the out-of-plane models: (a) unstrengthened (b) strengthened .... 92

Figure 109 - Maximum principal tensile strains experienced by the out-of-plane model subjected to the ground motion: (a) unstrengthened (b) strengthened ..... 93

Figure 110 - Hysteretic behavior of the out-of-plane models in comparison with the pushover curve: (a) unstrengthened (b) strengthened ..... 94

Figure B 1 - Principal tensile strains of the solid unstrengthened in-plane model with 80 cm wing at its peak capacity from different views..... 109

Figure B 2 - Different views of the principal tensile strains of the solid in-plane unstrengthened model with 50 cm wing at its peak capacity ..... 110

Figure B 3 - Different views of the principal tensile strains of the solid out-of-plane unstrengthened model pushed in the negative direction..... 110

Figure B 4 - Different views of the principal tensile strains of the solid out-of-plane unstrengthened model pushed in the positive direction ..... 110

Figure B 5 - Different views of the principal tensile strains of the solid in-plane strengthened model with 50 cm wing at its peak capacity ..... 111

Figure B 6 - Different views of the principal tensile strains of the solid out-of-plane strengthened model pushed in the negative direction ..... 111

Figure B 7 - Different views of the principal tensile strains of the solid out-of-plane strengthened model pushed in the positive direction ..... 111

## LIST OF TABLES

Table 1 - Rammed earth wall thicknesses proposed in the literature .....	11
Table 2 - Mechanical properties of rammed earth reported in different studies .....	12
Table 3 - Calibrated material properties for numerical analysis of rammed earth with micro-modeling approach (Miccoli <i>et al.</i> , 2015) .....	16
Table 4 - Height, length and opening characteristics of the rammed earth walls of the surveyed buildings (adopted from Correia, 2007).....	33
Table 5 - Characteristics of LNEC's shaking table (LNEC, 2010).....	33
Table 6 - Mechanical properties of rammed earth (adopted from Silva <i>et al.</i> 2014a).....	35
Table 7 - Results of the mesh refinement procedure of the models .....	37
Table 8 - Validation of constructed finite element models .....	38
Table 9 - Dynamic properties of the in-plane solid model with 80 cm wing length .....	39
Table 10 - Dynamic properties of the in-plane solid model with 50 cm wing length .....	40
Table 11 - Dynamic properties of the out-of-plane solid model from modal analysis .....	41
Table 12 - Dynamic properties of the in-plane shell model with 80 cm wing length .....	41
Table 13 - Dynamic properties of the in-plane shell model with 50 cm wing length .....	42
Table 14 - Dynamic properties of the out-of-plane shell model .....	43
Table 15 - Mechanical properties of the adopted strengthening textiles (Oliveira <i>et al.</i> , 2017 and Barroso, 2017).....	58
Table 16 - Mechanical properties of the mortar selected to integrate the numerical modeling (Oliveira <i>et al.</i> , 2017 and Barroso, 2017).....	60
Table 17 - Dynamic properties of the strengthened in-plane model .....	64
Table 18 - Dynamic properties of the strengthened out-of-plane model.....	64
Table 19 - Seismic parameters of Odemira municipality (Alentejo region) for an earthquake with 475 years returning period and respective artificial ground motion duration parameters .....	83
Table 20 - Selected modes and calculated parameters for Rayleigh damping .....	86
Table 21 - Selected time-step size in the nonlinear time-history analyses .....	88
Table A 1 - Dynamic properties (20 modes) of the solid unstrengthened in-plane model with 80 cm wing.....	103
Table A 2 - Dynamic properties (20 modes) of the solid unstrengthened in-plane model with 50 cm wing .....	104
Table A 3 - Dynamic properties (20 modes) of the solid unstrengthened out-of-plane model .....	105
Table A 4 - Dynamic properties (20 modes) of the shell unstrengthened in-plane model with 80 cm wing .....	106
Table A 5 - Dynamic properties (20 modes) of the shell unstrengthened in-plane model with 50 cm wing .....	107
Table A 6 - Dynamic properties (20 modes) of the shell unstrengthened out-of-plane model .....	108



This page is left blank on purpose.

# CHAPTER 1

## INTRODUCTION

### 1.1. Context and motivation

A significant part of the World's heritage and monuments are constituted by structural masonry, where raw earth is a dominant material. Furthermore, the availability of earth makes this material as the first option for building in rural, isolated and low income societies. On the other hand, and in the past few decades the sustainability and other green inherent characteristics of earthen constructions made them to achieve a considerable attention even in modern developed countries. Considering all, it is essential to have a precise understanding about their behavior. From a general point of view, these structural systems have a stable behavior under gravity loads, which made them to withstand during centuries, although, they are highly endangered with respect to earthquakes. Hence, investigating their response under earthquake excitations, understanding the most probable failure mechanisms and eventually proposing reliable and efficient strengthening solutions are important concerns of recent research works. The development of this research is important from several aspects, such as preserving the cultural heritage values of many monuments, securing numerous lives and limiting induced economic impacts.

One of the most common construction techniques using raw earth is called rammed earth, in which moist earth is placed between panels and rammed to obtain a compact material. This structural system is widespread all around the World, while limited studies are available in the literature regarding this construction method. Moreover, most of studies are concentrated on the material point of view. Therefore, the current study has the purpose of investigating the seismic performance of rammed earth buildings. In this regard, wall components with different configurations are considered to assess the in-plane and out-of-plane behavior of them. Subsequently, it was aimed to evaluate effectiveness of recently developed strengthening solution for enhancing the seismic performance of

these walls. Among all convenient approaches, the low-cost textile reinforced mortar (LC-TRM) was selected, due to its simple application, reasonable costs and compatibility with substrate, which is an especially important concern in historical constructions.

## **1.2. Objectives and methodology**

As stated previously, the main objectives of the current study are assessment of the seismic performance of rammed earth walls and of the effectiveness of the LC-TRM strengthening solution when applied in these walls. These objectives were achieved by means of an integrated methodology, described as follows:

- Review of the literature related with rammed earth constructions, with special attention on the experimentally attained mechanical characteristics, employed numerical methods, previously observed seismic deficiencies and applied strengthening techniques.
- Definition of proper geometrical dimensions of rammed earth walls behaving in the in-plane and out-of-plane directions. This step was done by considering previously conducted surveys on existing rammed earth buildings from southern Portugal. Furthermore, the studied walls were expected to be tested on shaking table. Limitations of the experimental facilities and stability issues of the walls were also one of the key parameters for the decision. Finally, the considered walls were defined to represent the expected failure mechanisms.
- Preparation of numerical models of the walls by means of the finite element method. In this regard, the capabilities of different modeling approaches, namely by using shell or solid elements, were also investigated.
- Assessment of the seismic performance of unstrengthened and strengthened rammed earth walls by means of pushover and nonlinear time-history analyses.

## **1.3. Thesis outline**

The present thesis is articulated in six chapters. The current chapter presents the main objectives of the thesis and the corresponding methodology to achieve them. Chapter 2 contains a brief review on the literature regarding rammed earth constructions. It includes a brief description of the history and origin of the technique, of experimental studies on mechanical properties, of the most common weaknesses, of proposed strengthening methods and of different conducted numerical studies. Chapter 3 describes the definition of the geometrical dimensions of the walls considered in the study, and subsequently the definition of the appropriate material properties to be employed in numerical models. Later on, the finite element method is employed to prepare the numerical models. Hence, different models with a variety of mesh sizes were tested to investigate the sensitivity of the outcomes

and to select a proper meshing size. In addition, the models were verified with analytical calculations to ensure accuracy of outcomes. This chapter ends with the detailing of pushover analyses on the unstrengthened models and with the investigation of frequency change during the analyses. From the outcomes, the most adequate geometrical dimensions and modeling approaches were selected for further investigation. In Chapter 4, the seismic performance of the strengthened walls was assessed by means of pushover analyses. In this regard, the experimentally captured mechanical behavior of different LC-TRM were collected and processed to be employed in the numerical models. Preliminary studies were conducted to select the most efficient TRM. Then, the effectiveness of the adopted strengthening solution was evaluated in comparison of the simple bearing walls. At the end, the frequency change as an indicator of damage and integrity of employed strengthening was investigated. Chapter 5 presents outcomes of conducted nonlinear time-history analysis obtained from both unstrengthened and strengthened walls. In this regard, artificial records were first generated with respect to seismic regulations of the Portugal and the dynamic properties required in the analyses, such as damping and time-integration parameters, were defined. Finally, Chapter 6 highlights the obtained conclusions and suggests possible future research activities.

This page is left blank on purpose.

## CHAPTER 2

# LITERATURE REVIEW

### 2.1. General overview

Earth as the most available material in many regions around the world was probably one of the first building materials used for manmade constructions. In this regard, many traditional building techniques have been developed, among which the most known are adobe masonry and rammed earth. Therefore, it is easy to find worldwide spread historical monuments made of raw earth. Furthermore, the low associated building costs led this material to be an appropriate choice for societies with economic issues, as well as for hardly accessible regions and isolated rural areas. The fact is that approximately 30-40% of the world population is estimated to live or work in earthen constructions (Houben and Guillaud, 1994). Geographical distribution of such constructions is shown in Figure 1.



Figure 1- Geographical distribution of earth constructions around the world (De Sensi, 2003)

During last century, traditional earthen constructions are substituted by constructions made of more modern materials, such as steel and reinforced concrete in developed countries. This situation led to the almost disappearing of the use of earth constructions; however the last decades pursue for more sustainable building solutions led to a renewed interest for this type of constructions. An example of a modern earth building is shown in Figure 2. The fact is that an expensive earthen built heritage exists and that the demand for building with earth is increasing though these constructions must fulfill modern demands. On the other hand, many of these buildings are located in regions with medium or high earthquake possibility of occurrence (see Figure 3). Hence, it became necessary to understand the behavior of these constructions not only for modern design objectives but also for strengthening/repair of existing buildings and monuments.



Figure 2- Woodley Park center in Lancashire, UK constructed in 1999 (Maniatidis and Walker, 2003)

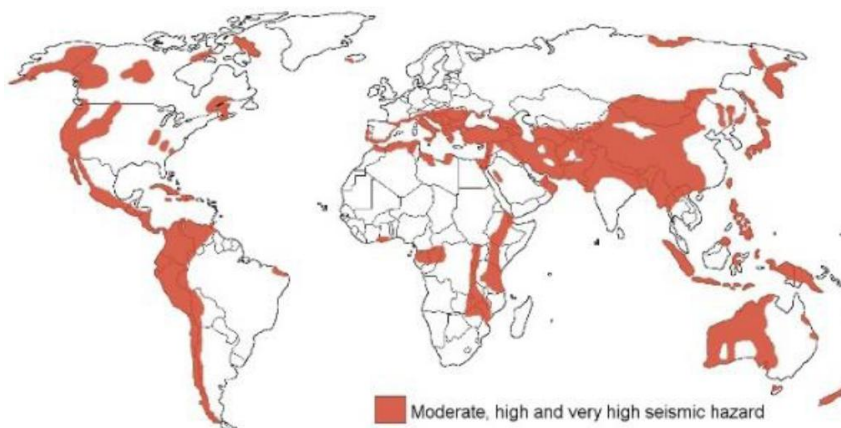


Figure 3 – Earthquake hazard in regions with earth constructions (De Sensi, 2003)

The current study is focused on study of rammed earth structures. In this technique, earth with adequate moisture content is placed between two parallel panels and is compacted (see Section 2.2 for further detail). This practice is well-known in all continents, as it can be understood from its specific name in different languages. For instance, it is known as *pisé* in French, *tapial* in Spanish, *taipa* in Portugal, *terra battuta* in Italian, *stampflehm* in German, *hangtu* in China, *chineh* in Iran and *pakhsa* in Uzbekistan. According to Jaquin *et al.* (2007) the rammed earth technique was independently

developed in China and in the Mediterranean region; which is later spread by the settlers of the New World. Its development map is depicted in Figure 4.



Figure 4- Development map of rammed earth construction (Jaquin *et al.*, 2007)

To assess, repair and strengthen adequately earth constructions, it is essential to understand their weaknesses. Several factors such as rainwater, soluble salts, and temperature oscillations can lead to occurrence of damage (Parreira, 2005). Although, these constructions have good behavior under gravity loads, but like other types of masonry buildings they are strongly endangered with respect to lateral loads. For example, many inhabitants, especially in rural regions and historical monuments of Turkey (Erzinkan 1992), Iran (Bam 2003), Peru (Pisco 2007) and Chile (Concepción 2010), have been severely affected by the occurrence of recent earthquakes. In this regard, one of the most catastrophic losses is the devastation of the historical citadel of Arg-e-Bam, classified by UNESCO as world (see Figure 5).



Figure 5- Arg-e-Bam (UNESCO world heritage as the largest adobe site): (a) before and (b) after earthquake in 2003

To further provide a comprehensive framework of the purposes of this thesis, the following sections of this chapter present and discuss different aspects of rammed earth buildings, such as the raw



material, construction process, mechanical properties and numerical modeling approaches. Later on, some proposed strengthening methods in the literature and their effects are also reviewed.

## 2.2. Rammed earth from soil to wall

The main ingredients of rammed earth are gravel, sand, silt, clay, water and in some cases additives. With respect to these additives, they are categorized into two general classes. One traditional version contains no artificial additives so-called as natural rammed earth; while the other includes materials such as cement and lime. The latter is known as stabilized rammed earth. Including cement increases strength, Young's modulus, resistance to corrosion and frost attack, but on the other hand it has downside effects on the sustainability of this type of construction. It is vital to be note that using organic additives is avoided either in natural or stabilized rammed earth walls, due to increasing tendency of the wall to high shrinkage, bio-deterioration, and insect attack.

The particles distribution is one of the key parameters affecting the characteristics of the rammed earth constructions, but it is generally accepted that it is necessary to include all size fractions in adequate percentages. For instance, excessive clay content (expressed by plasticity index) may cause shrinkage issues. On the other hand, well-distributed earth minimizes the voids ratio and increases contact between soil particles, thus promoting higher strength and erosion resistance of the material. Theoretically, the optimal distribution in the case of entirely spherical soil ingredients could be obtained using Fuller formula as expressed in equation (1):

$$p = 100 \left( \frac{d}{D} \right)^n \quad (1)$$

Where  $p$  is the percentage of particles passing a given size,  $d$  is the size of the particles,  $D$  is the largest particle size and  $n$  is grading coefficient. For entirely spherical particles,  $n$  equals 0.5, while in practice it varies in the range of 0.2-0.25 (Maniatidis and Walker, 2003).

An example of particle size distribution for rammed earth construction is shown in Figure 6.

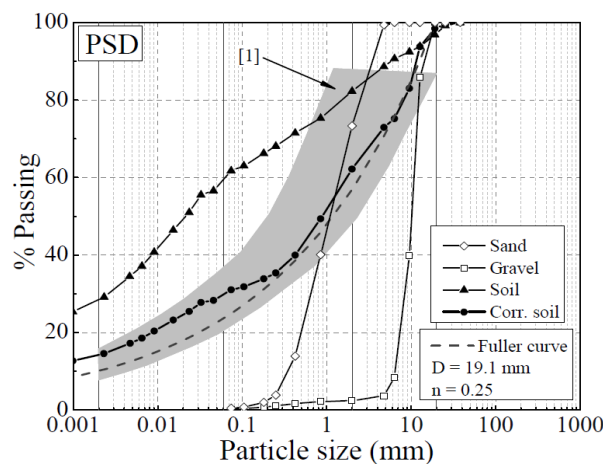


Figure 6 – Example of particle size distribution for rammed earth construction (Silva *et al.*, 2014a)

A wide variety of sub-soils can be used for rammed earth constructions; nevertheless a 30-70% balance between clay/silt and sand would be a reasonable distribution. Lower and upper bounds of particles mass distribution, proposed by different references are reported in Figure 7 (Maniatidis and Walker, 2003).

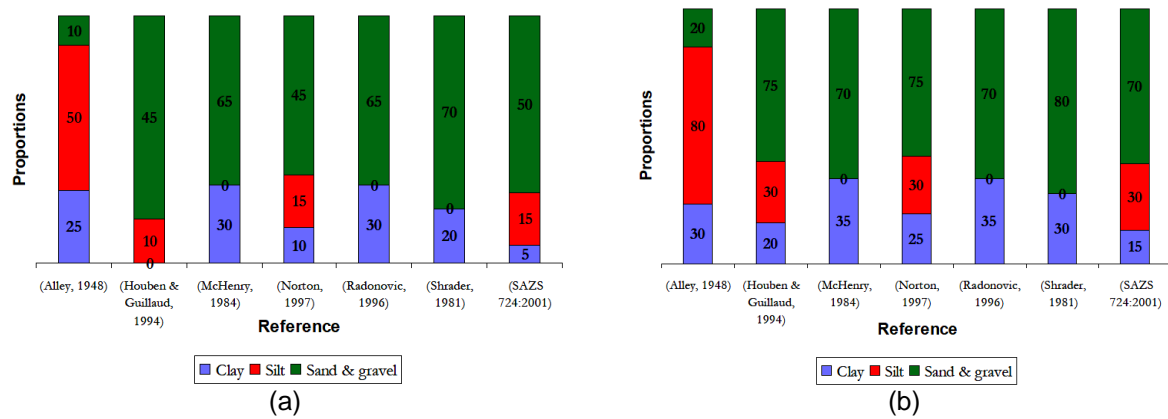


Figure 7- Particle size distribution proposed in the literature: (a) lower-bound (b) upper-bound (Maniatidis and Walker, 2003)

The other key parameter which affects mechanical characteristics is the moisture content. The optimal moisture content for filling the material into the formwork and subsequent compaction depends on the clay and silt content but it is usually around 10% of the mass (Miccoli *et al.*, 2014). It should be noted that the water content of the earth mixture to be built in rammed earth is less than for other earth construction types, e.g. Adobe.

After providing proper material, the construction process of a rammed earth wall is followed as shown Figure 8 and Figure 9. Different formworks have been employed in the practice depending on desired objectives, but generally, they first go surrounding the plan and then the higher level. The other key factor is the method of ramming. Traditionally, workers are hired while in more recent techniques pneumatic tools are also utilized (see Figure 10).



Figure 8- Rammed earth construction process (Minke, 2006)

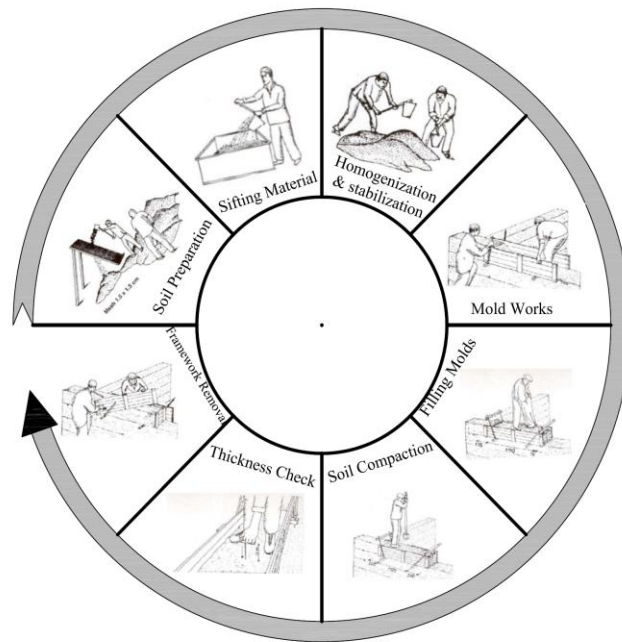


Figure 9 – Rammed earth construction phases (Minke, 2006)

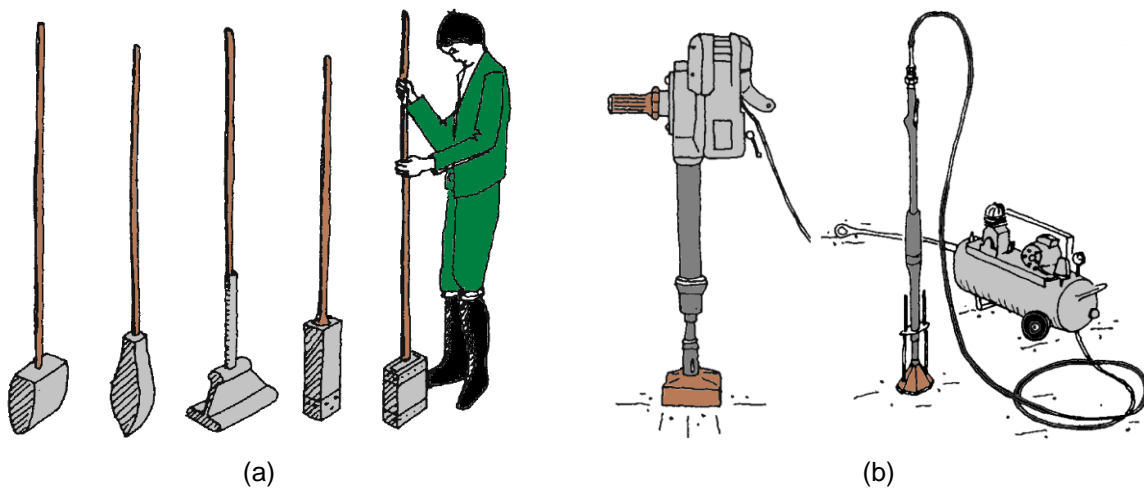


Figure 10 - Different ramming techniques: (a) manual ramming (b) pneumatic ramming (Minke, 2006)

Eventually, walls with different thicknesses are constructed to satisfy serviceability and stability conditions (mostly based on previous experiences). Different regulations specifying minimum values for wall thickness of rammed earth walls are presented in Table 1. Generally, these values are proposed to consider slenderness of walls to prevent excessive cracking under service load or compression buckling (Maniatidis and Walker, 2003). Table 1 also compares these minimum values with the typical thickness values of rammed earth walls of dwellings found in the Portuguese region of Alentejo. Here, the minimum normative values are clearly exceeded.

Table 1- Rammed earth wall thicknesses proposed in the literature

Region / Standard	Wall Thickness (mm)	
	Internal Wall	External Wall
New Zealand Code (NZS 4297, 1998)	250	
Zimbabwe Code (SAZS 724:2001, 2001)	300	
Australian Code (Standards Australia, 2002)	125	200
Alentejo, Portugal (Parreira, 2005)	500	

### 2.3. Mechanical characteristics of rammed earth

From a general point of view, rammed earth shows a fragile response under compression forces and low tensile strength. Considering this statement, identifying the mechanical characteristics of rammed earth materials is still a fundamental challenge within the investigation of this type of structures. Different parameters, such as particle size distribution, moisture content, compaction (rate and type), void ratio, cohesive strength of particles, fiber content and quantity of additions, affect the mechanical behavior of rammed earth. For instance, dynamic compaction (such as ramming or vibration) is more efficient than static compaction, since the first is able to promote a lower void ratio, and thus higher strength of the material. It is obvious that proposing any strengthening or repair without trustable mechanical properties may lead to a blind decision; however, limited knowledge exists in the literature. In this regard, a variety of experiments have been conducted to determine the mechanical properties of rammed earth, but as it is discussed later, they present expensive scattering. This situation may arise from different sources, such as characteristics of the soil, construction technique, and specimen scales. Yamin *et al.* (2004) conducted uniaxial and diagonal compression tests on wallets with full and 1:5 scales, concluding that parameters affected by self-weight (such as modulus of elasticity, compressive and tensile strength) will be scale-sensitive (Yamin *et al.*, 2004).

The apparent density and compressive strength of typical historical rammed earth (not stabilized) varies between 1700-2200 kg/m<sup>3</sup> and 1.5-4.0 MPa, respectively (Maniatidis and Walker, 2003); while the announced compressive strength in New Zealand and Australian standards is in the range of 0.4-0.6 MPa (NZS 4298, 1998 and Standards Australia, 2002).

It should be mentioned that the layered structure does not deem rammed earth to behave as a distinctively anisotropic material. For instance, studies have revealed that the compressive strength and Young's modulus determined parallel or perpendicular to layers do not vary more than 10%. It is necessary to note that this conclusion would not be correct for walls containing fibers (Miccoli et al., 2014). Field and laboratory tests were developed to obtain the strength of rammed earth, although field tests may lead to ambiguous interpretations and in some cases up to 200% error (Maniatidis and Walker, 2003). Uniaxial compression test on wallets (see Figure 11) were conducted to characterize compression behavior of rammed earth. These tests showed that the failure was characterized by a cone shaped cracking pattern and that the stress-strain behavior is expensively nonlinear.

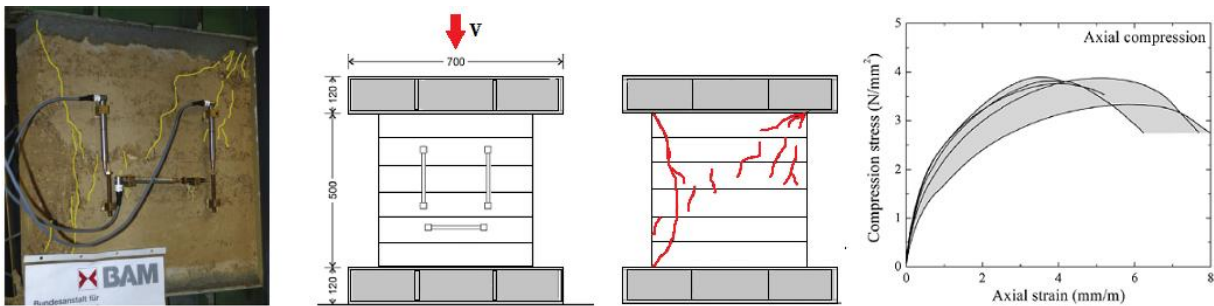


Figure 11- Uniaxial compression test of rammed earth wallets (Miccoli *et al.*, 2014 and Miccoli *et al.*, 2015)

Diagonal compression tests on wallets were also conducted in Miccoli *et al.* (2014) to characterize the shear behaviors of rammed earth. The obtained results are illustrated in Figure 12; nevertheless the failure was characterized by the formation of cracks crossing the diagonal section (between supports) of the wallets, while some delamination between layers was also detected. The shear strength and ultimate strains are in the range of 0.65-0.85 MPa and 1-2%, respectively.

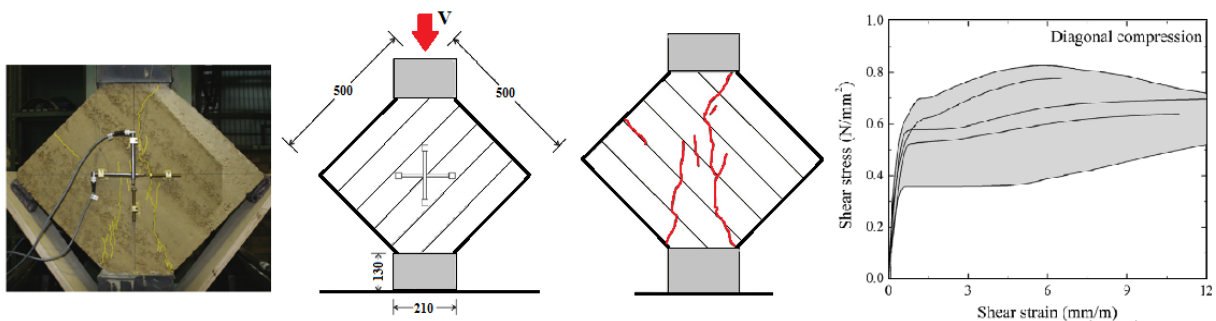


Figure 12- Diagonal compression test of rammed earth wallets (Miccoli *et al.*, 2014 and Miccoli *et al.*, 2015)

The fact is that the mechanical properties of rammed are reported in several studies, thus Table 2 is used to systemize this information.

Table 2- Mechanical properties of rammed earth reported in different studies

Ref.	$\rho$ (kg/m <sup>3</sup> )	$E$ (N/mm <sup>2</sup> )	$f_c$ (MPa)	Vertical Strain	$f_t$ (MPa)	$f_v$ (MPa)	$G$ (N/mm <sup>2</sup> )	Shear Strain	$\nu$ (-)	$\xi$ (%)
Lilley and Robinson (1995)	1870- 2170	-	1.8-2.0	-	-	-	-	-	-	-
Yamin <i>et al.</i> (2004)	1920	784.8	3.24	-	0.15	0.36	-	-	-	-
Parreira (2005)	2040.0	300.0	1.0	-	0.1	0.07	-	-	0.2	5.0
Bui and Morel (2009)	1800.0	90-105	1.0	-	-	-	-	-	-	-
Maniatidis <i>et al.</i> (2007)	1850.0	205	3.88	-	-	-	-	-	-	-
Miccoli <i>et al.</i> (2014)	-	4143 (STD = 961)	3.73 (STD = 0.23)	0.031 (STD = 0.007)	-	0.71 (STD = 0.11)	2326 (STD = 710)	0.011 (STD = 0.003)	0.27 (STD = 0.04)	-

Where  $\rho$  is bulk density,  $E$  is the Young's modulus,  $f_c$  is compressive strength,  $f_t$  is tensile strength,  $f_v$  is shear strength,  $G$  is shear modulus,  $\nu$  is Poisson's ratio and  $\xi$  is damping.

Among all reported properties, the Young's modulus and the shear modulus are those presenting the greatest scattering. Such differences are addressed not only due to inherent characteristics, workmanship or weathering but also due to the testing procedures. Moreover, the strength of earthen materials depends on their moisture content; as the moisture content increases, the strength decreases (Miccoli *et al.*, 2014).

## 2.4. Structural behavior of rammed earth under lateral loads

To understand the structural response of rammed earth under the action of an earthquake, it is required to investigate not only the behavior of the components (walls, connections, slabs and etc.) but also the full structure. This information includes both static (see Section 2.3) and dynamic properties, which will be present in this section.

Based on current seismic regulations, the seismic action can be imposed as an inertial force which is a function of fundamental period, damping ratio, and site characteristics. For low-rise buildings, seismic design codes provide empirical equations to calculate the dominant mode of vibration. Nevertheless, these formulas are developed for structures made with conventional structural systems and materials (concrete, steel, and masonry), meaning that their usage for rammed earth is not validated. For instance, Eurocode 8 proposes equation (2) for estimating the fundamental period ( $T_1$ ):

$$T_1 = C_t \cdot h_n^{3/4} \quad (2)$$

Where  $h_n$  is the height of the building and  $C_t$  is the coefficient which depends on the structural system and material, namely 0.0853, 0.0731 and 0.0488 for steel, reinforced concrete, and other building types.

In this regard, Bui *et al.* (2011) employed Frequency Domain Decomposition (*FDD*) technique to extract dynamic properties of rammed earth structures from in-situ experiments. By comparing the fundamental period obtained from the dynamic identification tests with that obtained using equation (2) (considering  $C_t = 0.0488$ ), it was possible to conclude that this equation is still acceptably valid for rammed earth buildings. It should be noted that in rammed earth buildings mostly do not present rigid floors; lateral loads should be applied and proportioned between components based on their lumped masses. Furthermore, Half-Power Band Width Method was employed to compute the damping ratio of the studied buildings, which resulted in values of 2.5-4.0% (Bui *et al.*, 2011).

Besides understanding the dynamic properties, it is required to find the most probable deficiencies or brittle failures to be prevented. Falling over due to out-of-plane actions, cracks at edges and at loading points where the load of the roof is transferred to the wall are among most observed damages in rammed earth building during previous earthquakes (see Figure 13). Wang *et al.* (2016) have tested a full scale one story typical rural rammed earth room with 2.6 x 2.4 x 2.1 m dimensions and a wall

thickness of 400 mm on shaking table. To realistically model the common construction, a wooden cantilever beam inserted to the top of wall, gable, wooden roof and door opening was also added. Plan and elevation view of the constructed model is shown in Figure 14.



Figure 13 - Mostly observed damages in rammed earth building subjected to earthquake (Wang *et al.*, 2016)

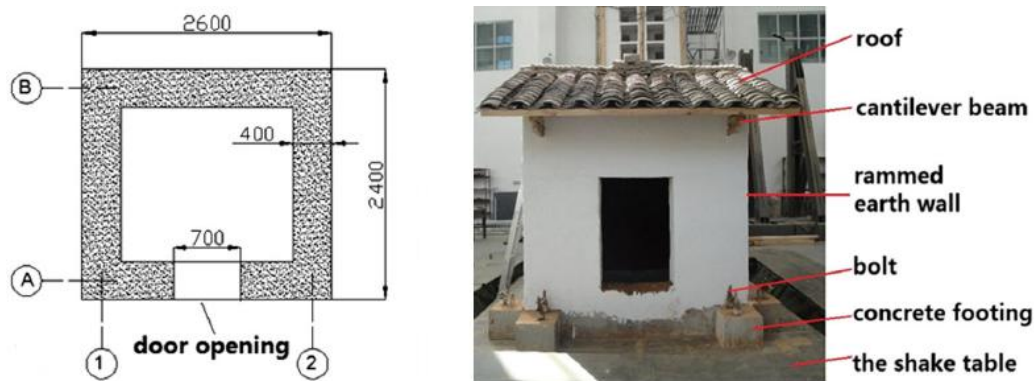


Figure 14 – Plan view and constructed rammed earth model to be tested on shaking table (Wang *et al.*, 2016)

Linearly scaled El Centro ground motion record is applied to the shaking table starting from the intensity with PGA equal to 0.1g. Major cracks have been developed on PGA equal to 0.4g and the model was approximately collapsed at 0.51g. Developed crack patterns at different intensities are shown in Figure 15.

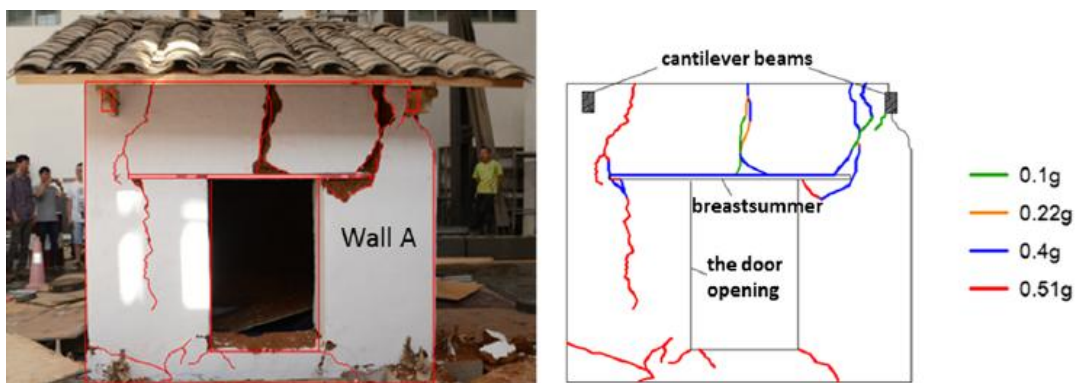


Figure 15 – Developed crack patterns at unreinforced rammed earth building tested on shaking table (Wang *et al.*, 2016)

## 2.5. Numerical studies

Different modeling approaches were employed to investigate the response of rammed earth walls, as summarized below:

- Simplified modeling (using limit analysis);
- Finite element (FE) modeling;
- Discrete element (DE) modeling;

As stated before (see Section 2.3 and 2.4) rammed earth presents an expensive nonlinear behavior, whereby predicting the response of structures, made from this material, by means of analytical or linear methods is a cumbersome task. However, few assumptions are considered in some studies to propose explicit equations based on simplified methods. For instance, Ciancio and Augarde (2013) propose to use two approaches based on limit analysis to evaluate the out-of-plane wind capacity of rammed earth walls. The first case considers the static approach (“Elastic Analysis”), where it is assumed that cracks are initiated from the point with tensile stress equal to tensile capacity (see Figure 16a). The second case considers the kinematic approach (“Ultimate Strength Analysis”), where the capacity and the failure mechanism of the wall can be defined using the principle of virtual work (see Figure 16b). By comparing the results of both approaches with experimental tests, it was concluded that the “Elastic Analysis” provides satisfactory accuracy. On the other hand, the “Ultimate Strength Analysis” only produces accurate results if the work necessary to open the mechanism crack is considered. As output, proposed equations (3) and (4) to compute the maximum uniform wind pressure, using the “Elastic Analysis” or the “Ultimate Strength Analysis”, respectively.

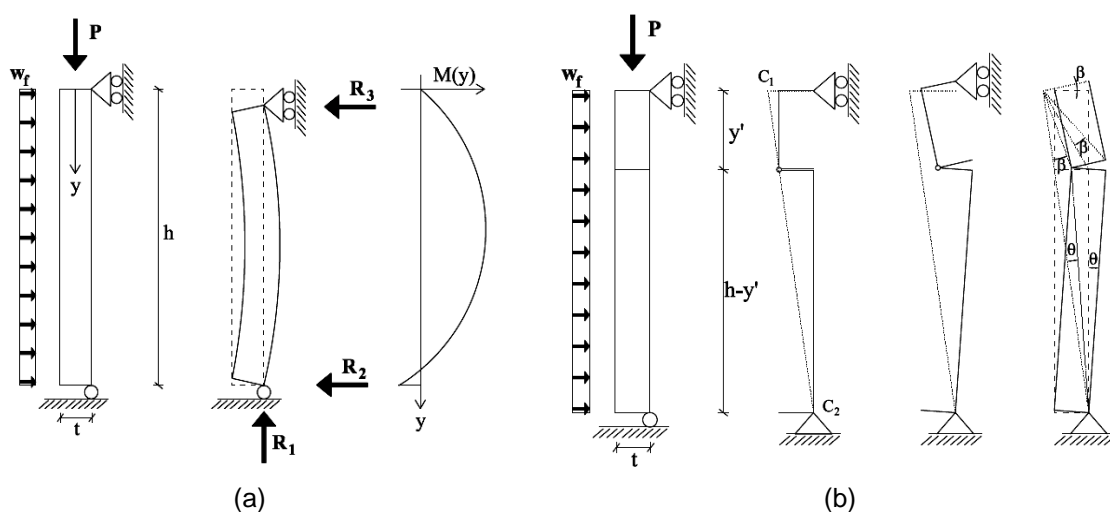


Figure 16- Simplified models used to evaluate the out-of-plane wind capacity of rammed earth walls: (a) elastic analysis approach (b) ultimate strength method (Ciancio and Augarde, 2013)



$$W'_f = \frac{5Pt + 2dt^2(f_t + 2h\gamma) + 2t\sqrt{(P + dtf_t)(4P + dt(f_t + 4h\gamma))}}{3dh^2} \quad (3)$$

$$W'_f = \frac{-t(2P + 2dht\gamma)^2 m}{dh^2((P + 2df_t t\alpha) - m)(2(P + df_t t\alpha) + 2dht\gamma - m)} \quad (4)$$

$$m = \sqrt{2(P + 2df_t t\alpha)(P + dt(f_t \alpha + h\gamma))}$$

Note that the geometrical parameters are defined in Figure 16, while  $f_t$  is tensile capacity and  $\alpha$  is fracture energy coefficient ( $G_f = \alpha \cdot f_t \cdot \delta_{max}$ ) and  $\delta_{max}$  is maximum crack opening. Ciancio and Augarde (2013) assumed  $\alpha$  and  $\delta_{max}$  as 0.15 and 0.15 mm, respectively.

With respect to FE modeling of rammed earth walls, two general approaches, i.e. macro or micro modeling were employed in previous studies. The macro-modeling approach does not consider layered and anisotropic nature of rammed earth, as the material is assumed to be continuous and isotropic. In micro-modeling, the rammed earth layers discretized and the interaction occurring between layers are taken into account. Nearly all available studies have employed the macro-modeling approach. The major reasons supporting this decision are the lack of reliable data to define the behavior of the interfaces and considerable reduction in computational efforts.

Miccoli *et al.* (2015) investigated the capacity of FE models, using both the macro- and the micro-modeling approaches to simulate the response of rammed earth wallets tested under uniaxial or diagonal compression. To model the rammed earth layers and interfaces, the total strain rotating crack model and the Mohr-Coulomb failure criterion were considered, respectively. It is valuable to mention that these models undergo a calibration process, where the behavior in compression was assumed to follow a multi-linear relationship (based on the average results of the compression tests) and the behavior in tension was assumed to follow an exponential relationship. An example of recommended material properties for numerical analysis of rammed earth obtained from calibration process is presented in Table 3.

Table 3 – Calibrated material properties for numerical analysis of rammed earth with micro-modeling approach (Miccoli *et al.*, 2015)

Material	$E_0$ (N/mm <sup>2</sup> )	$\nu$ (-)	$f_c$ (MPa)	$G_c$ (N/mm)	$f_t$ (MPa)	$G_f^I$ (N/mm)
Rammed earth	From test	From test	Multilinear from test	Multilinear from test	(0.08-0.12) $f_c$	(0.10-0.50) $f_t$
Material	$k_n$ (N/mm <sup>3</sup> )	$k_s$ (N/mm <sup>3</sup> )	$c$ (N/mm <sup>2</sup> )	$\tan(\phi)$ (-)	$\tan(\psi)$ (-)	$f_t^I$ (N/mm)
Interfaces	100 $E_0$	$kn / 2(1+\nu)$	(1.5-2.0) $f_t$	0.58 – 1.00	0.0	(0.67-1.00) $f_t$

Where  $E_0$  is Young's modulus,  $\nu$  is Poisson's ratio,  $f_c$  is the compressive strength,  $G_c$  is the compressive fracture energy,  $f_t$  is the tensile strength,  $G_f^I$  is the mode-I tensile fracture energy,  $k_n$  is the normal stiffness of the interface,  $k_s$  is the shear stiffness of the interface,  $c$  is the cohesion of interface,  $\phi$  is friction angle,  $\psi$  is the dilatancy angle and  $f_t^I$  is the tensile strength of the interface.

As it can be seen, both methods have a good agreement with experimental response. The micro-model shows possible delamination regions, although these areas are understandable from macro-model (Miccoli *et al.*, 2015). It may be concluded that micro-model does not result in significant advantages to simulate the diagonal compression tests.

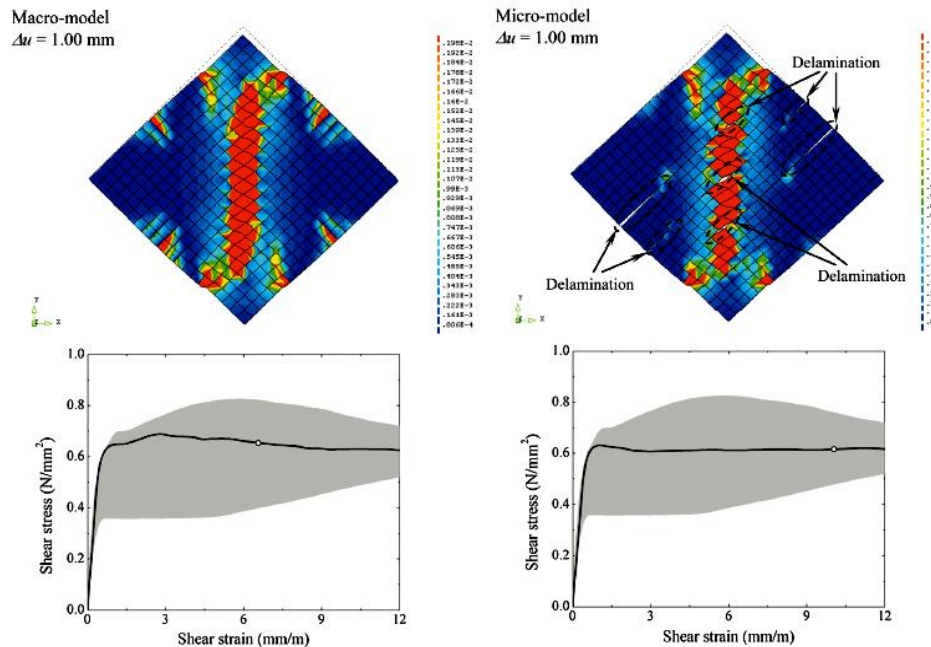


Figure 17- Comparison between macro- and micro-modeling approaches used to simulate diagonal compression tests (Miccoli *et al.*, 2015)

DE modeling is less popular than FEM in studies of rammed earth constructions, but some researchers have employed it to take into account the influence of layers in the response. Bui *et al.* (2012) modeled layers as homogenous and isotropic blocks which a Mohr-Coulomb behavior with tension cut-off assigned to the interface, using 3-Dimensional Distinct Element Codes (3DEC). Again, it was concluded that the results obtained by models with or without interfaces were similar, even when very low interface parameters were considered. Furthermore, the models were able to reproduce the first part of experimental behavior, but could not reproduce the nonlinear behavior of the experiment after the peak, as illustrated in Figure 18.

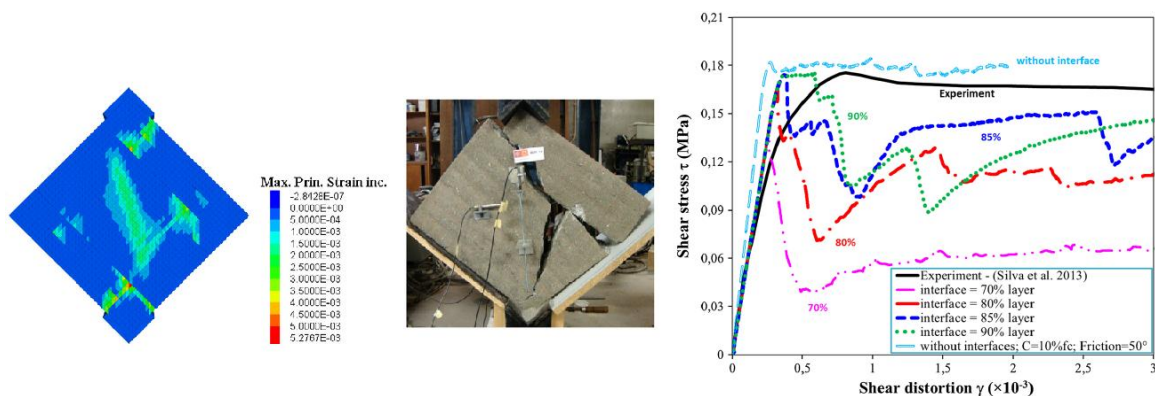


Figure 18- DE modeling of a rammed earth wallet tested under diagonal compression (Bui *et al.*, 2015)

It is worth to mention that previously discussed approaches obtained good agreed with experimental outcomes of rammed earth specimens tested under in-plane loading; nevertheless predicting the out-of-plane response of rammed earth is still a challenging topic that is insufficiently studied. In fact, more studied materials, such as masonry, share the same lack of knowledge. To highlight this issue, a blind test prediction was organized within the framework of an international conference (Mendes *et al.*, 2017). Two benchmark model buildings (brick and stone masonry) were tested on shaking table and the results were compared with numerical predictions. Both models had U-shape in plan a gable wall and an opening on the frontal façade, and an opening on one of side walls (see Figure 19). In this regard, different models using limit analysis, finite element modeling, and discrete element modeling were used by different experts. The blind predictions of the stone masonry resulted in an average value of the collapse PGA equal to 0.91g and a respective COV of 63%, while the experimental collapse PGA was of about 1.07g. In the case of the brick masonry model, the predicted average of PGA was equal to 0.64g and the respective COV was about 39%, while the experimental collapse PGA was about 1.27g.

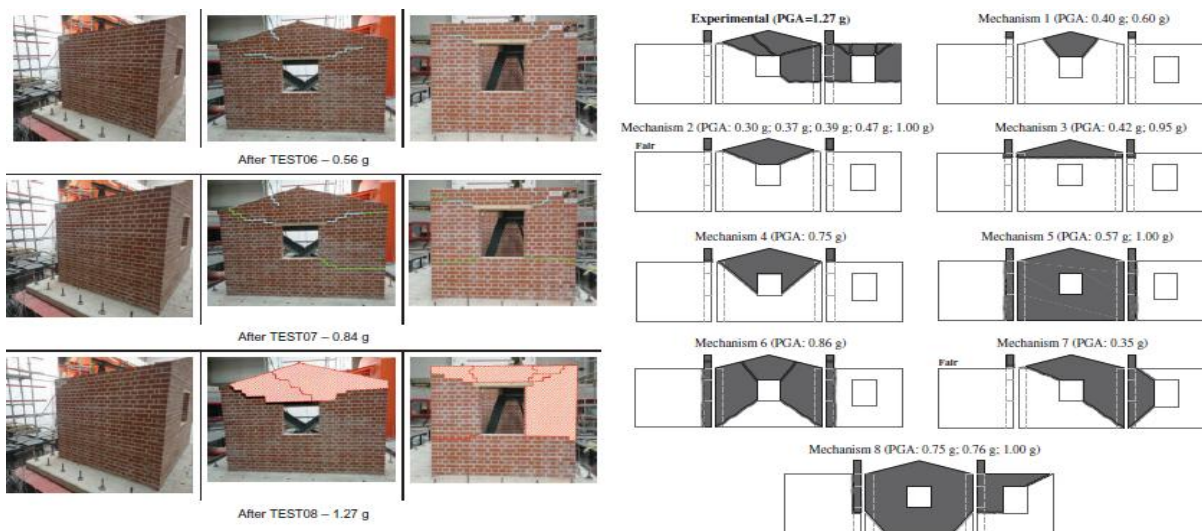


Figure 19- Blind prediction of the out-of-plane capacity of a brick masonry model (Candeias *et al.*, 2016 and Mendes *et al.*, 2017)

In addition to the need of modelling rammed earth structures using the aforementioned approaches, it is also essential to adopt an adequate strategy to model the behavior of rammed earth walls strengthened with Textile Reinforced Mortars (TRM). In this regard, different approaches are recommended in the literature, which can be generally classified into two groups:

- Micro-modeling, in which masonry, mortar, reinforcement and their interfaces are all modeled.
- Macro-modeling, in which the components' behavior is homogenized.

In this regard, Basili *et al.* (2016) adopted a macro-modeling approach and investigated the sensitivity of the outcomes, in terms of shear behavior to the variation of different parameters (on both

strengthened and un-strengthened walls). It was observed that the shear strength increases with increasing Young's modulus and the compressive/tensile strength (but not so much), while the variation in Poisson's ratio was not relevant. With respect to the fracture energies, it was observed that the influence of compressive fracture energy can be ignored, while the tensile fracture energy considerably affects shear strength with no major influence on degradation (see Figure 20). This influence of the tensile fracture energy was also observed by Garofano *et al.* (2016), where changing the tensile fracture energy from 0.009 N/mm to 0.012 N/mm caused the shear strength to increase by 30%. Approximately same outcomes were obtained for strengthened walls, where the mechanical characteristics of the matrix play an important role. It was observed that the mortar affects load carrying capacity at initial un-cracked stage; while the role of reinforcement becomes more significant in the cracked stage. Moreover, it was observed that employing double side reinforcement increases slightly the stiffness and approximately 20% the shear strength (Basili *et al.*, 2016).

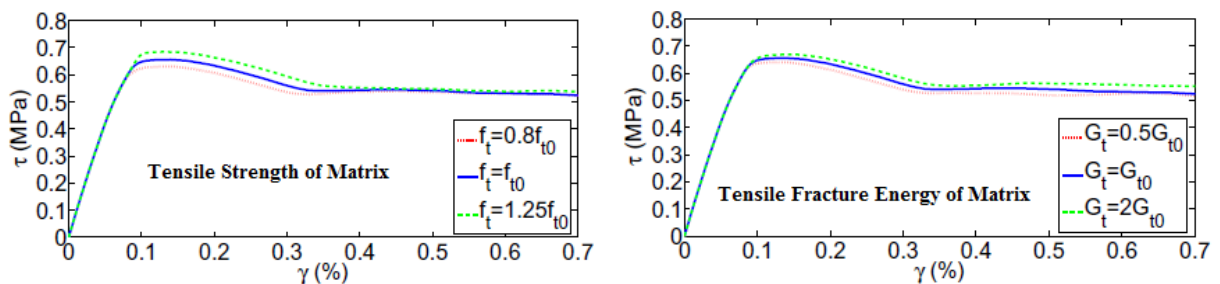


Figure 20- Sensitivity of wall strengthened by TRM to tensile strength and fracture energy of matrix (Basili *et al.*, 2016)

In another study, Mininno (2016) investigated the influence of TRMs on the in-plane and out-of-plane response of brick masonry walls, by adopting a macro-modeling approach in DIANA software. In the case of the in-plane models, quadrilateral 8-node shell elements were used to model the mortar matrix; while the reinforcement mesh was embedded as an equivalent grid in the matrix; hence no slip was possible between the mesh and the mortar. In other words, the strains of reinforcement and of the mortar are equal. A total strain crack model has been assigned to the matrix and its compression behavior was simulated by a parabolic relationship. Furthermore, the brittle linear tensile behavior was assigned to the reinforcement mesh. The interface between substrate and TRM was modeled by interface elements, but high stiffness values were assumed in the normal and tangential directions in order to avoid relative displacements. Perfect bond assumptions between the mortar and substrate are also used in other studies, but it worth to mention that this decision derives mainly from the lack of reliable data to characterize the bond behavior (Garofano *et al.*, 2016). In the case of the out-of-plane model, 8-nodes multi-layered shell elements were adopted. In these elements, the thickness of the shell can be subdivided in layers with different material properties (see Figure 21).

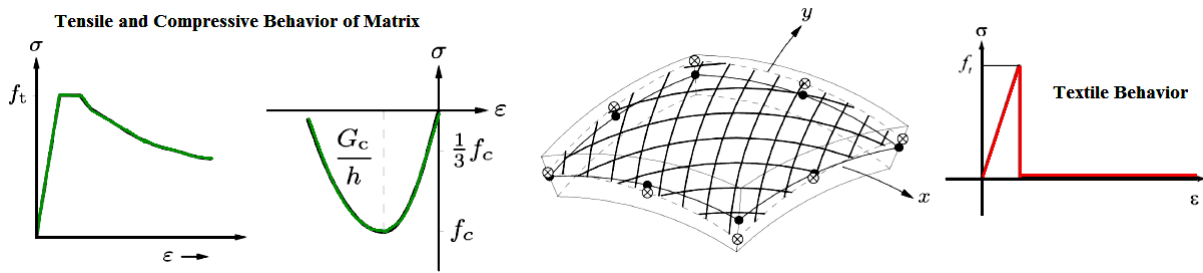
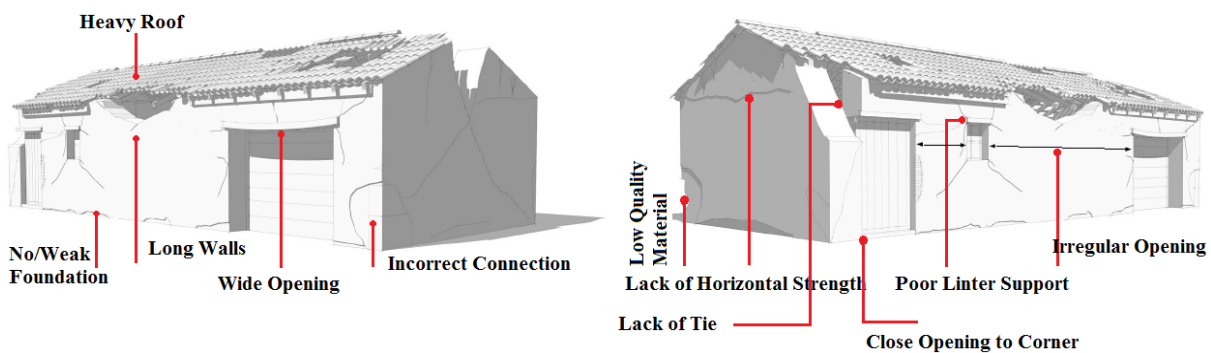


Figure 21- Macro-modeling approach to model TRMs (Mininno, 2016)

## 2.6. Strengthening techniques

Prior to proposing any strengthening technique, it is required to classify possible damages in rammed earth buildings and understanding their main causes. The most common issues on such buildings are the lack of continuity at corners and wall connections, the occurrence of concentrated roof loads, the absence of ring beams and the discontinuity between roofs and walls (see Section 2.4). Besides the aforementioned concerns, erosion, shrinkage cracks and other serviceability problems are also frequently observed. Since the main interest of current thesis is related with the behavior of rammed earth under earthquake excitations, hence the main possible failure mechanisms in such conditions are summarized below (see Figure 22) (Correia *et al.*, 2015):

Figure 22- Typical damages in vernacular dwellings subjected to earthquakes (Correia *et al.*, 2015)

- In-plane failure: it happens due to exceeding shear capacity of walls or initiation of inclined cracks (more or less  $45^\circ$ ) mostly from edges of openings;
- Out-of-plane failure: weak connection between orthogonal walls lead to the lateral loads perpendicular to plane of the wall to overcome its flexural capacity (see Figure 23).
- Roof/floor collapse: due to heavy loads on roof or its poor connection with walls;

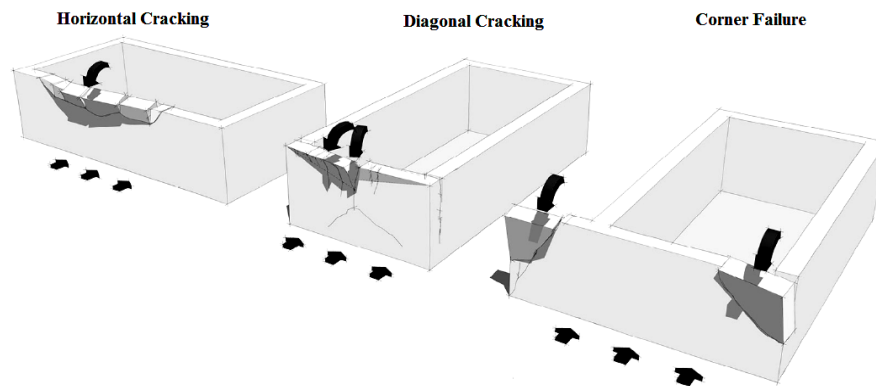


Figure 23- Typical out-of-plane failures of vernacular dwellings (Correia *et al.*, 2015)

Regarding the aforementioned deficiencies, several strengthening techniques are proposed in the literature. Nevertheless, before implementing any strengthening solution it is important to conduct prior repairs of existing damage. This first step may include local repair of damages (cracks, erosion or detachment) (Librici, 2016). One of the most common techniques at this level is grout injection of cracks, where special attention should be paid to compatibility requirements (see Figure 24).



Figure 24- Grout injection used to repair of cracks (Figueiredo *et al.*, 2013)

This compatibility should be addressed from physical, mechanical and chemical aspects between the injected grout and original materials. A general procedure to characterize employed mortars in restoration and strengthening of historical constructions is shown in Figure 25.

In following, paragraphs concept and efficiency of some of them is discussed.

With respect to the strengthening solutions for the earthen structures, Yamin *et al.* (2004) proposed using boundary wooden elements. These elements are installed on both faces of the walls and are connected by bolts going through the wall, whereby this solution is an easy economical option especially for societies with low incomes. This solution was evaluated by conducting in-plane cyclic, out-of-plane and shaking table tests on different specimens. The final conclusions were that the promoted confinement may increase ductility and cyclic stability under in-plane actions and also out-of-plane strength up to 100%, but cannot prevent the collapse of the building. Figure 26 presents a schematic sketch of the technique and compares the cyclic response of a strengthened model with that of un-strengthened one.

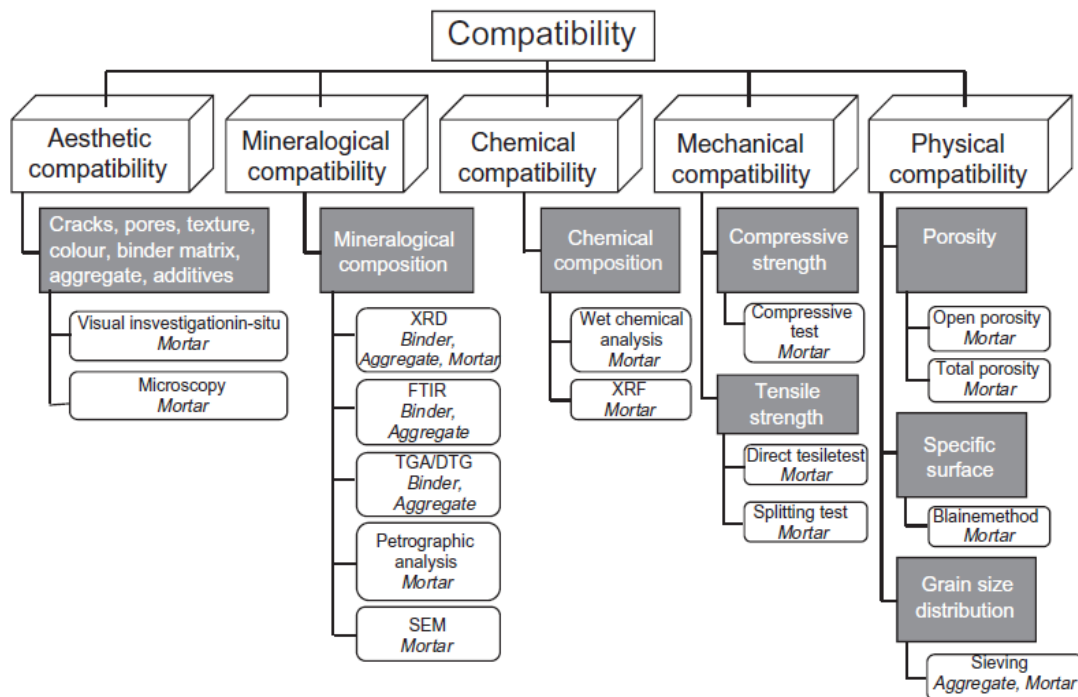


Figure 25 - General flow-chart to characterize properties of employed mortars in strengthening and restoration of historical construction (Schueremans *et al.*, 2011)

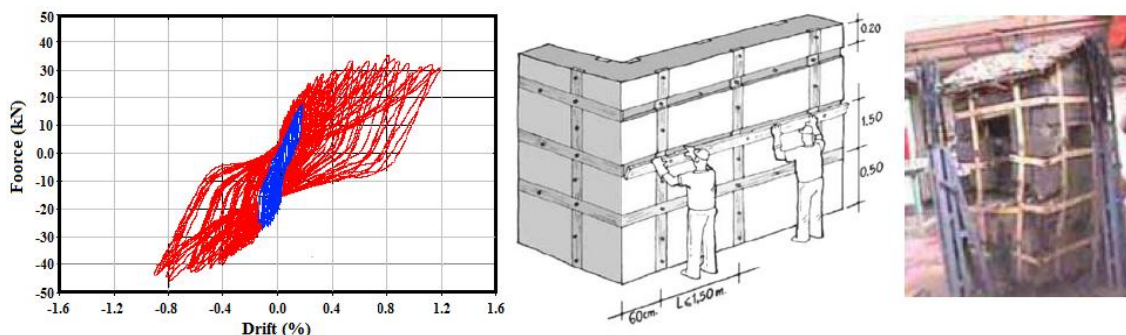


Figure 26- Cyclic behavior of a model strengthened with wooden elements (Yamin *et al.*, 2004)

Another possible strengthening solution consists in introducing reinforcing mesh on the inner and outer faces of walls. These mesh grids are attached by means of mechanical connectors and mortar. In this regard, different materials can be introduced, both for textiles and mortars. Figueiredo *et al.* (2013) strengthened a damaged full-scale adobe wall after an in-plane cyclic test. The strengthening consisted in applying a synthetic mesh fixed with PVC angle profiles and plastic fixing plugs. The Wall was built in I-shape in order to take into account the influence of adjacent walls. The construction and strengthening process is illustrated in Figure 27.

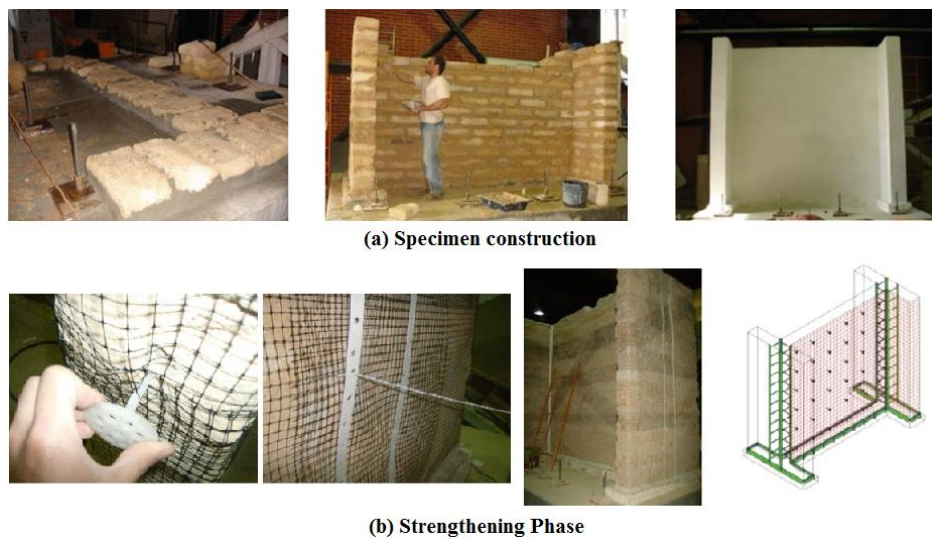


Figure 27- Construction and strengthening of an adobe masonry wall in Aveiro University (Figueiredo *et al.*, 2013)

The efficiency of strengthening technique was evaluated by recording the natural frequencies and hysteretic responses. The former, reveals capability of this method in reviving of initial stiffness; while the later shows enhancement in strength and in ductility. These advancements are shown in Figure 28. As it is evident, an increase of 23.43% and 220% could be detected in maximum resistance and drift, respectively.

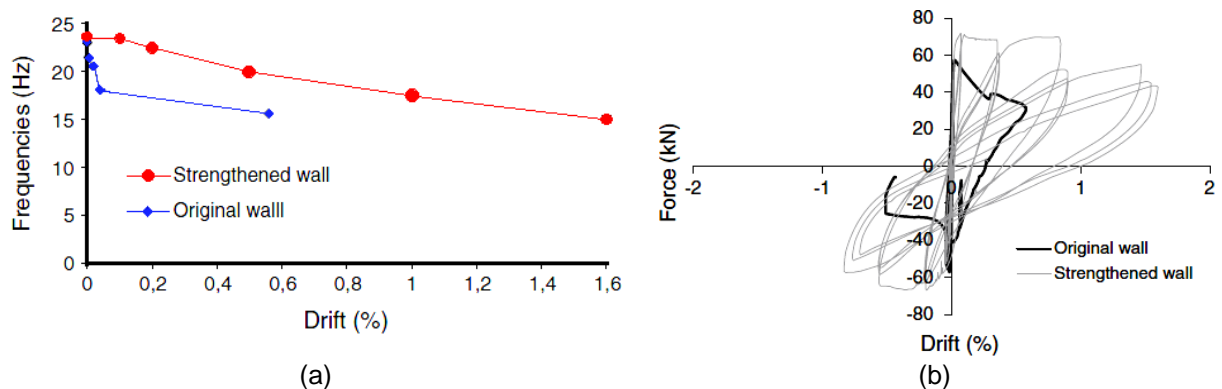


Figure 28- Efficiency of the strengthening with synthetic mesh applied to a damaged adobe wall: (a) changes in the natural frequency (b) comparison between cyclic responses (Figueiredo *et al.*, 2013)

In recent years, the application of composite-based materials to strengthen masonry structures has gained special interest. For instance, the application of FRP composites can effectively increase the shear/flexural capacity and ductility of walls, with a negligible increase in mass. In other words, this technique can strongly improve the weak tensile strength of masonry walls and change their failure mechanisms. This capacity is very important for earthquake strengthening purposes, since it does not



increase induced impacts by earthquake (due to minor mass increase). Generally, the application of composite-based materials on existing buildings may have the following objectives (Valluzzi *et al.*, 2014):

- Connection improvement and counteracting partial/overall collapses;
- Increasing in strength/stiffness of the walls;
- Columns/piers confinement;
- Enhancing load-bearing capacity of arches/vaults and decreasing the thrusts applied to the walls;
- Repairing existing cracks;

Some of these applications are illustrated in Figure 29. On the other hand, the strengthening with composite-based materials has its drawbacks, such as poor fire/high-temperature resistance, lack of vapor permeability, low reversibility, brittle failure and incompatibility with masonry substrate. Thus, the use of these materials in historical constructions is particularly dedicated, as the authenticity and minimum intervention principals must be respected (ICOMOS, 2003).



Figure 29- Examples of FRP-composites application on existing buildings (Valluzzi *et al.*, 2014)

Most of the aforementioned issues result from using organic epoxies in the application process. Therefore, alternative techniques have been developed in order to integrate more compatible matrixes such as cement- or lime-based mortars. Furthermore, strips are substituted by mesh grids to grant a good embedment. Steel Reinforced Grouts (SRG), Fiber Reinforced Cementitious Matrix (FRCM) and TRM (Textile Reinforced Mortar) are some of these new techniques. Besides the compatibility and FRP-composites advantageous, this technique has some other positive points like low installation costs, high durability and corrosion/fatigue resistance.

The roles of the cementitious matrix and of the reinforcement are the same as the epoxies and laminates in FRP-composites, i.e. matrix protects fibers and transfers stress from the substrate to the textile and the reinforcements are supposed to carry the tensile stresses.

The reinforcement fibers of TRM systems are mainly made of carbon, aramid, basalt, alkali-resistant glass PBO (Polyparaphenylene Benzobisoxazole) or hybrid systems. They are generally used as mesh sheets with grids not more than 2cm. Some of such fabric sheets are shown in Figure 30.



Figure 30- Fabric sheets of TRM made of steel, carbon, and PBO (Mininno, 2016)

Different failure modes have been observed on specimens strengthened with TRMs. It is schematically illustrated in Figure 31. The first three modes (A, B and C) are related to the shear failure in the substrate or matrix interface between substrate and textile, so-called as debonding. As it is shown, these modes have a clear flat shear-bond behavior after peak force followed by a brittle failure. Sliding of textile (mode D) has a more smooth force reduction due to friction loss. In modes E and F, the tensile failure of the textile happens before the flat region, leading to brittle failure. These modes will occur in cases where low strength textiles are employed.

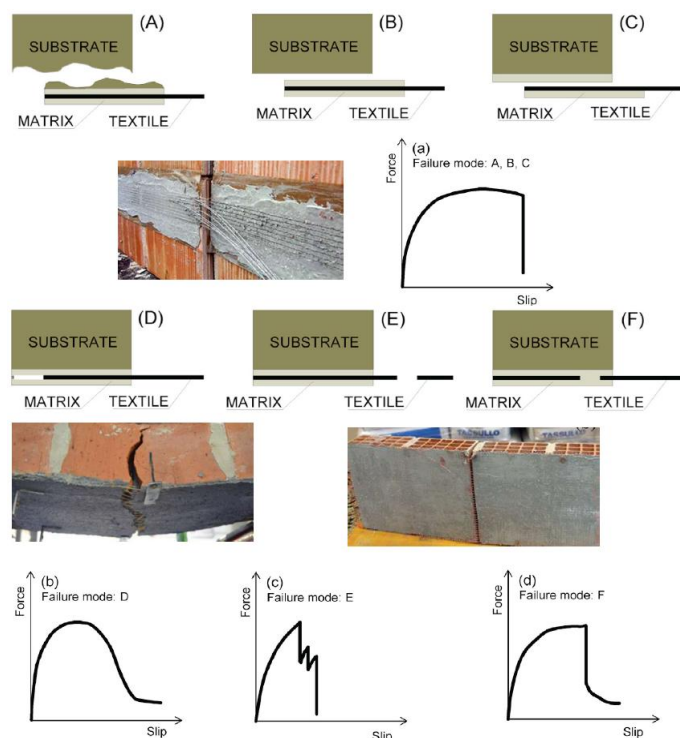


Figure 31- TRMs failure modes and corresponding force-slip curve (Ascione *et al.*, 2015 and Mordanova *et al.*, 2016)

The effective application of TRM strengthening solutions requires understanding their behavior, both at the level of the characteristics of the constituent materials and their interaction. In this regard, uniaxial tensile tests on steel reinforced grout (SRG), carbon textile reinforced mortar (CTRM), and basalt textile reinforced mortar (BTRM) were conducted at University Roma Tre (Rome, Italy), University of Minho (Guimarães, Portugal) and Tecnalia Research and Innovation (Bilbao, Spain). The obtained stress-strain curves are shown in Figure 32, from where it is clear that SRG has the highest tensile strength (approximately 3000 MPa), while the CTRM and BTRM have a similar capacity (approximately 1200 MPa) (Felice *et al.*, 2014). Regarding these stress-strain curves, three stages, i.e. un-cracked, crack development and cracked one can be distinguished. During the first stage, the behavior is linear, while by initiating cracks at stage II, the stiffness is reduced. By stabilizing crack opening, the load bearing capacity increases up to failure. In the first two stages, the mechanical characteristics of the mortar, textile, and their interface contribute for the behavior, while in the third stage the mortar matrix has mainly a redistribution function (Mininno, 2016).

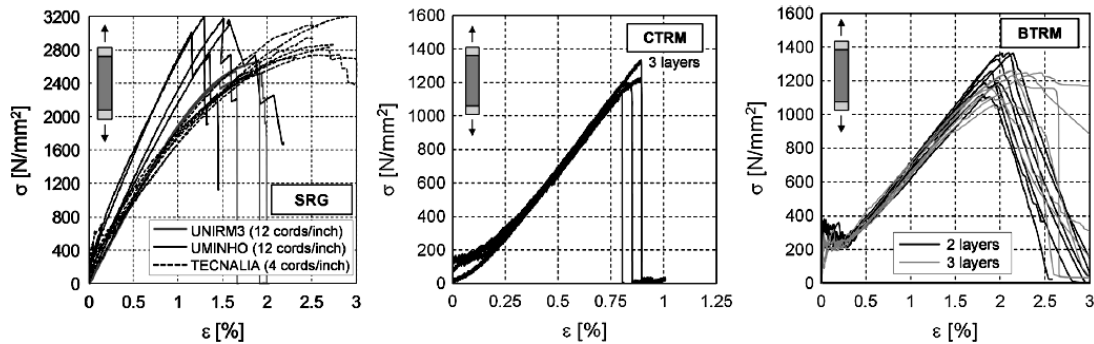


Figure 32- Stress-strain curves of SRG, CTRM, and BTRM (Felice *et al.*, 2014)

The other important parameters of the response are the interaction between the textile, matrix and substrate. In this regard, single and double lap shear tests were conducted on SRG, CTRM, and BTRM to investigate the bond strength. The force-displacement curves, obtained from the experiments (with different setups) are presented in Figure 33. The results revealed that the mortar, anchorage length, and substrate preparation have a significant influence on the debonding (Felice *et al.*, 2014).

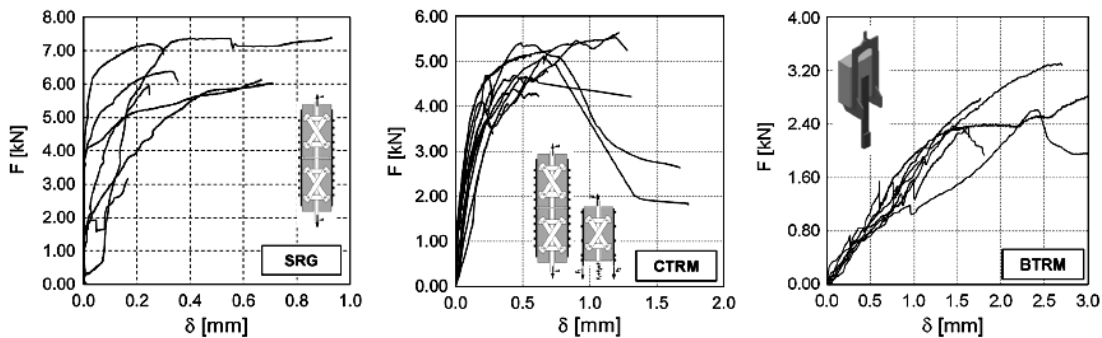


Figure 33- Load-displacement curves of SRG, CTRM and BTRM from lap-shear tests (Felice *et al.*, 2014)

Several numerical and experimental studies were conducted in the literature to assess the efficiency of externally bonded mesh grids with inorganic mortars. Experimental outcomes have shown that externally bonded FRP (FRP-EBR) can lead to shear strength increase in the range of 15-70%, while for TRMs it may increase up to 30%. Although TRMs are less effective than FRP-EBR with respect to capacity, their application lead to larger deformability, which can increase up to 15-30%. In other words, TRMs may improve ductility better than FRP-EBR. Garofano *et al.* (2016) investigated experimentally the influence of TRMs on the cyclic in-plane response of adobe masonry walls. The adopted strengthening consisted of polyester and polypropylene grids. The strengthening layout and crack patterns of the strengthened and un-strengthened walls are shown in Figure 34, where an evident change is clear, namely two major diagonal cracks in the unreinforced wall changed to a widespread pattern in strengthened one. Debonding occurred at the end of the test process; hence it was concluded that the interface may have no major influence on the response. Moreover, it was observed that different textiles have a different influence on strength increase (Mordanova *et al.*, 2016).

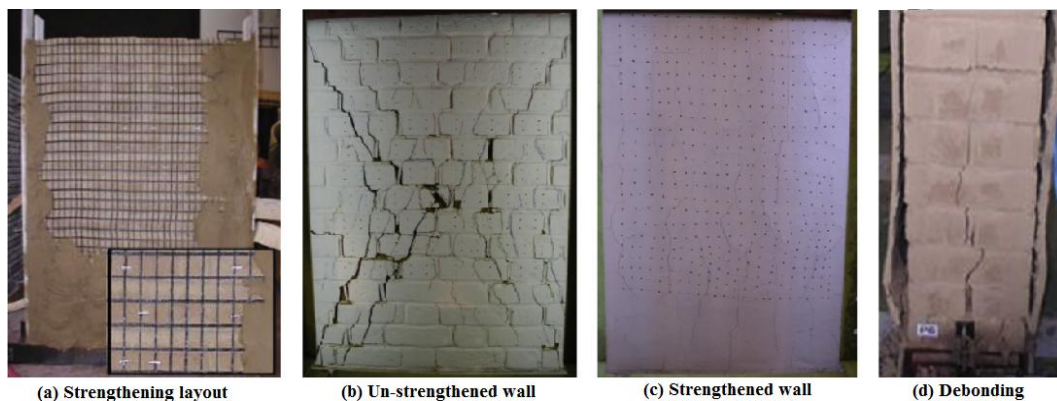


Figure 34- Strengthening layout by FRCM and crack patterns in strengthened and un-strengthened adobe wall (Mordanova *et al.*, 2016)

Furthermore, several experimental studies are conducted to evaluate the influence of mortar-based composites on the out-of-plane behavior of wall specimen. Outcomes are shown in Figure 35.

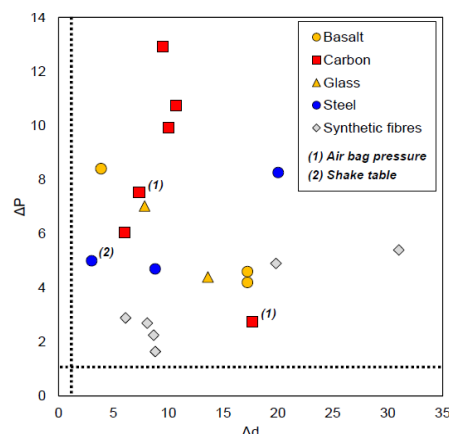


Figure 35- Influence of mortar-based composites on out-of-plane response of masonry walls (Mordanova *et al.*, 2016)

As it is clear, strength and displacement capacity have increased approximately 2-13 and 4-31 times, respectively. These outcomes are obtained from four-point bending tests. Generally, strength and displacement capacity increase in vice directions. In other words, composites leading to higher strength increase have less influence on displacement.

Several other strengthening techniques for rammed earth buildings such as introducing ring/bond beam (timber or concrete) at the top of walls are also proposed in the literature. Studies have shown that these elements not only increase the stiffness of walls and reduce vertical bending stresses on them but also make the displacement, between different walls more compatible. In other words, it significantly improves box behavior of the building. On contrary of that, its application may induce higher gravity loads which can decrease ductility of walls and produce strong disequilibrium in stiffness distribution. Moreover, it is shown that the connection between these beams and walls (their interface) could be critical and improper design of that cause higher shear demands to be governed which may result in local failure (Parreira, 2005 and Librici, 2016).

Mininno has compared the influence of this ring beams with previously discussed FRCMs on typical rural rammed earth buildings in Alentejo region, south Portugal. She used three-dimensional brick element and Total strain rotating crack model (CHX60 and TSRM of DIANA TNO) to model rammed earth wall. Exponential and parabolic softening functions were assigned for tension and compression, respectively, but performed nonlinear analysis has shown that parabolic compressive relationship cannot capture the real nonlinear behavior of rammed earth walls. Then, multi-linear relationship based on the average of the experimental axial tests was employed. Constructed model is shown in Figure 35.

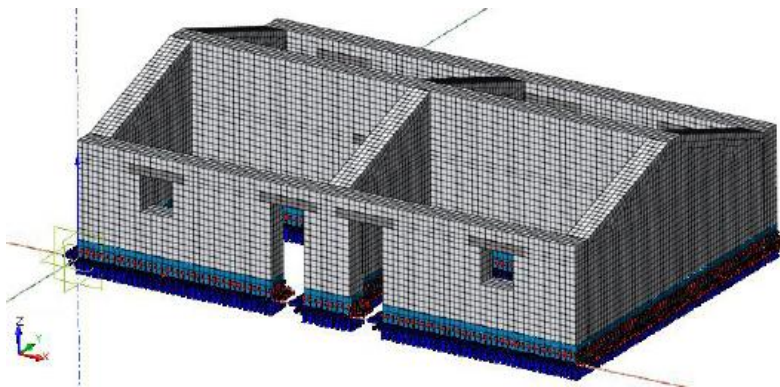


Figure 36- Numerical model of a typical rammed earth building in Alentejo region, Portugal (Librici, 2016)

It was concluded that ring beam increases the bearing capacity of walls but decreases their ductility. But numerical studies have shown that FRCM application increases capacity without any significant influence on ductility. Influence of their application (together and separated) with respect to ordinary buildings is shown in Figure 37. It was also concluded that PBO textiles are more effective than basalt

and basalt had better results than glass textiles. Finally, it was shown that the pushover analysis overestimates the values both in terms of force and displacement.

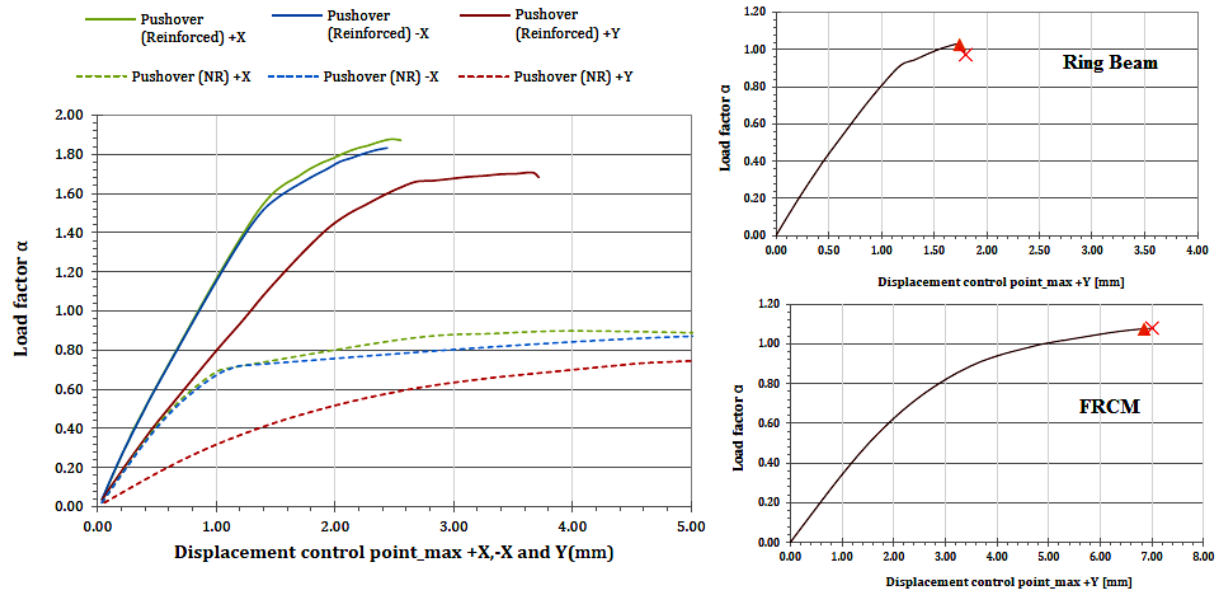


Figure 37- Influence of ring beam and FRCM on response of rammed earth building (Librici, 2016)

This page is left blank on purpose.

## CHAPTER 3

# PUSHOVER ANALYSIS OF UNSTRENGTHENED RAMMED EARTH WALLS

### 3.1. Introduction

This chapter includes the investigation of the behavior of unstrengthened rammed earth structural components (herein usually termed as walls) under lateral seismic loadings by means of nonlinear static analyses, also known as pushover analyses. Firstly, the geometric dimensions of the model, the material properties and the different modeling approaches (i.e. shell or solid elements) were defined and discussed. Subsequently, the corresponding finite element models were constructed, and a mesh sensitivity analysis was conducted to obtain an appropriate mesh size. The accuracy of these models was validated by outcomes of analytical results. Later on, the capacity, ductility and possible failure mechanism were studied for both in-plane and out-of-plane models. In addition, the frequency and modal mass changes of each model were investigated during given steps of the pushover analyses, to which correspond different damage states.

### 3.2. Geometry of the models

Two types of structural geometries were considered, namely one with a I-shape (in-plane behavior) and the other with a U-shape (out-of-plane behavior). These two components are expected to be tested both statically and dynamically on a shaking table in near future. Therefore, the definition of their dimensions should represent real rammed earth constructions from southern of Portugal, but also



must take into account the limitations coming from the size and maximum capacity of the shaking table.

Previously, eleven different rammed earth buildings were surveyed in Alentejo region (southern Portugal); whose plan views and respective dimensions are reported in Figure 38 (Correia, 2007). As it is seen, the wall thickness is, in all cases, of about 0.5m; hence the same dimension was adopted in the definition of the geometry of the models. Regarding the height and length of the walls, the surveyed values and their average/standard deviations are reported in Table 4. Other publications about full scale models tested under static and dynamic loading conditions were also analyzed, e.g. Candeias *et al.* (2016) and Figueiredo *et al.* (2012).

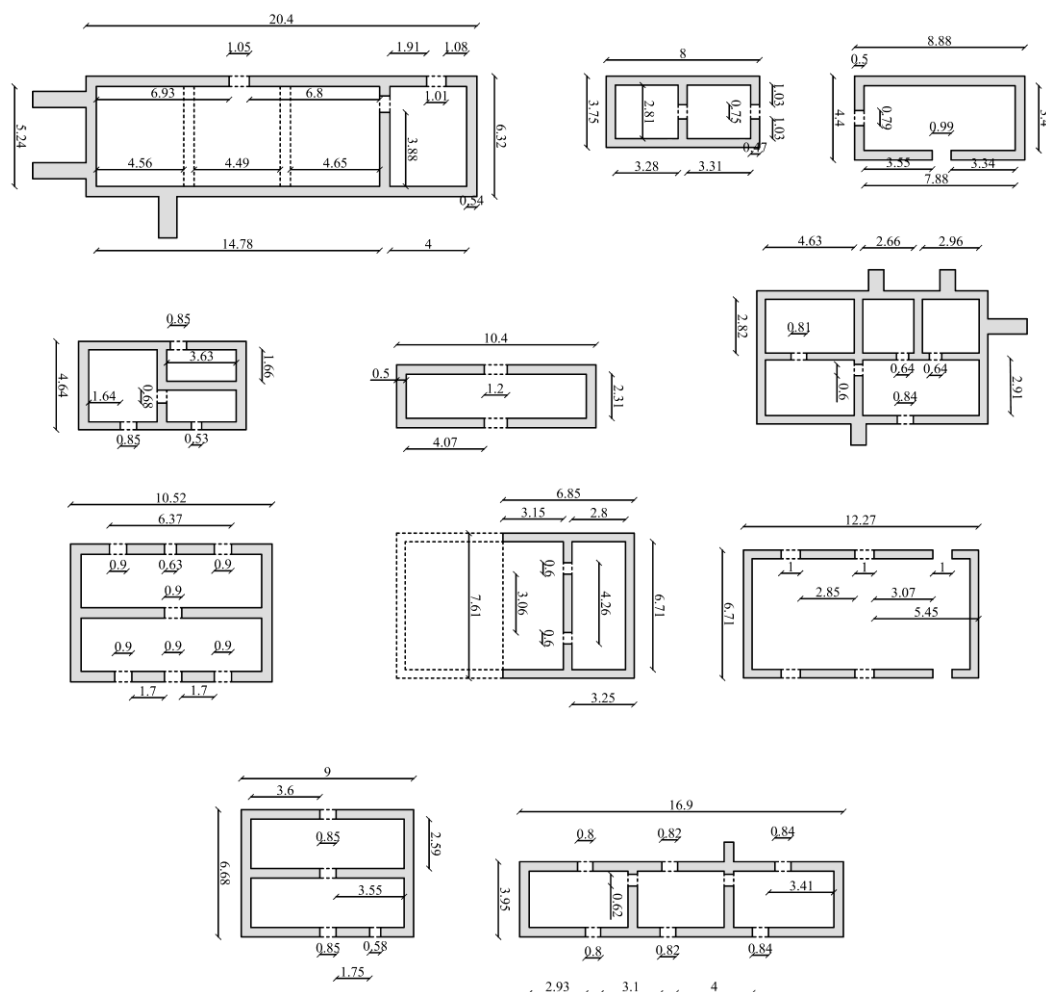


Figure 38 – Plan view and dimension of surveyed rammed earth buildings (units in m) (adopted from Correia, 2007)

The shaking table to be used is hosted in the Portuguese national civil engineering laboratory (LNEC) and its characteristics are briefly reported in Figure 39 and Table 5. It is worthwhile to mention that the maximum mass of rammed earth specimens that can be tested on LNEC's shaking table is of 21 tons.

Table 4 – Height, length and opening characteristics of the rammed earth walls of the surveyed buildings (adopted from Correia, 2007)

Building	Height (m)	Length (m)	Opening
1	2.46	5.24	No
2	2.23	2.81	No
3	2.48	3.4	No
4	2.01	3.79/1.66	No
5	2.5	2.31	No
6	1.88	2.82 / 2.91	No
7	2.59	2.79	No
8	1.55	6.71	No
9	2.1	5.81	No
10	2.2	2.59	No
11	2.1	2.95	No
Average	2.19	3.52	-
STD	0.31	1.49	-

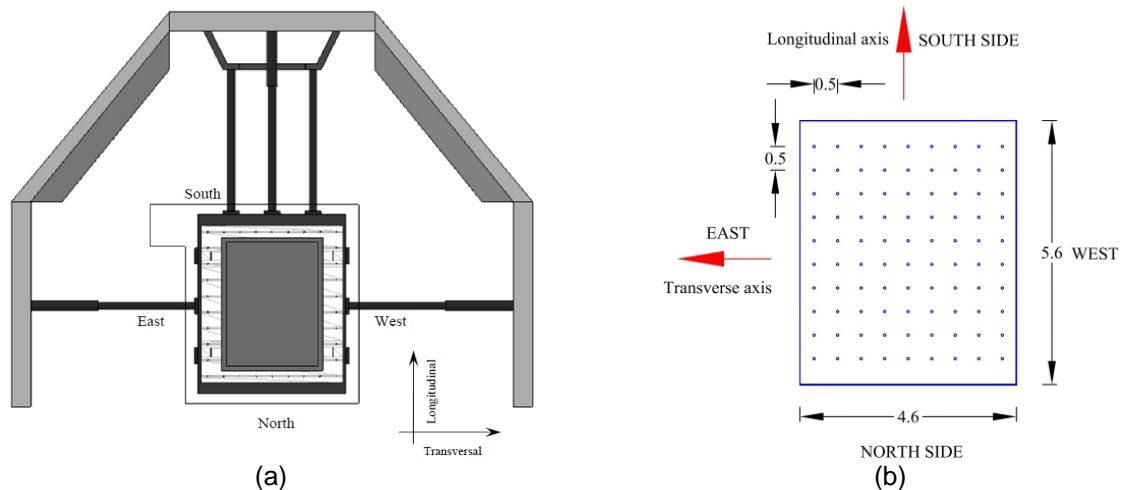


Figure 39 – LNEC's shaking table: (a) schematic plan view (Mendes, 2012); (b) dimensions of the foundation slab (units in m)

Table 5 – Characteristics of LNEC's shaking table (LNEC, 2010)

<b>Frequency range</b>		Hz	0.1-4.0
<b>Stroke (effective/maximum)</b>	Horizontal	mm <sub>pp</sub>	290/400
	Vertical	mm <sub>pp</sub>	290/400
<b>Maximum velocity (nominal/limit)</b>	Horizontal	Transversal	cm/s 70.1/121.5
		Longitudinal	cm/s 41.9/72.6
<b>Maximum acceleration for bare table</b>	Vertical	cm/s	42.4/73.5
	Horizontal	Transversal	m/s <sup>2</sup> 18.75
		Longitudinal	m/s <sup>2</sup> 9.38
	Vertical	m/s <sup>2</sup>	31.25
<b>Yaw/Pitch/Roll</b>	Rotation degree	°	N/A
	Velocity	rad/s	N/A
<b>Maximum overturning moment</b>		kN.m	N/A
<b>Maximum mock-up dead weight</b>		kN	392
<b>Maximum compensated dead weight</b>		kN	392

The definition of the geometry must also take into account the necessity of the models to behave and fail according to the expected behavior for these elements. In other words, an I-shaped wall should fail under diagonal cracks on the web and a U-shaped wall should fail due to out-of-plane collapse of the web. Given the expected influence of the geometry on the behavior of the models, two I-shape walls with different wing lengths and one U-shape were initially considered for analysis. Their dimensions and principal directions (x parallel to web and y perpendicular to that) are shown in Figure 40. The maximum weight of the considered walls would be as 18 tons (see Section 3.6). Furthermore, it should be noticed that the considered wings for the in-plane model are necessary for sake of stability; where the two lengths considered serve to assess if the considered values are sufficiently long to satisfy this condition.

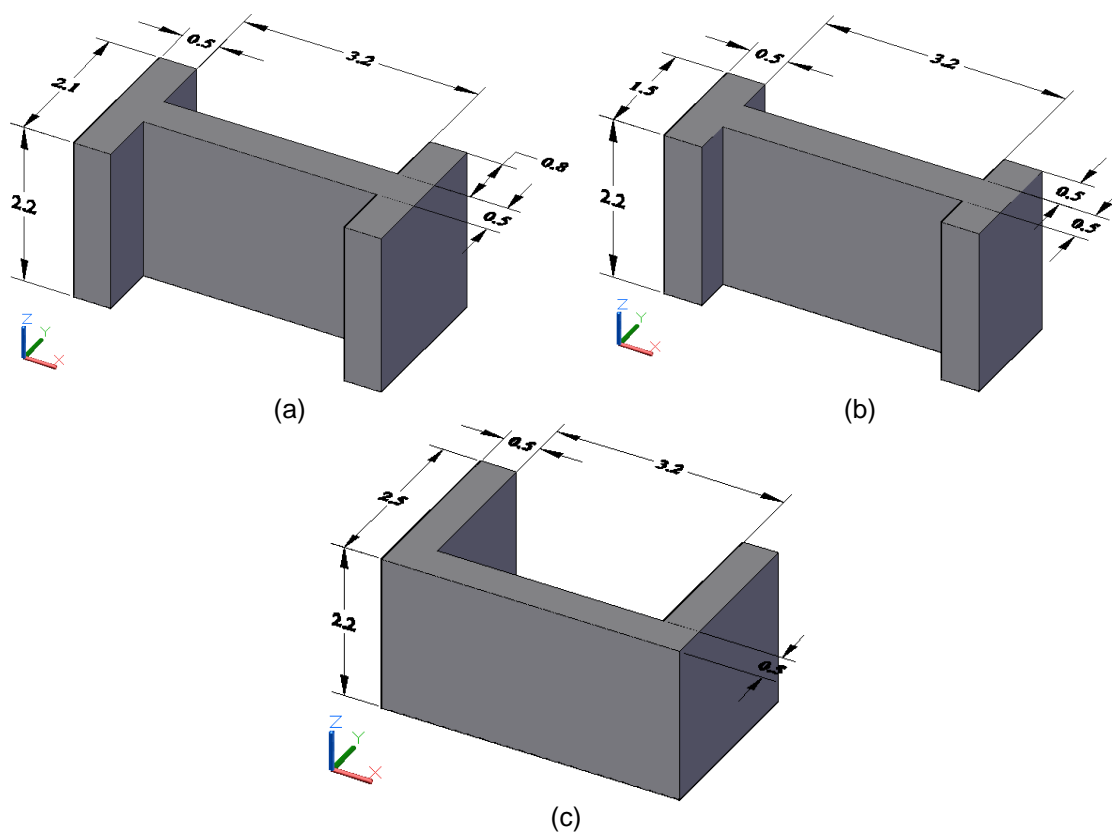


Figure 40 – Models of the walls (units in m): (a) In-plane wall with 80 cm wing length (b) In-plane wall with 50 cm wing length (c) Out-of-plane wall

### 3.3. Rammed earth material properties

Several studies have highlighted expensive nonlinear compressive behavior of the rammed earth. It was observed that the conventional concrete material model in compression (i.e. parabolic relationship) may not be proper for rammed earth material. In this regard, using a multi-linear relationship provides a better agreement with experimental outcomes, as suggested by Miccoli *et al.*

(2015) and Librici (2016). Thus, the current numerical investigation adopted a similar approach, by using a calibrated stress-strain relationship obtained from averaging results of the compression tests on cylindrical rammed earth specimens, detailed Figure 41a. Hence, it should be noted to take into account the post-peak softening and due to lack of experimental data, the curve is continued by the same slope of the experimental data. The other adopted mechanical properties were obtained from previously calibrated numerical models (both micro- and macro-models) used to simulate the experimental results from uniaxial and diagonal compression tests on rammed-earth wallets. Note that these specimens were built with a soil collected from Alentejo. In the calibration process of these wallet models, the total strain rotating crack model was assigned to the rammed earth material, whereby, the same approach was followed in the current study. Furthermore, the same exponential relationship was assumed for the tensile behavior of the rammed earth (see Figure 41b) (Silva *et al.* 2014a). In order to make the numerical outcomes independent from the size of the element, the crack bandwidth ( $h$ ) was assumed to be a function of the element area ( $A$ ), as expressed by equation (5):

$$h = \sqrt{A} \quad (5)$$

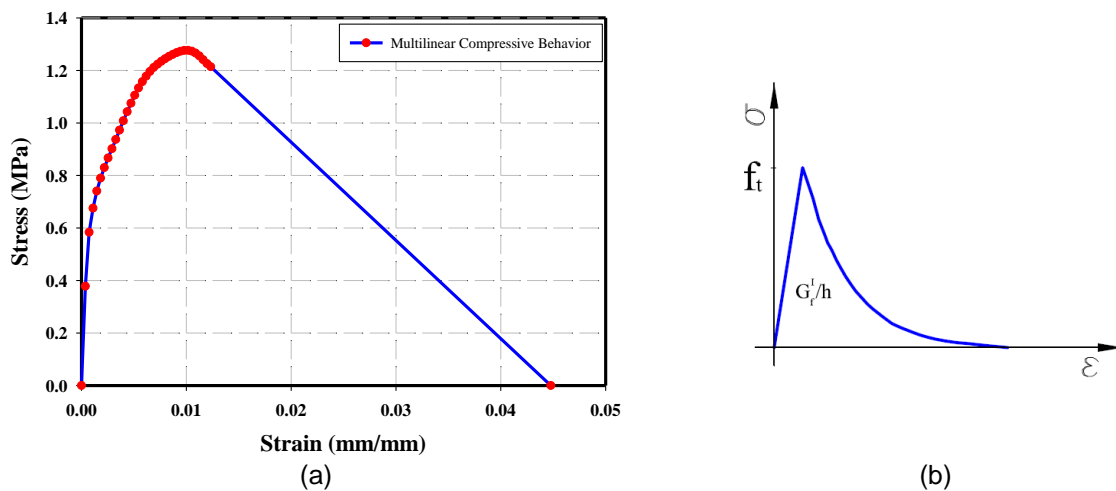


Figure 41- Adopted stress-strain relationships for rammed earth: (a) multilinear relationship in compression (b) exponential relationship in tension

The assigned properties of the rammed earth are given in Table 6.

Table 6 – Mechanical properties of rammed earth (adopted from Silva *et al.* 2014a)

Material	$E$ (N/mm <sup>2</sup> )	$\nu$ (-)	$f_t$ (MPa)	$G_f^l$ (N/mm)	$f_c$ (MPa)	$\rho$ (kg/m <sup>3</sup> )
Rammed earth	1034	0.27	0.05	0.074	1.28	2000

Where  $E$  is the Young's modulus,  $\nu$  is the Poisson's ratio,  $f_t$  is the tensile strength,  $G_f^l$  is the mode-I tensile fracture energy,  $f_c$  is the compressive strength, and  $\rho$  is the density.

### 3.4. Finite element modelling

The modeling of the structural component was evaluated initially by two modeling approaches, namely by considering solid and shell elements. In the case of solid models, 20 nodes iso-parametric brick elements CHX60 were used, as implemented in DIANA software (DIANA FEA BV, 2017) and illustrated in Figure 42a. In the case of the shell models, 8 node quadrilateral curved shell elements CQ40S (DIANA FEA BV, 2017) were adopted, see Figure 42b. The default integration scheme 3x3x3 was used for the solid elements, while the 2x2 was used for the shell ones, where the integration along the thickness considered 7 integration points.

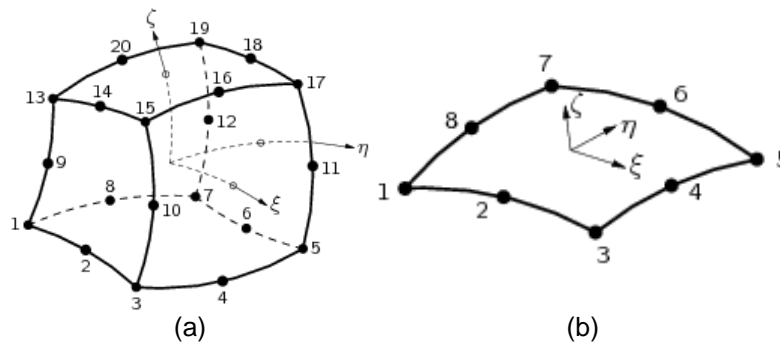


Figure 42 – Elements used in the preparation of the unstrengthened models (DIANA FEA BV, 2017):  
(a) 20 nodes solid element (b) 8 nodes shell element

Moreover, it is worth mentioning that the shell models were prepared considering the mid-section planes of each wall. A schematic view of this approach is depicted in Figure 43, where it is evident that this approach may introduce some errors.

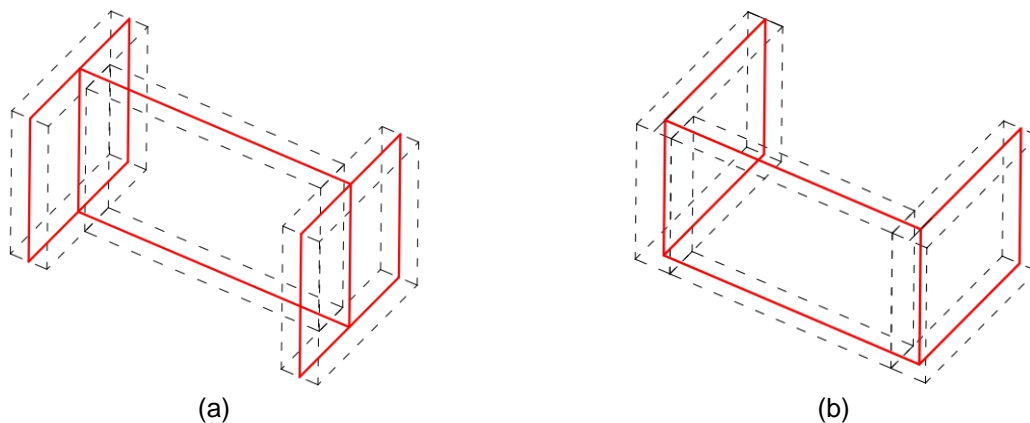


Figure 43 – Schematic view of the shell models: (a) in-plane model (b) out-of-plane model

For instance, the simulation of the connection between walls and the length of the wing cantilevers are properly modeled, where in this last case the web of walls in the model present higher length than in the reality. These are expected to have influence on the response obtained from the models. Furthermore, the overlapping thicknesses of the walls lead to a wrong consideration of the real self-weight value and mass distribution, and thus of the inertial forces. These aspects are further

discussed in the following, nevertheless it should be noted that adopting shell based models allow to reduce considerably the computational effort with respect to solid based ones.

### 3.5. Mesh refinement

A proper selection of the meshing size is necessary to obtain accurate results and relatively adequate computational times. In this regard, three meshing sizes were considered for the models, namely 25 mm (over-meshed), 50 mm and 100 mm. For instance, the out-of-plane solid model is presented in Figure 44 for the considered meshing sizes. All models were tested by considering the material nonlinear behavior, and by loading them with the self-weight and then by pushing with the self-weight applied in the horizontal direction. The model with 25 mm meshing size was considered as the benchmark and the base shear force and relevant displacement at a reference node were used as indicators of the mesh refinement. The obtained outcomes and the related errors (with respect to the benchmark models) are presented in Table 7. As it can be seen, the meshing size equal to 100 mm is sufficiently accurate to be used in the subsequent numerical investigation.

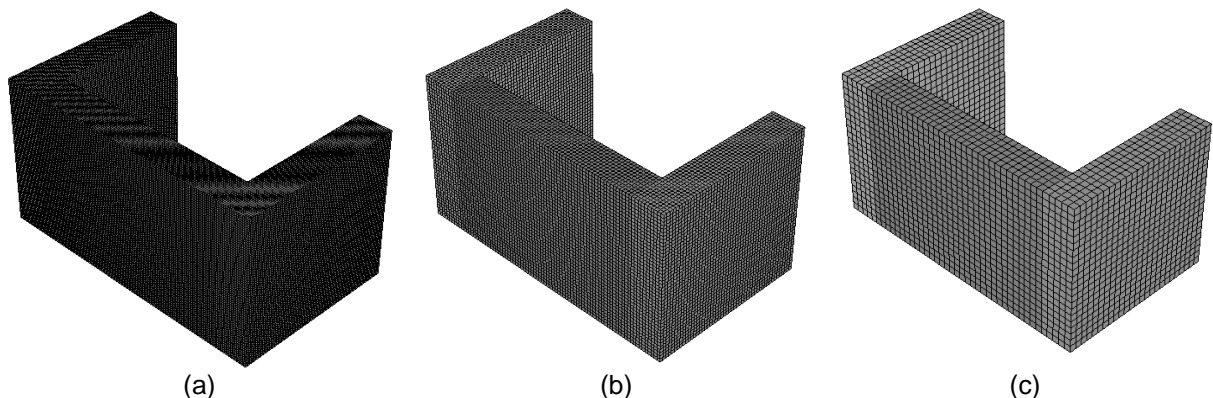


Figure 44 - Different considered mesh sizes of out-of-plane solid model: (a) mesh size = 25 mm (b) mesh size = 50 mm (c) mesh size = 100 mm

Table 7 – Results of the mesh refinement procedure of the models

Model	Mesh size = 25 mm		Mesh size = 50 mm		Mesh size = 100 mm	
	Horizontal Base Shear (kN)	Disp. (mm)	Horizontal Base Shear (kN) [Error %]	Disp. (mm) [Error %]	Horizontal Base Shear (kN) [Error %]	Disp. (mm) [Error %]
In-Plane Solid with 80 cm Wing	152.5	0.2577	153.12 [0.4%]	0.2577 [0.0%]	154.22 [1.11%]	0.258 [0.11%]
In-Plane Solid with 50 cm Wing	130.17	0.227	130.68 [0.39%]	0.227 [0.0%]	131.21 [0.79%]	0.227 [0.0%]
Out-of-Plane Solid	137.41	0.906	137.41 [0.0%]	0.906 [0.0%]	140.19 [1.98%]	0.903 [0.33%]
In-Plane Shell with 80 cm Wing	162.08	0.306	162.06 [0.01%]	0.306 [0.0%]	162.03 [0.03%]	0.306 [0.0%]
In-Plane Shell with 50 cm Wing	139.3	0.264	139.3 [0.0%]	0.264 [0.0%]	139.145 [0.11%]	0.265 [0.37%]
Out-of-Plane Shell	140.85	0.941	141.72 [0.61%]	0.946 [0.52%]	142.36 [1.06%]	0.946 [0.0%]

### 3.6. Model validation for self-weight

In order to validate the constructed models, the obtained reactions under gravity load (self-weight of the walls) were compared with the calculated weight of the walls. In this regard, the weights of the in-plane and out-of-plane components are given by equations (6) to (8).

$$W_{in-plane-80Wing} = \gamma \times V = \frac{2000 \times 9.81}{1000} \times [(2 \times 2.1 + 3.2) \times 0.5 \times 2.2] = 159.7 kN \quad (6)$$

$$W_{in-plane-50Wing} = \gamma \times V = \frac{2000 \times 9.81}{1000} \times [(2 \times 1.5 + 3.2) \times 0.5 \times 2.2] = 133.8 kN \quad (7)$$

$$W_{out-of-plane} = \gamma \times V = \frac{2000 \times 9.81}{1000} \times [(2 \times 2.0 + 4.2) \times 0.5 \times 2.2] = 176.97 kN \quad (8)$$

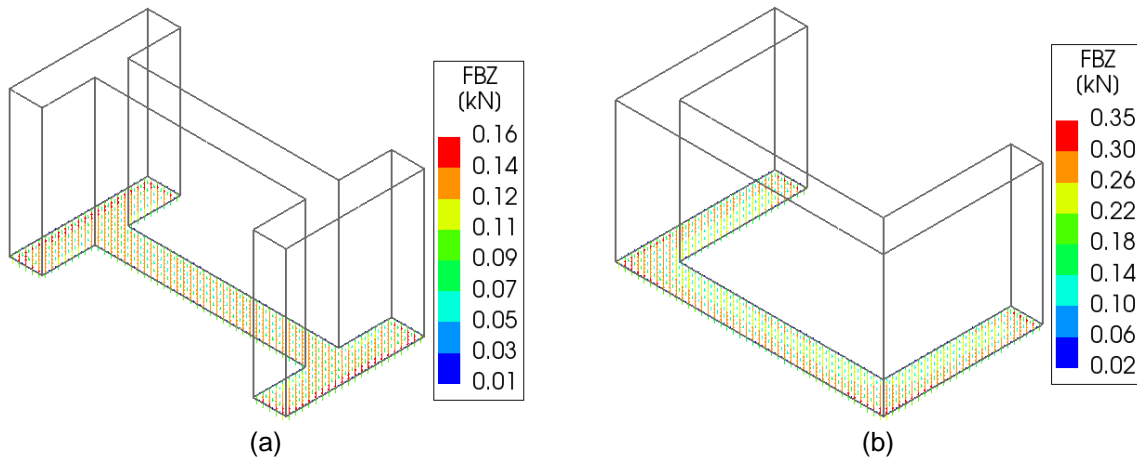


Figure 45- Reactions of the models under self-weight loading: (a) in-plane solid model (b) out-of-plane solid model

The reactions of the models under self-weight for all considered cases and their error with respect to the calculated values are reported in Table 8. As it can be seen, the error in all models is less than 8%, which is considered an acceptable limit in engineering judgments. It worth to mention that, the difference in shell models are arise from overlapping thicknesses due to considering the mid-section planes in the modeling (see Section 3.4).

Table 8 – Validation of constructed finite element models

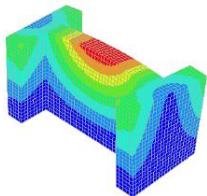
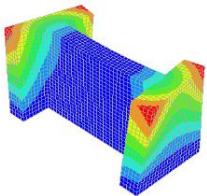
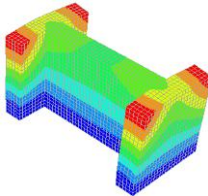
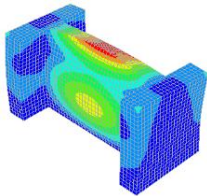
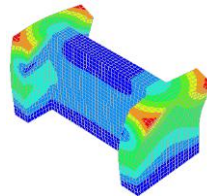
Model	Reaction (kN)	Error (%)
In-Plane Solid with 80 cm Wing	159.7	0.0
In-Plane Solid with 50 cm Wing	133.8	0.0
Out-of-Plane Solid	176.3	0.4
In-Plane Shell with 80 cm Wing	170.49	6.8
In-Plane Shell with 50 cm Wing	144.6	8.0
Out-of-Plane Shell	176.97	0.0

### 3.7. Modal analyses

In this section, the eigenvalue analysis is performed for all considered models. In this regard, the 20 first modes of vibration were verified to be sufficient to cover most of the modal mass participation in the dynamic behavior. The dynamic properties and corresponding mode shapes are presented in Table 9 to Table 14. Only the modes with the highest contribution are reported here, nevertheless all modes are presented in Appendix A. Moreover, the modes with the highest contributions are compared with both type 1 and 2 spectrums (far- and near-fields earthquakes) of the national Portuguese code (Norma Portuguesa, 2009) in Figure 46 to Figure 51. As it is evident, all of these modes are in the initial branch of the spectra. Therefore, considered components are sensitive to earthquakes with high-frequency contents, particularly within the elastic regimes. These spectra correspond to the seismological characteristics of the Alentejo region, which is discussed in detail in Chapter 5.

It can be seen from the presented results that the shell models lead to softer models. In other words, the period of corresponding modes in the shell models has greater period than that of the solid model. This situation is due to the mid-section consideration made in the shell model preparation. Furthermore, the obtained effective modal mass from the shell models are different with that of the solid models; whereas the captured mode shapes are similar in most of cases. It is worthwhile to note that only the order of corresponding modes (particularly higher modes) is different in the in-plane models.

Table 9 – Dynamic properties of the in-plane solid model with 80 cm wing length

Mode 1	Mode 3	Mode 4	Mode 8	Mode 13
				
$T_1 = 0.0448$ sec	$T_3 = 0.0306$ sec	$T_4 = 0.0289$ sec	$T_8 = 0.0135$ sec	$T_{13} = 0.01199$ sec
EMM <sub>x</sub> = 0.0 %	EMM <sub>x</sub> = 0.0 %	EMM <sub>x</sub> = 69.6 %	EMM <sub>x</sub> = 0.0 %	EMM <sub>x</sub> = 11.7 %
CEM <sub>x</sub> = 0.0 %	CEM <sub>x</sub> = 0.0 %	CEM <sub>x</sub> = 69.6 %	CEM <sub>x</sub> = 69.6 %	CEM <sub>x</sub> = 82.3 %
EMM <sub>y</sub> = 39.6 %	EMM <sub>y</sub> = 23.2 %	EMM <sub>y</sub> = 0.0 %	EMM <sub>y</sub> = 11.3 %	EMM <sub>y</sub> = 0.0 %
CEM <sub>y</sub> = 39.6 %	CEM <sub>y</sub> = 62.8 %	CEM <sub>y</sub> = 62.8 %	CEM <sub>y</sub> = 75.4 %	CEM <sub>y</sub> = 75.4 %

Where,  $T_i$  is period of  $i$ -th mode, EMM is the effective modal mass and CEM is cumulative effective mass.



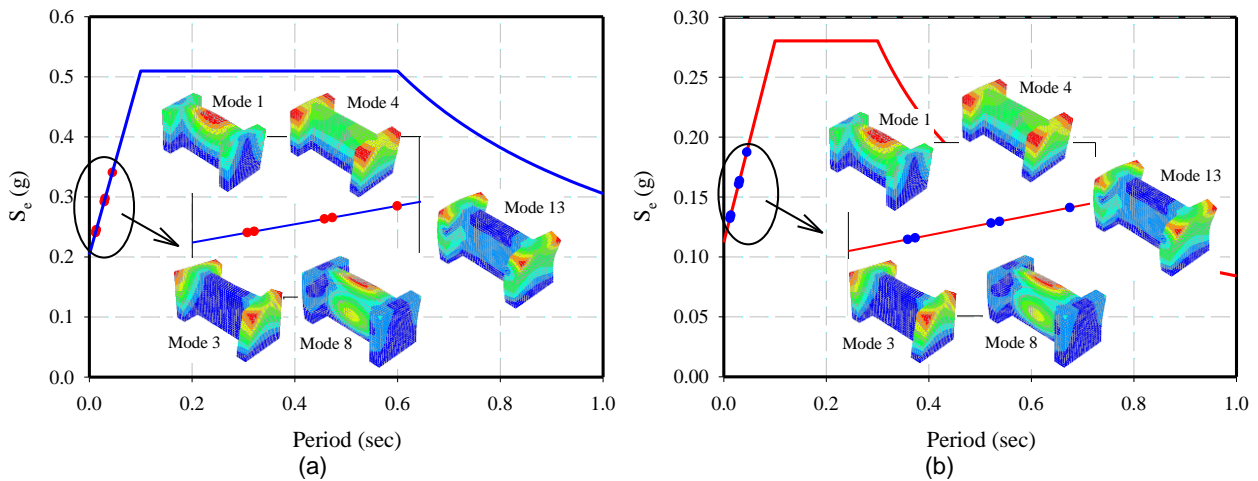


Figure 46- Highest contributing modes of the in-plane solid model with 80 cm wing and comparison with the design spectrums: (a) spectrum type 1 (far-field earthquake) (b) spectrum type 2 (near-field earthquake)

Table 10 – Dynamic properties of the in-plane solid model with 50 cm wing length

Mode 1	Mode 4	Mode 8	Mode 10	Mode 14
$T_1 = 0.0502$ sec	$T_4 = 0.0261$ sec	$T_8 = 0.0137$ sec	$T_{10} = 0.0118$ sec	$T_{14} = 0.0106$ sec
EMM <sub>x</sub> = 0.0 %	EMM <sub>x</sub> = 72.2 %	EMM <sub>x</sub> = 0.0 %	EMM <sub>x</sub> = 6.4 %	EMM <sub>x</sub> = 0.0 %
CEM <sub>x</sub> = 0.0 %	CEM <sub>x</sub> = 72.2 %	CEM <sub>x</sub> = 72.2 %	CEM <sub>x</sub> = 78.6 %	CEM <sub>x</sub> = 78.6 %
EMM <sub>y</sub> = 55.8 %	EMM <sub>y</sub> = 0.0 %	EMM <sub>y</sub> = 15.1 %	EMM <sub>y</sub> = 0.0 %	EMM <sub>y</sub> = 6.3 %
CEM <sub>y</sub> = 55.8 %	CEM <sub>y</sub> = 62.5 %	CEM <sub>y</sub> = 77.6 %	CEM <sub>y</sub> = 77.6 %	CEM <sub>y</sub> = 84.0 %

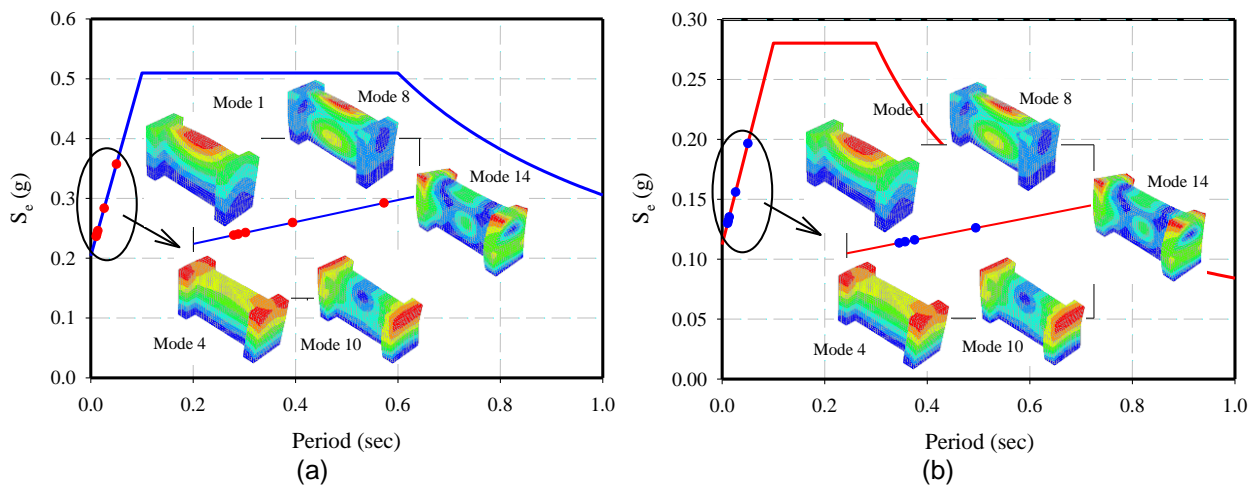
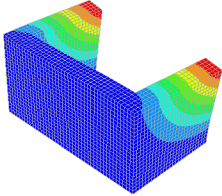
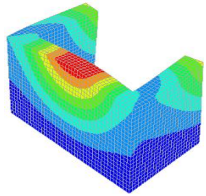
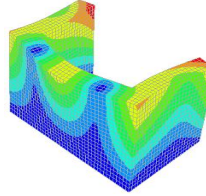
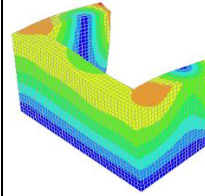
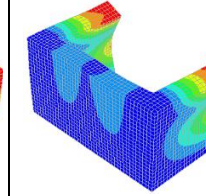


Figure 47- Highest contributing modes of the in-plane solid model with 50 cm wing and comparison with the design spectrums: (a) spectrum type 1 (far-field earthquake) (b) spectrum type 2 (near-field earthquake)

Table 11 – Dynamic properties of the out-of-plane solid model from modal analysis

Mode 2	Mode 3	Mode 5	Mode 6	Mode 9
				
$T_2 = 0.0518$ sec EMM <sub>X</sub> = 32.1 % CEM <sub>X</sub> = 32.1 % EMM <sub>Y</sub> = 0.0 % CEM <sub>Y</sub> = 4.4 %	$T_3 = 0.0390$ sec EMM <sub>X</sub> = 0.0 % CEM <sub>X</sub> = 32.1 % EMM <sub>Y</sub> = 40.0 % CEM <sub>Y</sub> = 44.4 %	$T_5 = 0.0243$ sec EMM <sub>X</sub> = 0.0 % CEM <sub>X</sub> = 36.5 % EMM <sub>Y</sub> = 21.4 % CEM <sub>Y</sub> = 65.8 %	$T_6 = 0.0232$ sec EMM <sub>X</sub> = 28.7 % CEM <sub>X</sub> = 65.3 % EMM <sub>Y</sub> = 0.0 % CEM <sub>Y</sub> = 65.8 %	$T_9 = 0.0147$ sec EMM <sub>X</sub> = 8.3 % CEM <sub>X</sub> = 78.1 % EMM <sub>Y</sub> = 0.0 % CEM <sub>Y</sub> = 66.7 %

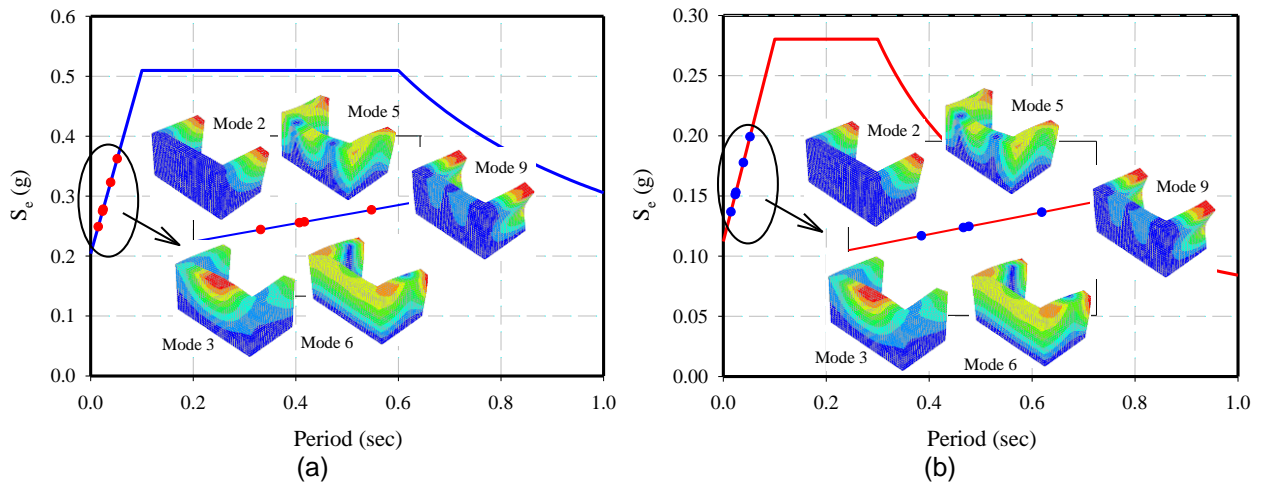
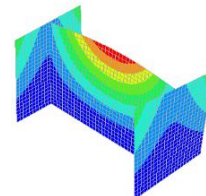
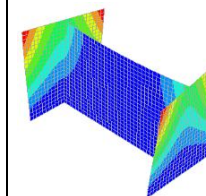
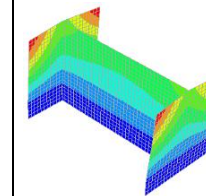
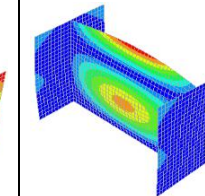
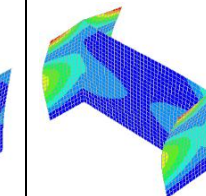


Figure 48- Highest contributing modes of the out-of-plane solid model and comparison with the design spectrums: (a) spectrum type 1 (far-field earthquake) (b) spectrum type 2 (near-field earthquake)

Table 12 – Dynamic properties of the in-plane shell model with 80 cm wing length

Mode 1	Mode 3	Mode 4	Mode 10	Mode 12
				
$T_1 = 0.0479$ sec EMM <sub>X</sub> = 0.0 % CEM <sub>X</sub> = 0.0 % EMM <sub>Y</sub> = 40.1 % CEM <sub>Y</sub> = 40.1 %	$T_3 = 0.0318$ sec EMM <sub>X</sub> = 0.0 % CEM <sub>X</sub> = 0.0 % EMM <sub>Y</sub> = 21.0 % CEM <sub>Y</sub> = 61.1 %	$T_4 = 0.0313$ sec EMM <sub>X</sub> = 67.2 % CEM <sub>X</sub> = 67.2 % EMM <sub>Y</sub> = 0.0 % CEM <sub>Y</sub> = 61.1 %	$T_{10} = 0.0141$ sec EMM <sub>X</sub> = 0.0 % CEM <sub>X</sub> = 70.4 % EMM <sub>Y</sub> = 11.2 % CEM <sub>Y</sub> = 75.3 %	$T_{12} = 0.0128$ sec EMM <sub>X</sub> = 11.9 % CEM <sub>X</sub> = 82.3 % EMM <sub>Y</sub> = 0.0 % CEM <sub>Y</sub> = 75.3 %

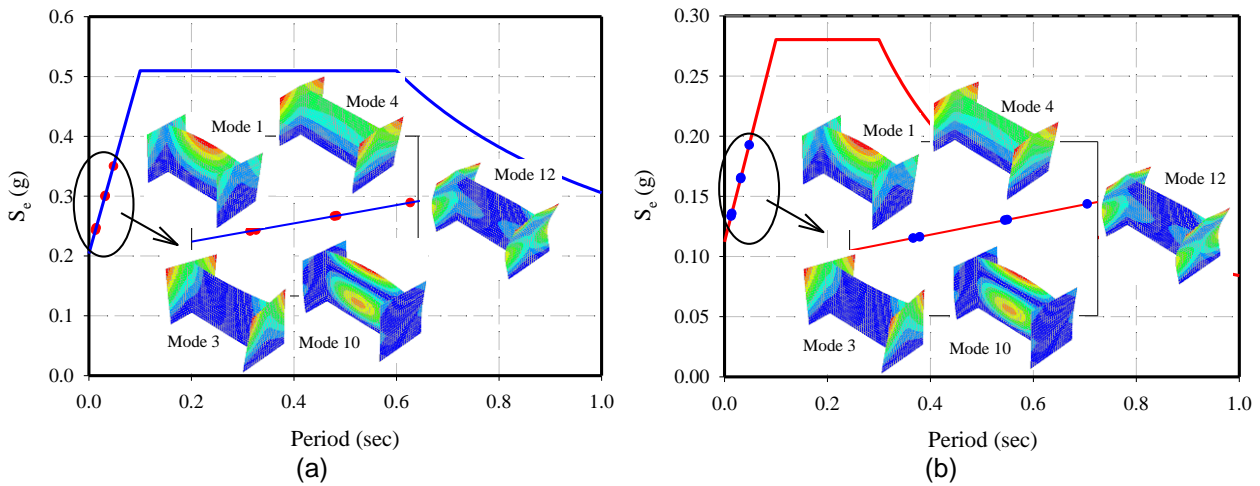


Figure 49- Highest contributing modes of the in-plane shell model with 80 cm wing and comparison with the design spectrums: (a) spectrum type 1 (far-field earthquake) (b) spectrum type 2 (near-field earthquake)

Table 13 – Dynamic properties of the in-plane shell model with 50 cm wing length

Mode 1	Mode 4	Mode 8	Mode 11	Mode 15
$T_1 = 0.0533$ sec	$T_4 = 0.0280$ sec	$T_8 = 0.0143$ sec	$T_{11} = 0.0120$ sec	$T_{15} = 0.0109$ sec
EMM <sub>x</sub> = 0.0 %	EMM <sub>x</sub> = 71.1 %	EMM <sub>x</sub> = 0.0 %	EMM <sub>x</sub> = 6.9 %	EMM <sub>x</sub> = 0.0 %
CEM <sub>x</sub> = 0.0 %	CEM <sub>x</sub> = 71.1 %	CEM <sub>x</sub> = 71.1 %	CEM <sub>x</sub> = 78.0 %	CEM <sub>x</sub> = 82.7 %
EMM <sub>y</sub> = 54.7 %	EMM <sub>y</sub> = 0.0 %	EMM <sub>y</sub> = 14.5 %	EMM <sub>y</sub> = 0.0 %	EMM <sub>y</sub> = 6.5 %
CEM <sub>y</sub> = 54.7 %	CEM <sub>y</sub> = 62.7 %	CEM <sub>y</sub> = 77.2 %	CEM <sub>y</sub> = 77.2 %	CEM <sub>y</sub> = 83.7 %

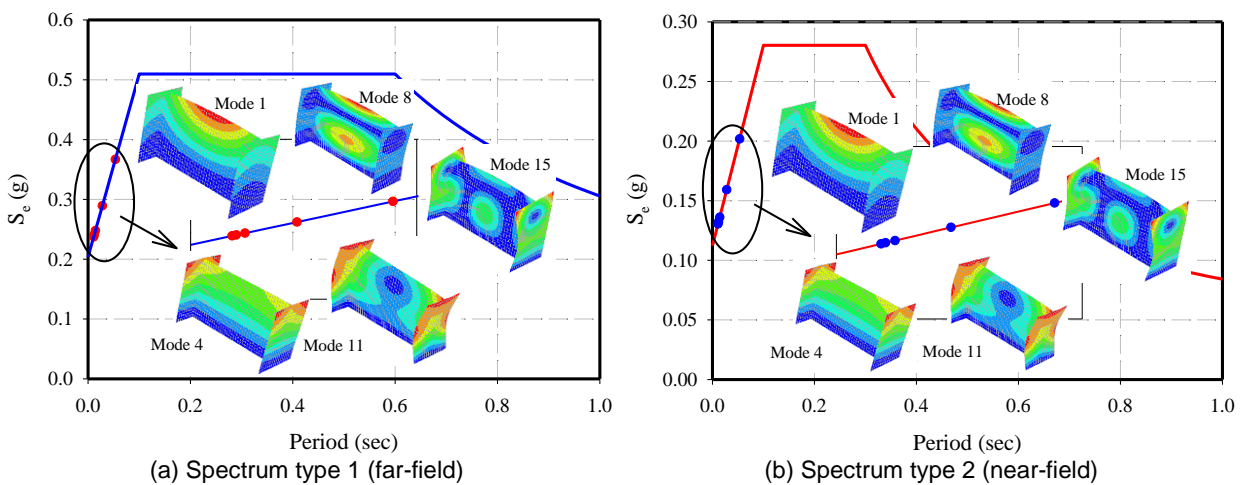
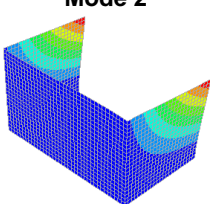
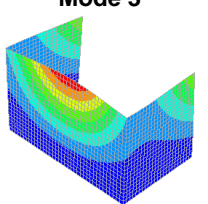
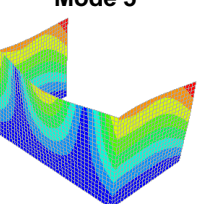
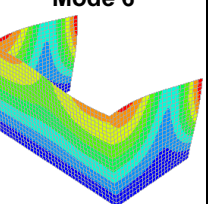
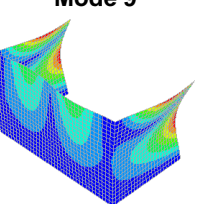


Figure 50- Highest contributing modes of the in-plane shell model with 50 cm wing and comparison with the design spectrums: (a) spectrum type 1 (far-field earthquake) (b) spectrum type 2 (near-field earthquake)

Table 14 – Dynamic properties of the out-of-plane shell model

Mode 2	Mode 3	Mode 5	Mode 6	Mode 9
				
$T_2 = 0.0546$ sec	$T_3 = 0.0422$ sec	$T_5 = 0.0248$ sec	$T_6 = 0.0239$ sec	$T_9 = 0.0152$ sec
EMM <sub>x</sub> = 33.4 %	EMM <sub>x</sub> = 0.0 %	EMM <sub>x</sub> = 0.0 %	EMM <sub>x</sub> = 26.0 %	EMM <sub>x</sub> = 9.0 %
CEM <sub>x</sub> = 33.4 %	CEM <sub>x</sub> = 33.4 %	CEM <sub>x</sub> = 37.5 %	CEM <sub>x</sub> = 63.5 %	CEM <sub>x</sub> = 78.0 %
EMM <sub>y</sub> = 0.0 %	EMM <sub>y</sub> = 37.5 %	EMM <sub>y</sub> = 23.0 %	EMM <sub>y</sub> = 0.0 %	EMM <sub>y</sub> = 0.0 %
CEM <sub>y</sub> = 5.1 %	CEM <sub>y</sub> = 42.6 %	CEM <sub>y</sub> = 65.6 %	CEM <sub>y</sub> = 65.6 %	CEM <sub>y</sub> = 66.4 %

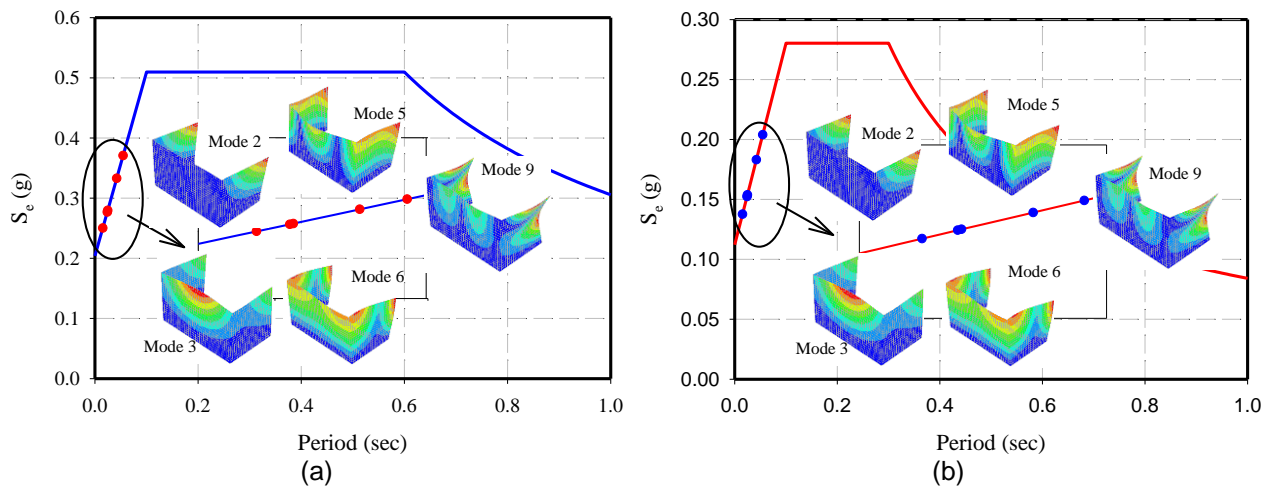


Figure 51- Highest contributing modes of the out-of-plane shell model and comparison with the design spectrums: (a) spectrum type 1 (far-field earthquake) (b) spectrum type 2 (near-field earthquake)

### 3.8. Pushover analyses

As it was previously referred in the literature, pushover analyses may lead to acceptable mean responses in comparison with nonlinear dynamic (time-history) analyses, but the damage pattern produced is likely to differ significantly. On the other hand, the probability of under-estimating the maximum lateral displacements can go beyond acceptable limits (Allahvirdizadeh and Gholipour, 2017). In spite of that, pushover analyses are expected to provide an initial and general overview on the behavior of the considered models. Therefore, this section presents the outcomes of nonlinear static analyses performed for analyzing the behavior of the unstrengthened models. In this regard, a mass-proportional lateral load pattern was applied to push the models. This is done in the principal directions of each wall, i.e. in the x-direction for in-plane models and y-direction for out-of-plane ones. Due to un-symmetric geometry of the out-of-plane models, the analyses are performed for both

positive and negative directions. It should be noted that, the results are presented in two stages, i.e. damage initiation stage and the peak capacity.

### 3.8.1. In-plane models

In this section, the behavior of the unstrengthened in-plane models is investigated by means of pushover analyses. In this regard, not only a general overview about the seismic behavior of the walls is obtained, but also the modeling approach (i.e. shell or solid) showing the best compromise between accuracy of results and computational effort is selected for subsequent numerical investigation.

The pushover curves (representing the normalized base shear to the weight of the structural wall as a function of displacement of the control nodes) obtained for the in-plane models, are illustrated in Figure 52 and Figure 53, for the models with 80 cm and 50 cm wings, respectively. The lateral displacement of three nodes was controlled, namely on top of the left and right wings, and on top of the middle section of the web. In all cases the right wing (the wing which wall is leaned on during the push) controls the behavior; while the captured lateral displacement in the shell models is greater than that of the solid ones. Nevertheless, a minor increase in peak capacity is observed from the shell to the solid models.

The point of damage initiation of the models is also highlighted in the curves, which corresponds to the onset of the opening of cracks. As it can be seen, this state occurs for very low values of the imposed lateral loading, evidencing the great influence of the nonlinear behavior of the rammed earth on the structural behavior.

The models with 50 cm wing achieve higher load and displacement capacities than those of the models with 80 cm wings. It is also true that the damage initiation occurs earlier for the models with 80 cm wings. This difference in behavior is explained by the influence of the out-of-plane bending of wings on the response, where the higher their length the earlier is the damage initiation. Thus, a response of the models governed by the in-plane behavior by formation of diagonal cracks in the web wall is very unlikely to be dominant failure mode in the models with 80 cm wings, since these massive web sections induced higher bending stresses. It should be noted that these aspects are further discussed with the investigation on strains and stresses developing in the models. As it was previously mentioned, experimental models with similar geometry to that of the numerical models are expected to be tested on shaking table, hence due to stability concerns during the tests the wings cannot be eliminated. Therefore, it is of utmost interest to find the dimensions that satisfy not only the experimental issues but also represent desired lateral behavior of the rammed earth walls.

With respect to the failure mode evidenced by the models, when the response is considered by the left wing and the mid web nodes, it is possible to observe that an apparent unloading occurs in the post peak behavior. This situation can be explained by the possible detachment between the right wing and the web wall. Such detachment increases displacements on the right wing, whereas the left wing and the web unload. It can be understood from the presented curves that the peak capacity is same for all

controlling nodes, while the peak displacement capacity considerably differs from point to point. It is clear that, the sway of the right wing cannot be interpreted entirely as ductility of the model.

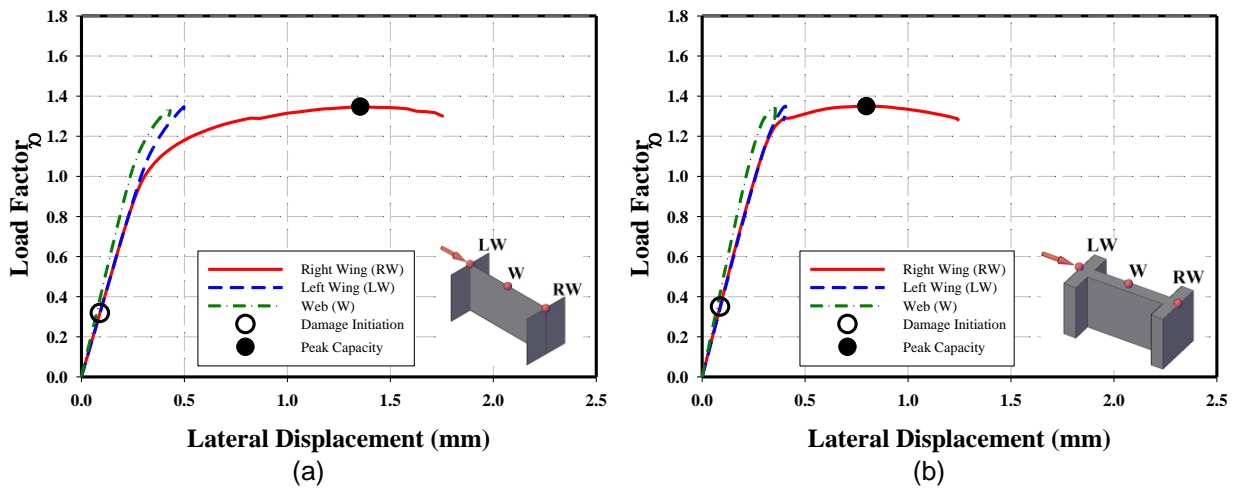


Figure 52 – Pushover curves of the unstrengthened in-plane models with 80 cm wings: (a) shell model (b) solid model

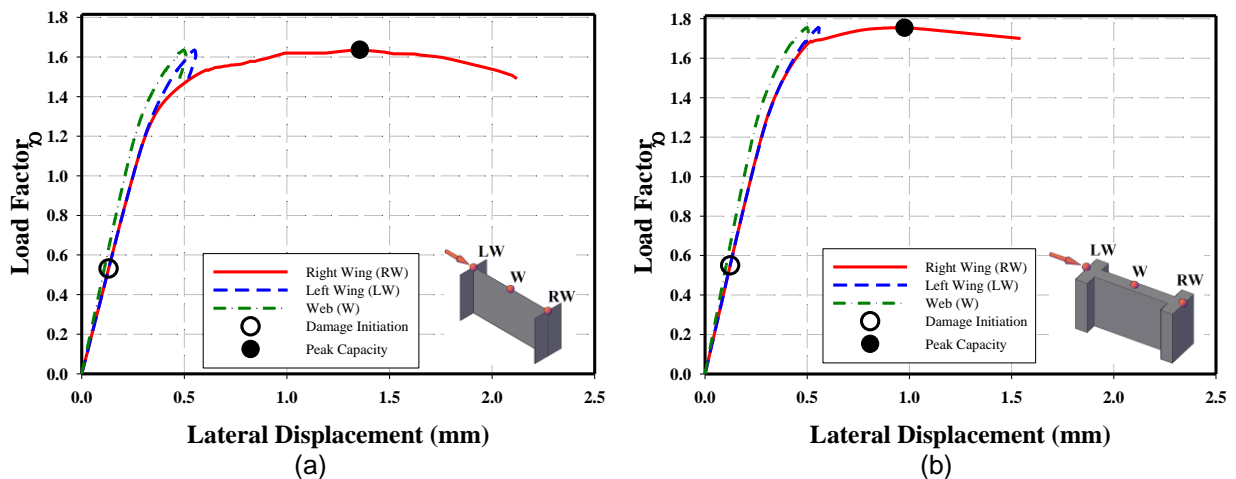


Figure 53 – Pushover curves of the unstrengthened in-plane models with 50 cm wings: (a) shell model (b) solid model

The above figures also show that the models have an apparent linear development even after damage initiation. In this regard, the damage state of the solid in-plane model with 50 cm wings was assessed by considering the principal compression stress and principal tensile strain distributions at this point (see Figure 54). For sake of brevity, the results of the other models are not presented. As it is evidenced, initiated damage occurred locally. The compression stresses developed at the connection between the web and the right wing and also at its toe show that these are the most stressed zones, due to the kind of rocking movement of the model. On the other hand, the principal tensile strains are developing in a minor region located at the connection of the web and the left wing. Therefore, the initiated damage is very local, and thus much higher demand is required to force the wall to undergo nonlinearity.

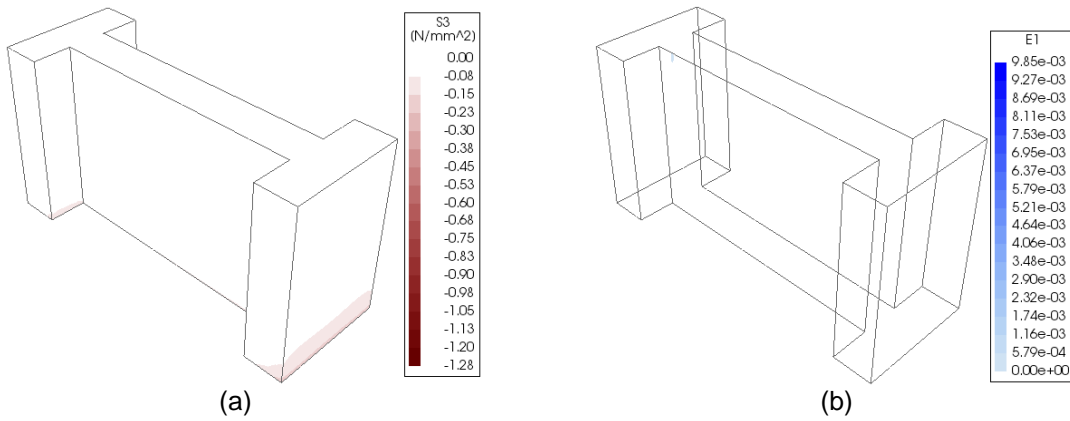


Figure 54 – Damage representation of the solid in-plane model with 50 cm wings at the damage initiation step: (a) principal compressive stress (b) principal tensile strain

The contour map of the total lateral displacement in x-direction for the in-plane models (shell and solid models) at the peak capacity are shown in Figure 55 and Figure 56, respectively for the models with 80 cm and 50 cm wings.

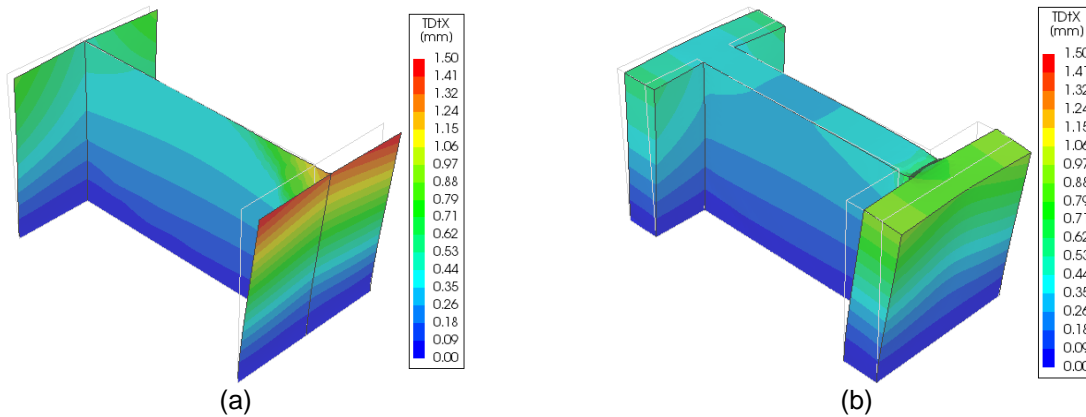


Figure 55 – Total lateral displacements at the peak capacity of the in-plane models with 80 cm wings:  
(a) shell model (b) solid model

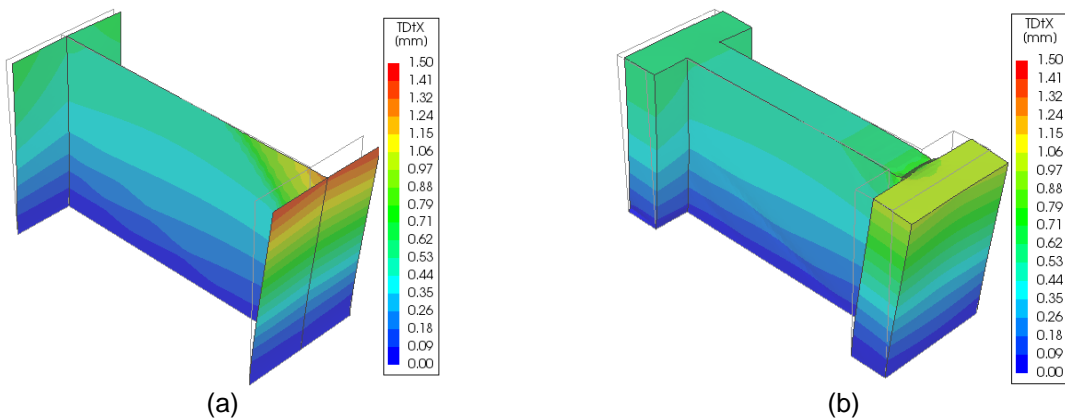


Figure 56 – Total lateral displacements at the peak capacity of the in-plane models with 50 cm wings:  
(a) shell model (b) solid model

As it can be seen, the shell models experienced higher lateral displacements at the right wings. This behavior is a consequence of the thickness disregard of the web, where the supporting effect is not simulated in its full extension, meaning that the wings are considered with longer effective lengths and are more easily bended. Thus, it can be stated that the thickness disregard of the shell models may lead to the prediction of unreliable failure mechanisms and capacities.

To assess the load paths through the models and highlight the regions with damage concentration, the principal compressive stresses and the principal tensile strains were also analyzed. The principal compressive stresses at the peak capacity are presented in Figure 57 and Figure 58 for the models with 80 cm and 50 cm wings, respectively.

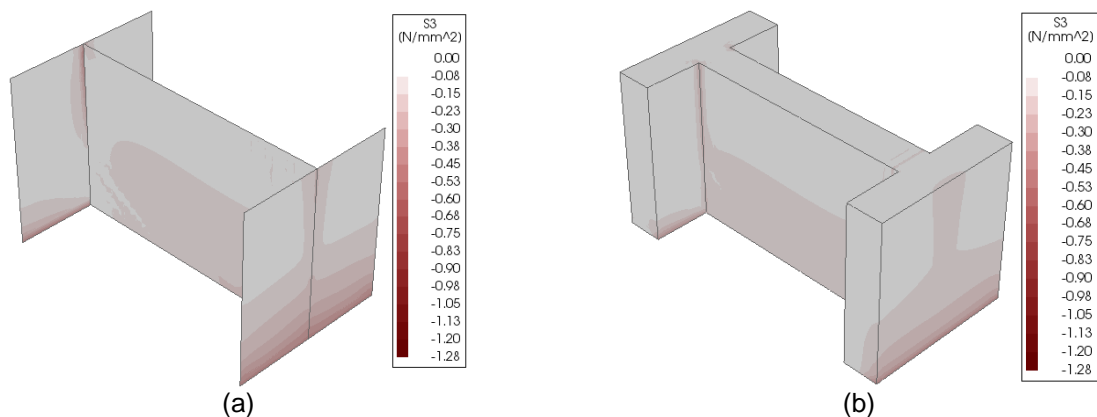


Figure 57 – Principal compressive stresses at the peak capacity for the in-plane models with 80 cm wings: (a) shell model (b) solid model

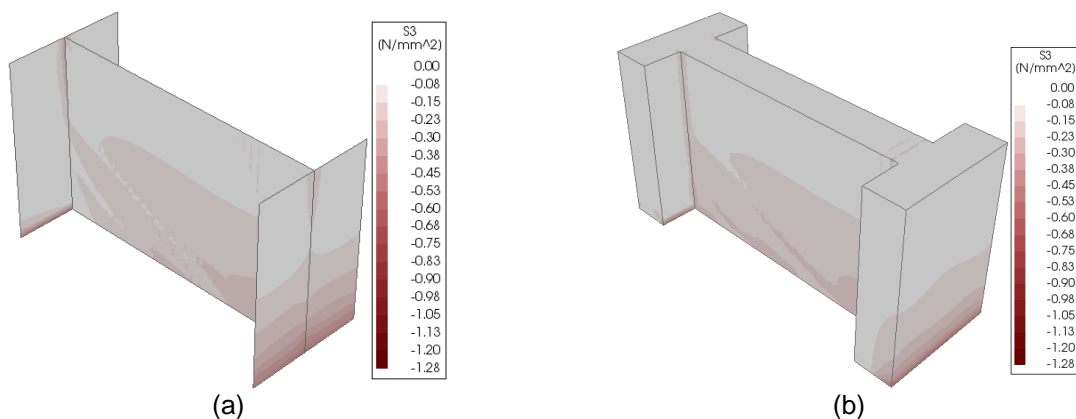


Figure 58 – Principal compressive stresses at the peak capacity for the in-plane model with 50 cm wings: (a) shell model (b) solid model

As it can be seen, the compressive stresses in the wall with 80 cm wings are mostly concentrated on the right wing, whereas it was expected that the in-plane models were transferring the loads by means of diagonal struts in the web wall. Nevertheless the onset of the load distribution mechanism can be observed in the model with 50 cm wings, but it is not fully developed. As stated in previously, it is believed not to be possible to remove the wings due to the stability conditions required during the experimental tests, meaning that it is probably not possible to fully develop the shear capacity of the



web wall. Then, it can be concluded that the in-plane wall with 50 cm wings has a response that is more in agreement with the intended behavior of the experimental models. Furthermore, the contour map of the solid model in comparison of that of the shell one, illustrates more representative outcomes; especially in the regions of the connection between the web and the wings, where stress concentrations in the shell model seems to show a less efficient stress distribution.

The principal tensile strains were also analyzed following the similar approach to that of the analysis of the principal compressive stresses. The respective contours are presented in Figure 59 and Figure 60 for the models with 80 cm and 50 cm wings, respectively.

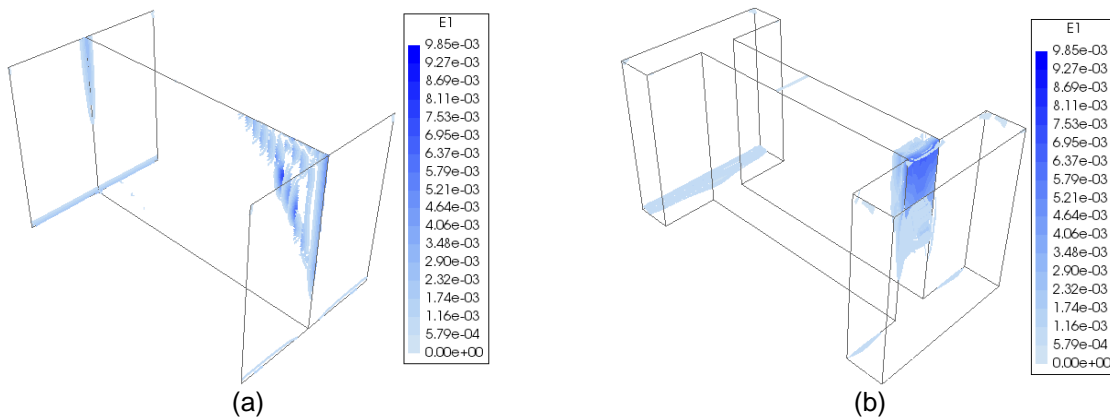


Figure 59 – Principal tensile strains at the peak capacity of the in-plane models with 80 cm wings: (a) shell model (b) solid model

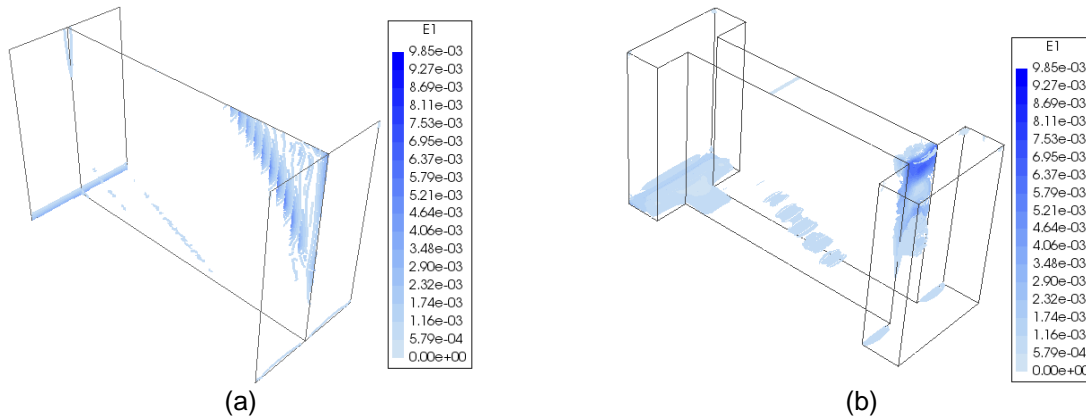


Figure 60 – Principal tensile strains at the peak capacity of the in-plane models with 50 cm wings: (a) shell model (b) solid model

The connection of the web and the right wing is the region with the highest values of tensile strains, indicating that this region is more likely to control the response of the in-plane models and to concentrate the cracking process. Again, the difference between the solid and the shell models are evident, namely with respect to the undesirable distribution of damage in the web of the shell model near the right wing. On the other hand, no diagonal cracks are detected in the model with 80 cm wings, showing the absence of the shear failure of the web, as initially expected. In the case of the model with 50 cm wings, the formation of diagonal cracks is evident, even though not in its full

extension, meaning that this model is more representative of the expected behavior for the experimental models. By considering above discussion and conclusions, the subsequent studies will only consider the solid in-plane model with 50 cm wing length.

### 3.8.2. Out-of-plane models

In this section, a similar approach to that of Section 3.8.1 is followed for the unstrengthened out-of-plane models. Due to asymmetrical geometry of the corresponding wall in one of its main axis, the models were pushed in the positive (inside) and negative (outside) directions. The obtained pushover curves are shown in Figure 61 and Figure 62. As it was expected, pushing in the negative direction results in less load and displacement capacities. This behavior is a consequence of a less effective supporting contribution of wings in this direction. The lack of this contribution is also true for explaining the earlier damage initiation of the models pushed in the negative direction. For instance, in the case of the solid model pushed in the negative direction, the damage onset occurs for a base shear ratio of approximately 0.2, whereas in the case of the same model pushed in the positive direction this value is of about 0.4. Thus, it is clear that the lowest capacity should be considered for assessment purposes. Moreover, and similarly to the observed for the in-plane models, the out-of-plane shell model leads to greater lateral displacements than those of the solid one, while there is no clear relation between the modeling approach and the obtained load capacities.

It is also essential to take into account the post peak behavior of the wall under the two pushing conditions. The behavior of the models in the negative direction experiences a sudden drop immediately after the peak, while pushing it in the positive direction produces a smooth degradation of capacity. In other words, the wall shows a brittle response if pushed outside of the wings, explained by the overturning of the web due to the loss of connection with the wings; on the other hand, when the models are pushed towards the wings, the connections are compressed, meaning that the wings are able to counteract the overturning movement.

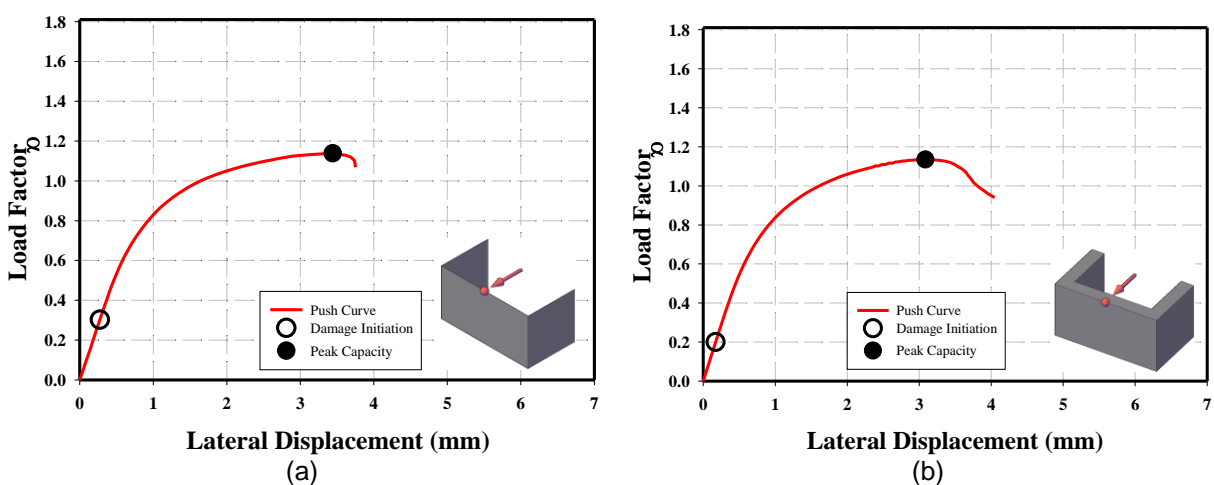


Figure 61 – Pushover curves of the unstrengthened out-of-plane models pushed in the negative direction: (a) shell model (b) solid model

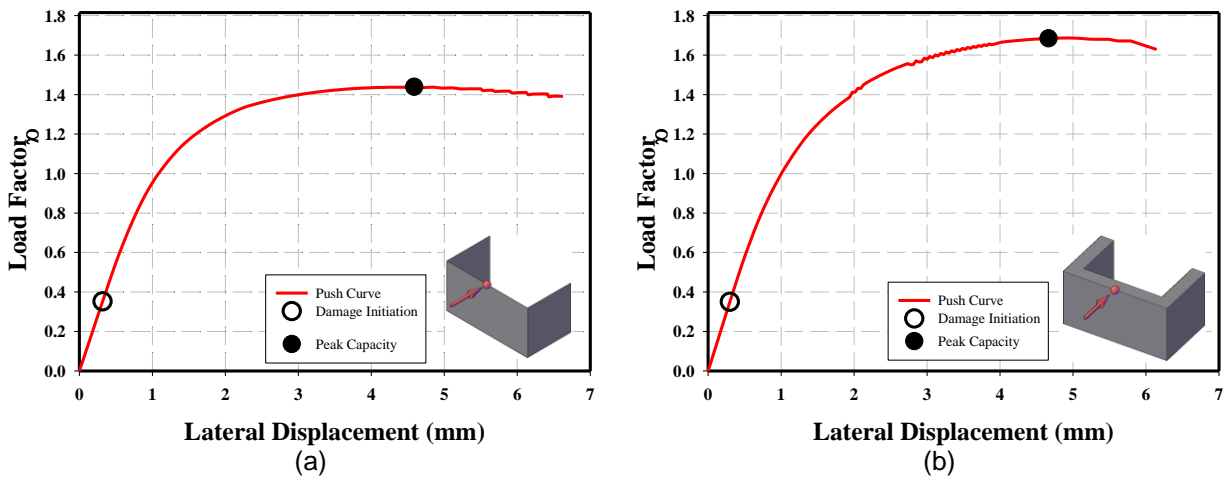


Figure 62 – Pushover curve of the unstrengthened out-of-plane models pushed in the positive direction: (a) shell model (b) solid model

The total lateral displacement contours at the peak capacity are shown in Figure 63 and Figure 64 for the negative and positive pushing directions, respectively. As it was expected, in both cases the middle of the web experienced the highest lateral displacements. It should be noted that in the solid models a portion of the wings collaborates in the out-of-plane response of the wall, while in the shell this contribution seems incipient, since the thickness of the walls is disregarded in this last case. The absence of this contribution seems to be a major aspect explaining the different capacities exhibited between the pushover curves of the shell and solid models. Furthermore, the contour maps reveal different contribution levels of the wing walls in the models considering different modeling approaches and pushing directions.

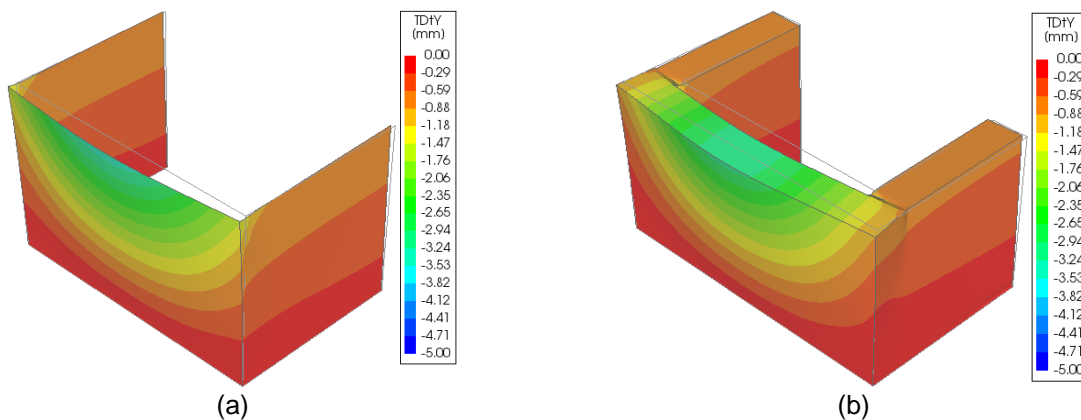


Figure 63 – Total lateral displacements at the peak capacity of the out-of-plane models pushed in the negative direction: (a) shell model (b) solid model

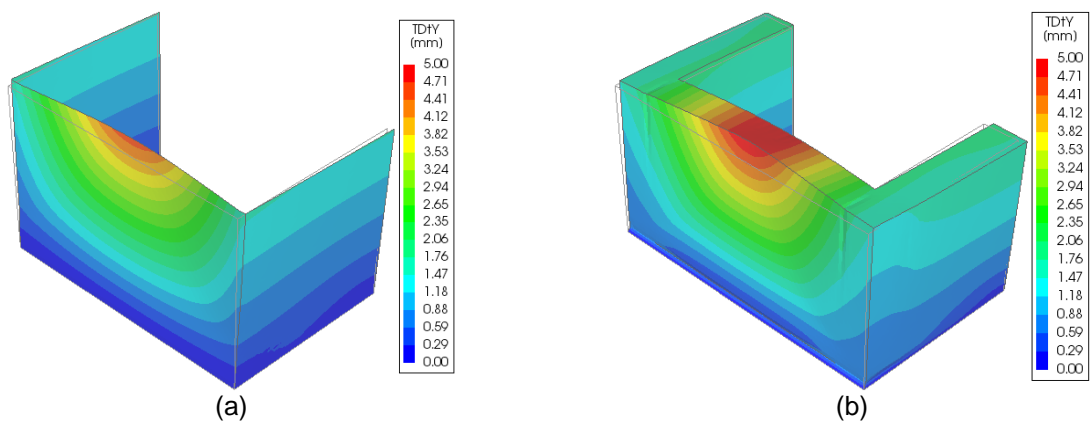


Figure 64 – Total lateral displacements at the peak capacity of the out-of-plane models pushed in the positive direction: (a) shell model (b) solid model

The principal compressive stresses at the peak capacity are presented in Figure 65 and Figure 66, respectively for the models pushed in the negative and positive directions. A diagonal compressive strut is observed in the solid model pushed in the negative direction, while a completely different behavior is captured by the shell model. From a general point of view, the compressive principal stresses in the solid model seem to be more compatible with expected out-of-plane response of the wall, which is probably detachment of the web from the wings and overturning.

Moreover, an evident arch effect is observed on both shell and solid models pushed in the positive direction. This effect can also be interpreted as the bending occurring at the middle section of the web. It can also be seen that the lateral loads induced by the web are transferred to the wings by aforementioned arch effect in web wall. These compressive stresses are then transferred to the wings' toes by a compression strut which deems this region as that presenting the highest compressive stresses of the model. In the case of the solid model pushed in the negative direction, also a small strut along the thickness of the web is observed to transmit the compressive stresses of wings to the toe of the web wall.

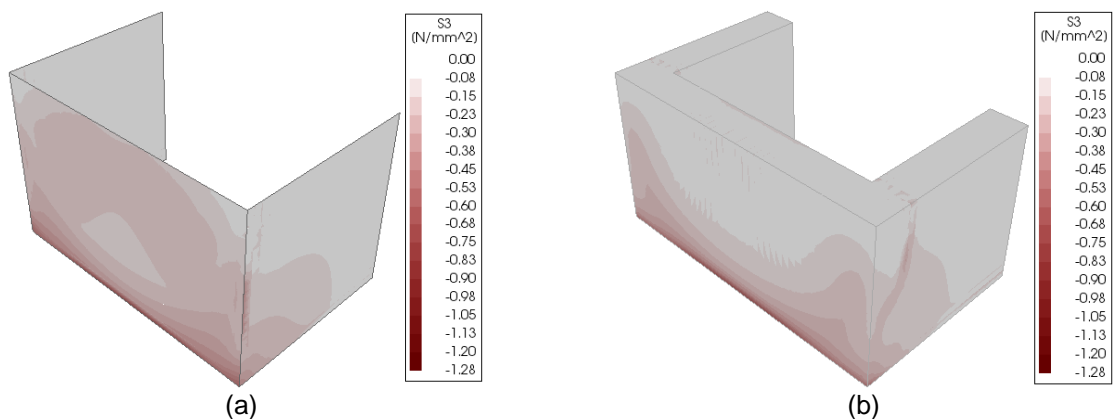


Figure 65 – Principal compressive stresses at the peak capacity of the out-of-plane models pushed in the negative direction: (a) shell model (b) solid model

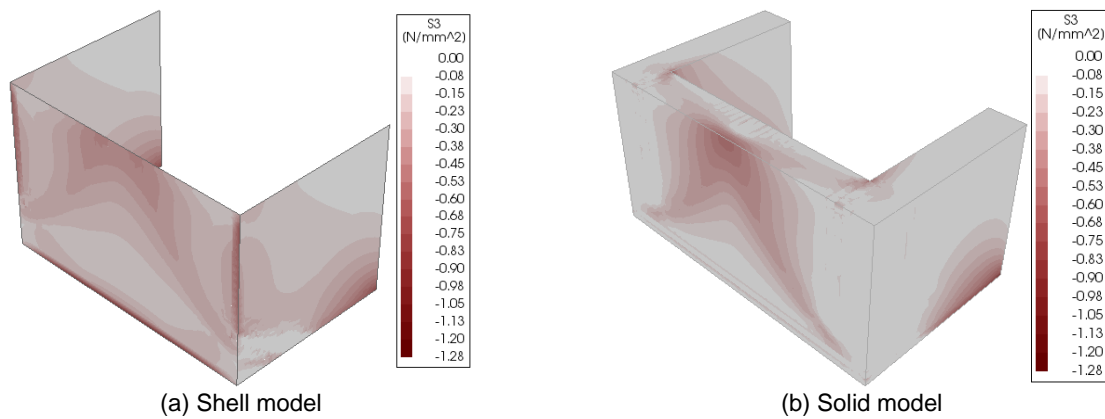


Figure 66 – Principal compressive stresses at the peak capacity of the out-of-plane models pushed in the positive direction: (a) shell model (b) solid model

The contours of the principal tensile strains are also presented in Figure 67 and Figure 68, respectively for the models pushed in the negative and positive directions. The same observations outlined for the principal compressive stresses can be applied for these results. Furthermore, it is evident that when the models are pushed in the negative direction, the web wall tends to detach from the wings, especially in the upper sections. The tensile strains at the base of the models pushed in the negative direction seem to indicate that the web wall is likely to be overturning, while for the models pushed in the positive direction, the whole model seems to be overturning.

In conclusion, the solid modeling approach seems to lead to more reliable outcomes of the out-of-plane behavior, meaning that the subsequent numerical investigation will only consider the solid model.

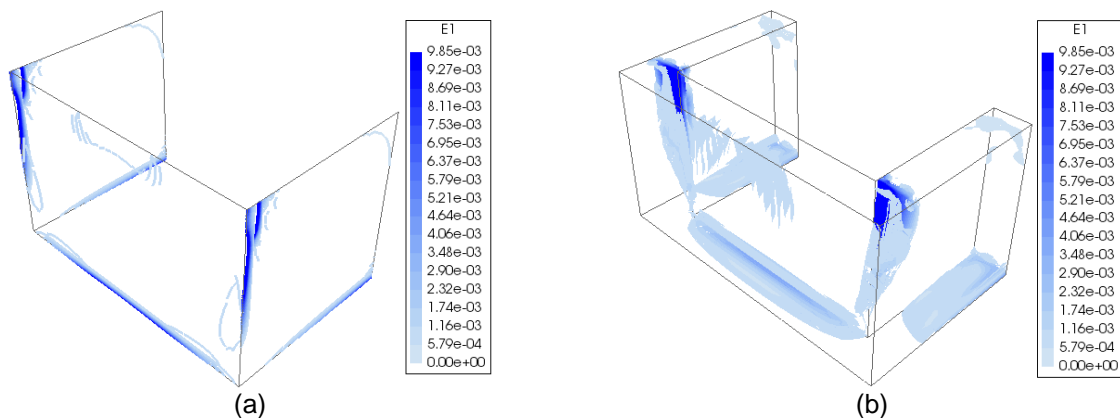


Figure 67 – Principal tensile strains at the peak capacity of the out-of-plane models pushed in the negative direction: (a) shell model (b) solid model

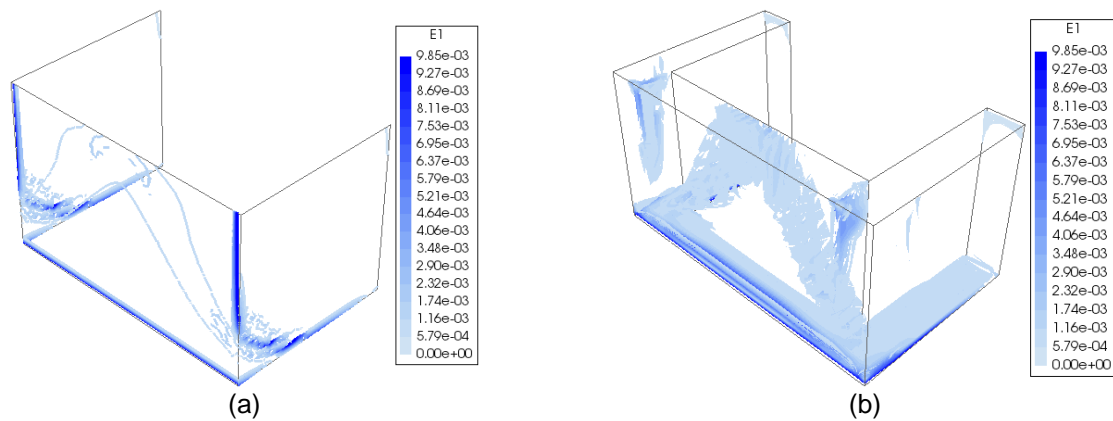


Figure 68 – Principal tensile strains at the peak capacity of the out-of-plane models pushed in the positive direction: (a) shell model (b) solid model

### 3.9. Influence of the damage on the dynamic properties

During the pushover analyses, the damage initiates and develops within the models, leading to a progressive reduction of the stiffness. In this regard, eigenvalue analyses were conducted at different steps of the solid models, starting with the initial undamaged condition up to the peak capacity. The changes in frequencies were here adopted as an indicator of damage state in unstrengthened walls. The performed eigenvalue analyses confirmed the progressive reduction in frequencies of the models with damage progression, and demonstrated that the damage also changes the mode shapes and modal mass contributions of the modes. Therefore and for the sake of simplicity, the three modes with the highest effective mass contribution in the undamaged condition were selected to study the reductions in frequencies. Furthermore, the mode shapes of these selected modes were also considered in each step to find the most compatible modes. As the order of the modes was not necessarily the same in all considered steps, they are called hereafter as high participating modes (HM). The frequencies of each HM were normalized to the initial frequency value (corresponding to the state with no damage) and outcomes are presented in Figure 69 as a function of the corresponding displacement at the middle web section. As it can be seen, the greatest frequency reduction is typically to the mode with the highest contribution. In general, the reductions at peak load are greater in the out-of-plane models than in the in-plane model. Furthermore, it is possible to observe that pushing the out-of-plane model in the negative direction (outside) leads apparently to higher damage levels than when it is pushed in the positive direction.

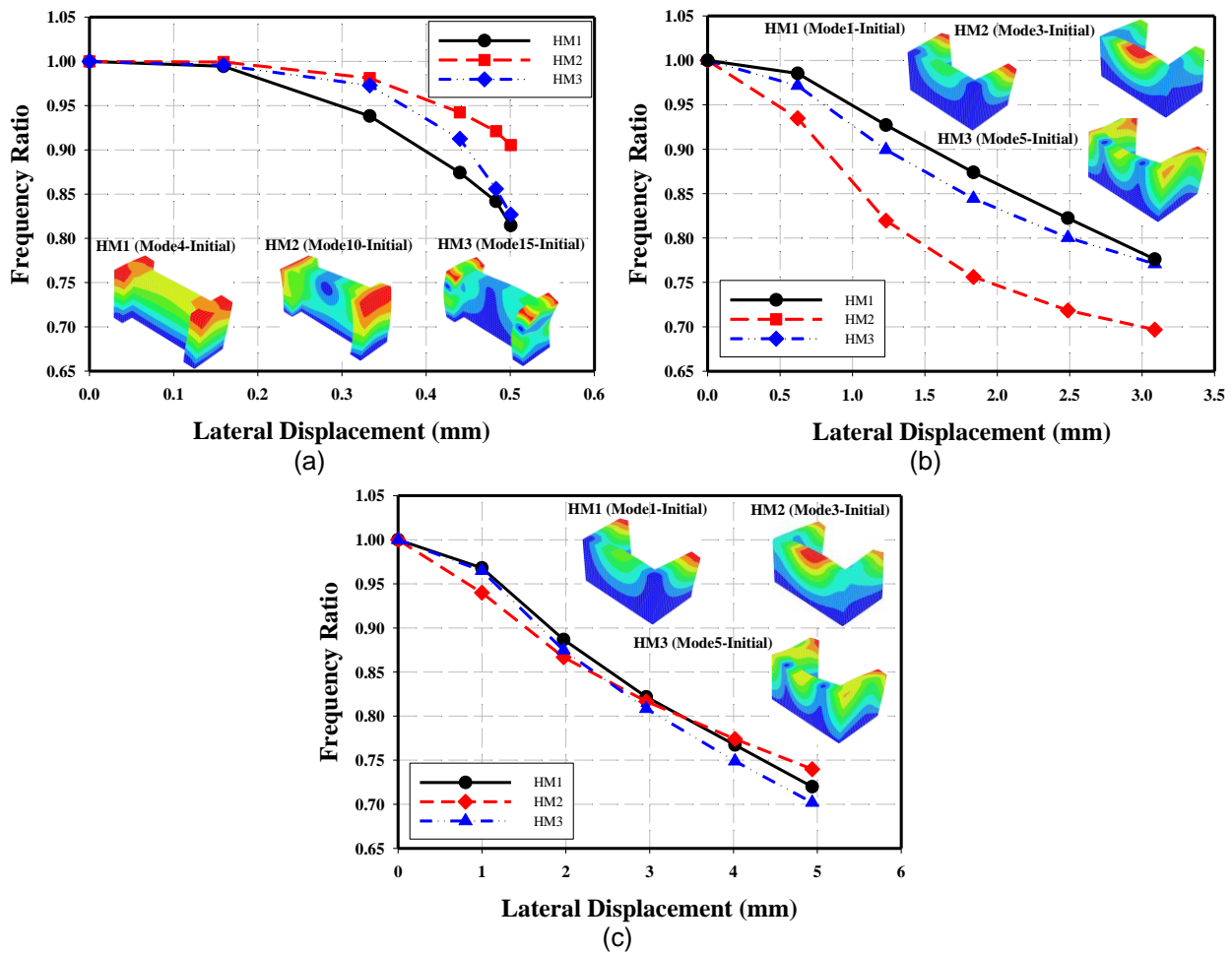


Figure 69 – Reduction in frequencies of the unstrengthened models during the pushover analyses: (a) in-plane model with 50 cm wing (b) out-of-plane model pushed in the negative direction (c) out-of-plane model pushed in the positive direction

The evolution of the effective modal mass of the aforementioned considered modes (HM) can also clarify the damage state of the models during the pushover analyses. In this regard, the effective modal mass on each step is normalized to the corresponding value at initial undamaged state and presented in Figure 70. Clearly, it is shown that the modal mass participation of HM1 in the in-plane model is relatively stable during the analysis, while the contribution of HM2 increases and that of HM3 decreases. In the case of the out-of-plane models, the contribution of HM1 drastically increases, while HM2 as the mode with the highest initial contribution significantly decreases its contribution.

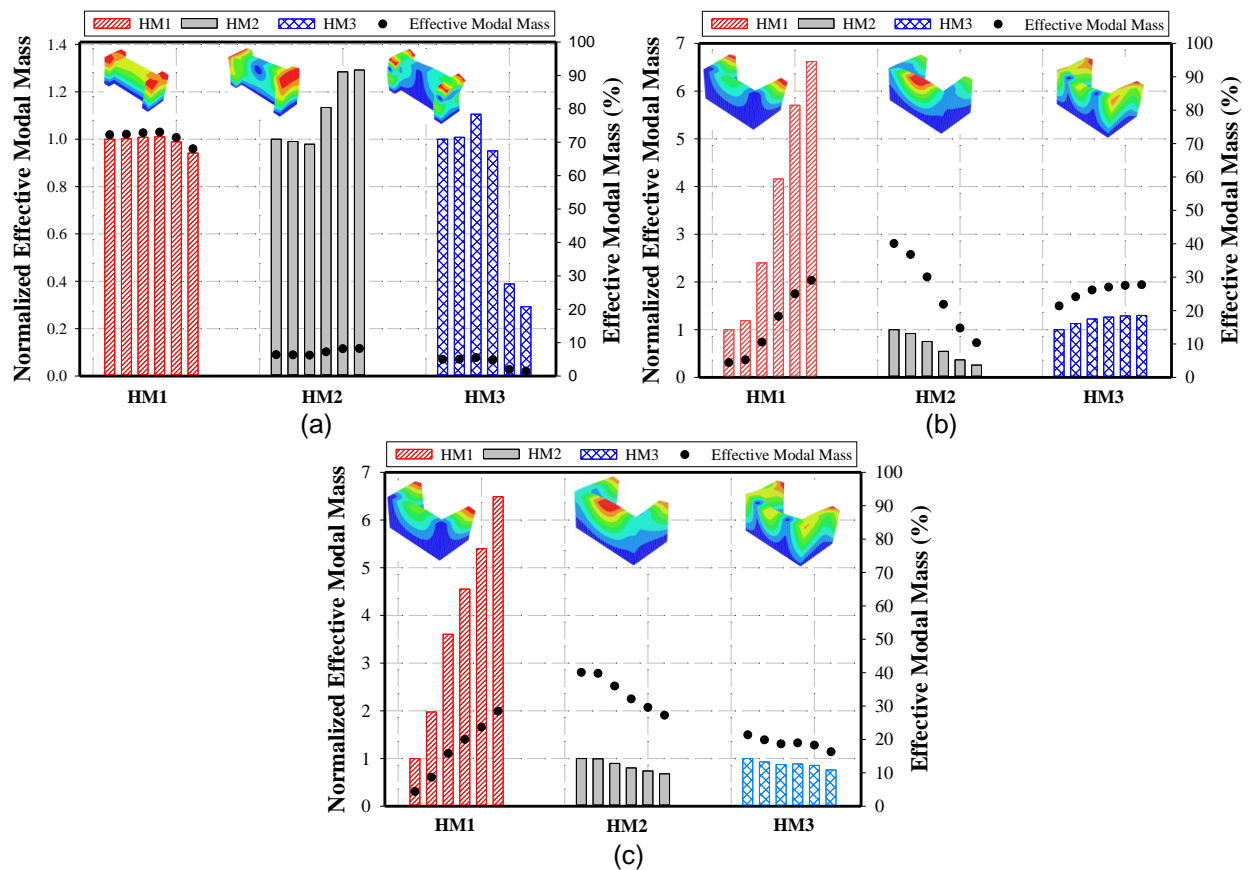


Figure 70 – Changes in the effective modal masses of the unstrengthened models during the pushover analyses: (a) in-plane model with 50 cm wing (b) out-of-plane model pushed in the negative direction (c) out-of-plane model pushed in the positive direction

### 3.10. Concluding remarks

The main remarks of Chapter 3 can be summarized as follows:

- The comparison between the FE models prepared with shell and solid elements revealed that the models with shell elements present larger displacements and in most of cases less capacity. Furthermore, different failure mechanisms were captured by the two approaches.
- It was observed that adopting large wings in the in-plane models changes the failure mode from diagonal shear cracking to detachment of the wing from the web wall. In this regard, the model with the smallest wing (i.e. 50 cm length) was selected for further numerical investigation.
- The in-plane models with 50 cm wing length presented higher capacity and ductility than those with 80 cm long. Moreover, increasing the wings' length leads to earlier initiation of damage.



- Different failure modes were observed to occur for the out-of-plane models pushed toward the wings (positive Y-direction) or outside the wings (negative Y-direction). In the latter case, the failure mechanism includes bending of the upper portion of the web and detachment of the web from wings; while in the case of the models pushed in the positive Y-direction, the wings serve as supports of the web and the failure mechanism consists of the bending of the middle part of the web.
- In the case of the out-of-plane model pushed in the negative Y-direction, the damage initiates much earlier than when it is pushed in the positive Y-direction. The latter case leads to higher capacity and ductility, while the former leads to a brittle failure.
- The investigating of the reductions in frequencies during the pushover analyses (i.e. at different damage states) shows that the modes with the highest effective mass contribution may change with different states. This behavior is particularly evident in the case of the out-of-plane model. For instance, the importance of the first high contributing mode increased during the pushover analysis, while that of the second high mode has significantly decreased.
- Reductions in frequency as indicators of damage initiation and development showed that apparently the out-of-plane models are subjected to larger damage levels than those of the in-plane model.

## CHAPTER 4

# PUSHOVER ANALYSIS OF STRENGTHENED RAMMED EARTH WALLS

### 4.1. Introduction

This chapter discusses the influence of the strengthening with low-cost TRM when applied to the rammed earth models introduced in the previous chapter. In this regard, firstly the material properties of the adopted strengthening solution and the respective modeling approach are discussed. Secondly, pushover analyses were conducted on the strengthened models and the results are compared with those from the respective unstrengthened models. Finally, the reductions in frequencies of the strengthened models were investigated for different damage levels, achieved during the pushover analyses, also to assess the effectiveness of the adopted strengthening technique.

### 4.2. Properties of the strengthening material

Regarding the strengthening, low-cost textile reinforcement mortars (LC-TRM) were adopted in the current study. The concept of this solution consists in using compatible, affordable and readily available materials in order to generalize its use. With this respect, different meshes capable of integrating this strengthening system and available in the market were characterized in Oliveira *et al.* (2017). Among them, glass fiber (denoted as G2) and nylon (called as G8) meshes were pre-selected in this study to integrate the solution to be studied in the numerical modeling of the strengthened rammed earth models. In the aforementioned experimental study, steel plates were glued to the two

ends of specimens with 100 mm width and 400 mm length. Then, displacement-controlled direct uniaxial tests were conducted on both principal directions (hereafter denoted as X and Y directions). The obtained load-strain curves are shown in Figure 71. It can be concluded from the illustrated load-strain curves that the G2 mesh has linear behavior up to the ultimate strength and a fragile post-peak behavior; whereas the G8 has much less strength with a clear hardening region, which ends with a brittle failure. It should be noted that both meshes exhibit different behaviors in X and Y directions. The obtained mechanical properties are presented in Table 15.

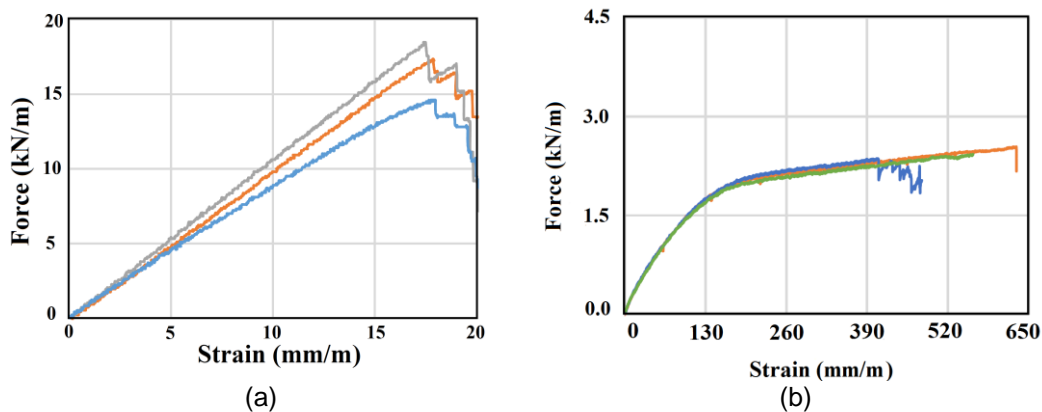


Figure 71 – Load-strain curves of low-cost textiles obtained from direct tensile tests: (a) glass fiber mesh G2 (b) nylon mesh G8 (Barroso, 2017)

Table 15 – Mechanical properties of the adopted strengthening textiles (Oliveira *et al.*, 2017 and Barroso, 2017)

Material	Mesh Aperture (mm)	Grammage (gr/m/m)	$E$ (kN/m)	Tensile strength (kN/m)	Peak strain (mm/m)	Ultimate strain (mm/m)
Glass fiber (G2)	8 x 9	$g_x = 52.3$ $g_y = 53.0$	$E_x = 979.6$ $E_y = 705$	$T_x = 16.8$ $T_y = 12.4$	$\epsilon_x = 18$ $\epsilon_y = 15$	$\epsilon_{ux} \geq 20$ $\epsilon_{uy} \geq 22$
Nylon (G8)	16 x 21	$g_x = 36.4$ $g_y = 54.6$	$E_x = 136.1$ $E_y = 181.5$	$T_x = 2.4$ $T_y = 4.3$	$\epsilon_x = 532$ $\epsilon_y = 505$	$\epsilon_{ux} \geq 600$ $\epsilon_{uy} \geq 540$

In the FE modeling, the stress-strain curves of each material are required, while the mechanical behavior reported for the meshes relates the linear force with the strain. Therefore, it was decided to adopt the tensile behavior of TRM specimens, which considers both the mortar and the mesh together as a composite material. It should be noted that this does not allow simulating the slippage of the fibers within the matrix. These results are obtained from uniaxial tensile tests on specimens consisting of mortar layers reinforced with textile meshes, as illustrated in Figure 72.

The obtained composite tensile stress-strain curves are presented in Figure 73. The experimental results corresponding to these curves were originally reported in terms of linear tensile force-strains relations, which were transformed into the stress-strain relations by considering a 10 mm uniform thickness for the TRM composite (mortar and embedded mesh).

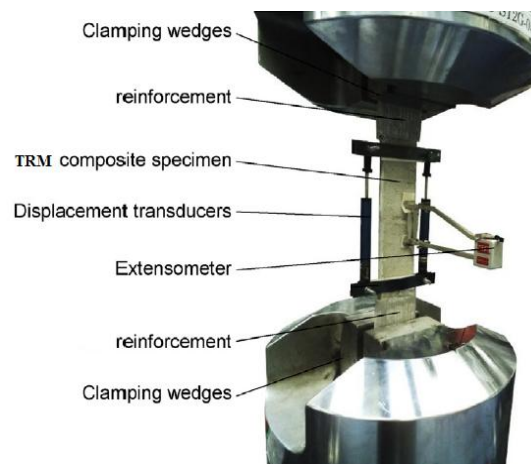


Figure 72 – Setup for the uniaxial tensile tests on composite mortar-mesh specimens (Ascione *et al.*, 2015)

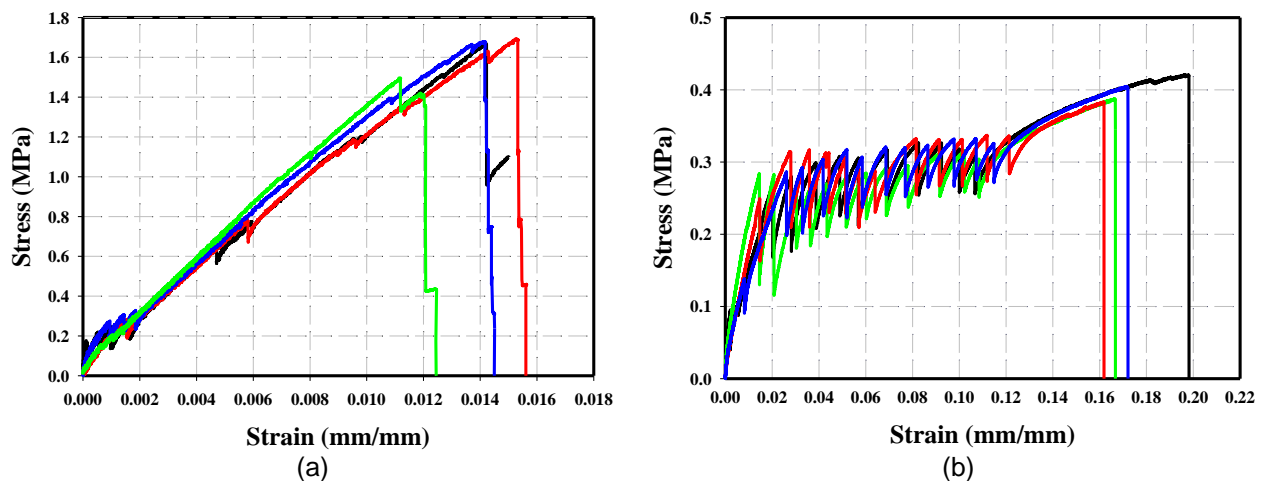


Figure 73 - Uniaxial tensile stress-strain curves of composite LC-TRM band specimens (Barroso, 2017): (a) G2 mesh (b) G8 mesh

Regarding the numerical modeling of the stress-strain curves, a trilinear average stress-strain curve was adopted to represent the behavior of each TRM. The first stage mostly represents the contribution of the uncracked mortar, while in the second stage the mortar is cracked but still contributes for the composite behavior together with the mesh. The third stage is governed by the behavior of the mesh. As it can be seen from the experimental curves (Figure 73), a brittle failure is expected for both meshes immediately after the peak load. The adopted trilinear numerical curves (average curves) are presented in Figure 74 in comparison to the experimental ones.

Furthermore, the definition of the full behavior of the TRM system requires defining its behavior under compression. In this regard, the contribution of the mesh was disregarded and the behavior was assumed as being that of the mortar. An experimental study was conducted and presented in Oliveira *et al.* (2017), where the mechanical behavior of mortars with different compositions was characterized by means of compression tests on cylindrical specimens.

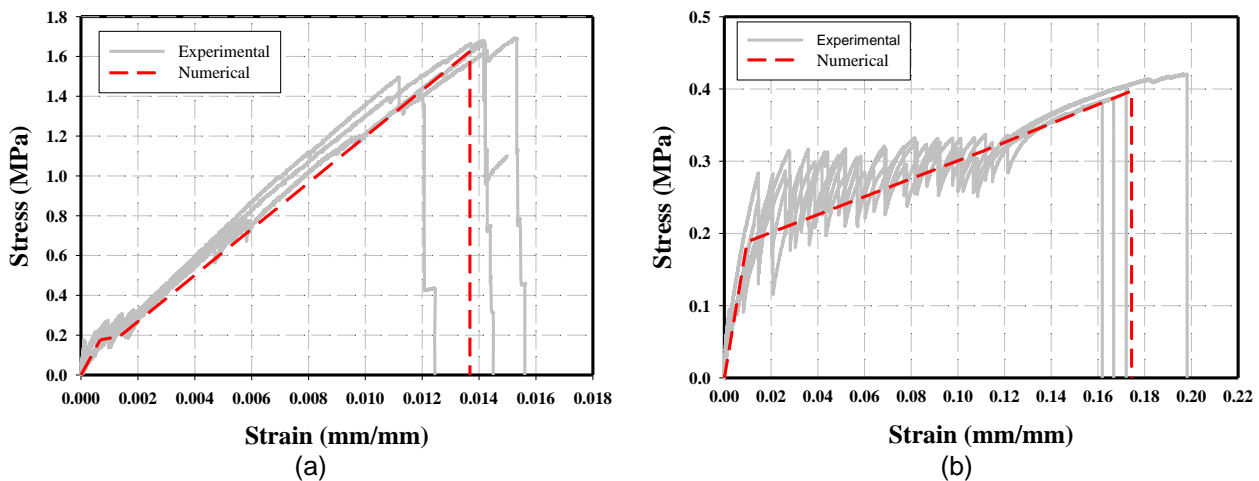


Figure 74 – Trilinear numerical curves based on the experimental tensile stress-strain curves of TRM composite specimens: (a) G2 mesh (b) G8 mesh

From the tested mortars, that with 33% (weight percentage) of earth, 67% of sand and a water to solids (W/S) ratio of 0.17 showed good performance, and thus it was selected for this numerical investigation. The aforementioned reference study denoted this mortar as EM2 and its mechanical properties are reported in Table 16. It is worthwhile to note that different loading states (i.e. in the ranges of 10-25%, 25-50%, and 10-50% of the peak strength) were considered in the estimation of the Young's modulus. In the following, and as it is shown in Figure 75b, the value corresponding to 10-25% of strength i.e.  $3431 \text{ N/mm}^2$  has better agreement with experimental results.

Table 16 – Mechanical properties of the mortar selected to integrate the numerical modeling (Oliveira *et al.*, 2017 and Barroso, 2017)

Material	$\rho$ ( $\text{kg/m}^3$ )	$E$ ( $\text{N/mm}^2$ )	$f_c$ (MPa)	$f_t$ (MPa)	$\varepsilon_{tu}$ (mm/mm)
EM2 Mortar	1810	3431 (10-25% stress) 2150 (25-50% stress) 2506 (10-50% stress)	1.30	0.51	0.00015

The reported compressive stress-strain curves of the cylindrical specimens and their average curve are shown in Figure 75a. This average curve was then smoothed to represent numerically the compressive behavior of the mortar. Also, a trend based descending branch was added to the post-peak part of the behavior (see Figure 75b) to take into account the stress degradation of the TRM composite in compression.

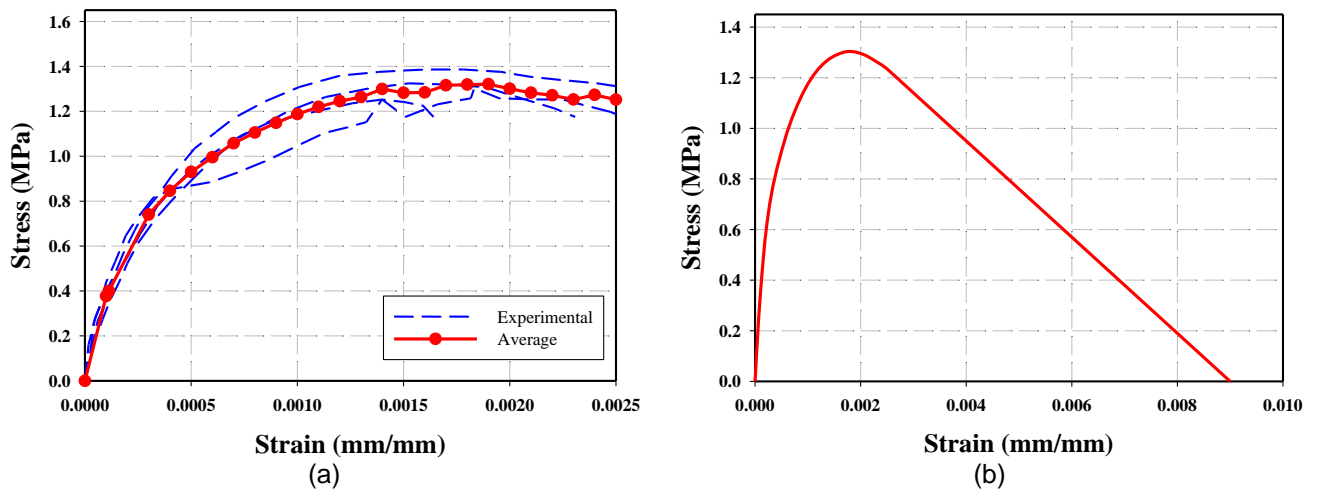


Figure 75- Adopted compressive stress-strain curve of the TRM composite: (a) average experimental behavior (b) numerical compressive behavior with descending post peak branch

By comparing the different available compressive material behaviors implemented in DIANA FEA, it seems that the multi-linear behavior is the most appropriate. For instance, the conventional parabolic relationship was verified. This relationship is widely used to represent the compressive behavior of concrete and masonry materials (see Figure 76a). In this regard, the fracture energy to the element size ratio was calculated using the stress-strain curve shown in Figure 75b and adopting equation (9); which was estimated to be equal as  $0.00041 \text{ N/mm}^2$ .

$$\int_{\alpha_c}^{\alpha_u} f \, d\alpha_j = \frac{G_c}{h} \quad (9)$$

Where  $G_c$  is the fracture energy and  $h$  is the characteristic element length. Other parameters are defined in Figure 76a.

The resulted stress-strain curve obtained for the parabolic relationship is compared with the experimental one in Figure 76b. The parabolic curve is obtained by using implemented formulation in DIANA FEA and reported mechanical properties of the mortar. As it can be observed, the parabolic relation leads to a considerably different behavior.

Finally, the adopted complete composite stress-strain behavior adopted here is presented in Figure 77. Since the compressive behavior is due to the contribution of the mortar, it becomes identical in both mesh cases. The LC-TRM composite with mesh G2 has the greatest tensile strength (ratio of about 4.1), while that with mesh G8 has the greatest deformability in tension (ratio of about 12.7).

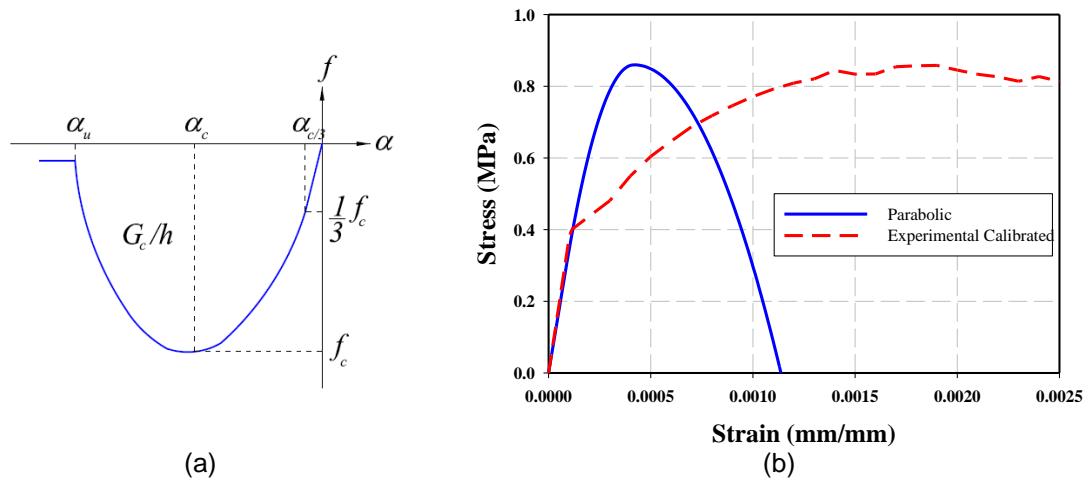


Figure 76 – Applicability of the conventional parabolic compressive behavior in the modeling of the mortar: (a) adopted parabolic compressive behavior in DIANA FEA software (b) comparison between the numerical parabolic behavior and the experimental behavior of the mortar

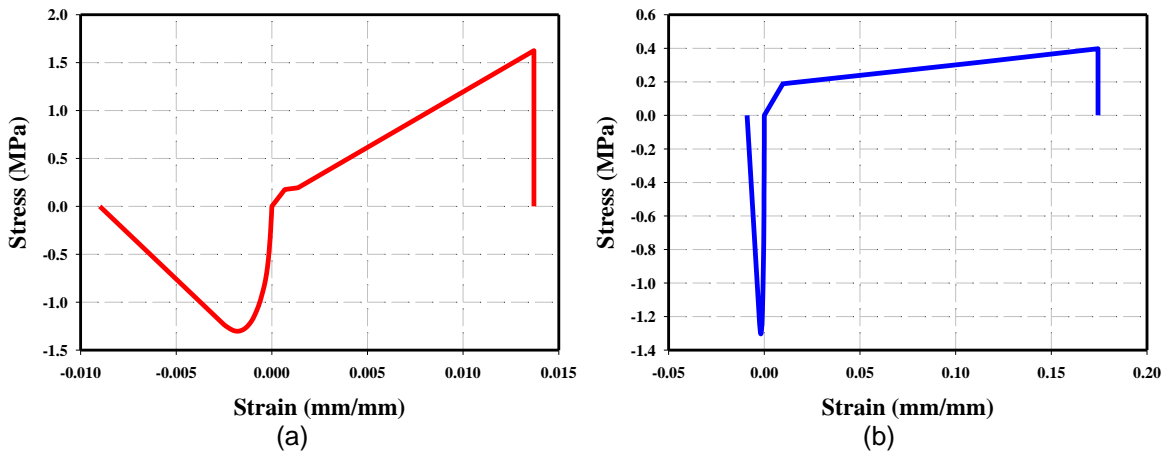


Figure 77 – Adopted stress-strain composite behavior for the LC-TRM: (a) mesh G2 (b) mesh G8

### 4.3. Finite element modelling of the strengthening

The modeling approaches adopted in the preparation of the FE models was previously discussed in Section 3.4; thus the current section only includes the aspects related with modeling of the LC-TRM strengthening.

In order to model the strengthening, shell elements were used and were connected to the model of the wall by means of interface elements. The employed shell elements consisted of 8 node quadrilateral curved shell elements CQ40S, as detailed in Section 3.4. Therefore, a quadrilateral interface element was used to connect the rammed earth solid elements with the LC-TRM shell elements (see Figure 78). The meshing size in the strengthened model was similar to that of unstrengthened models. The interfaces were assumed as rigid in order to avoid any relative displacement between the substrate and strengthening.

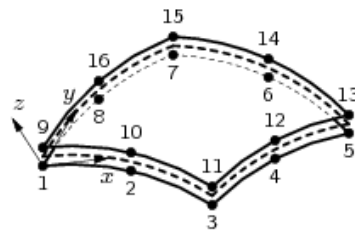


Figure 78 - Interface element employed in the preparation of the strengthened models (DIANA FEA BV, 2017)

#### 4.4. Strengthening selection

The current costs of the meshes G2 and G8 are estimated to be of about  $0.85 \text{ €/m}^2$  and  $0.63 \text{ €/m}^2$ , respectively (Barroso, 2017). Nevertheless, both cases seem to correspond to residual costs in the overall implementation of the strengthening solution. Therefore, the rational selection between these two meshes points to that providing the best expected performance from the structural point of view. In this regard, both meshes were tested in the in-plane model to assess their strengthening effectiveness by means of pushover analysis (see Figure 79). With respect to the analysis results, it should be noted that choosing the node on top of the right wing from the web in the unstrengthened model (local failure mode) originated a large deformation capacity, which may constitute a case of false ductility of the model. Nevertheless, it gives a clear sense about the stability enhancement achieved by any of the adopted strengthening materials. In this regard, the control node at the middle section of the web was also taken into account (see Figure 79a). As it can be seen, the strengthening with the G8 LC-TRM results in a 13% and 8% increase in displacement and load capacities, respectively; while in the G2 composite the increase is of 56% and 21%, respectively. In conclusion, using the G2 LC-TRM composite seems more reasonable, whereby the subsequent investigation was conducted using this particular solution.

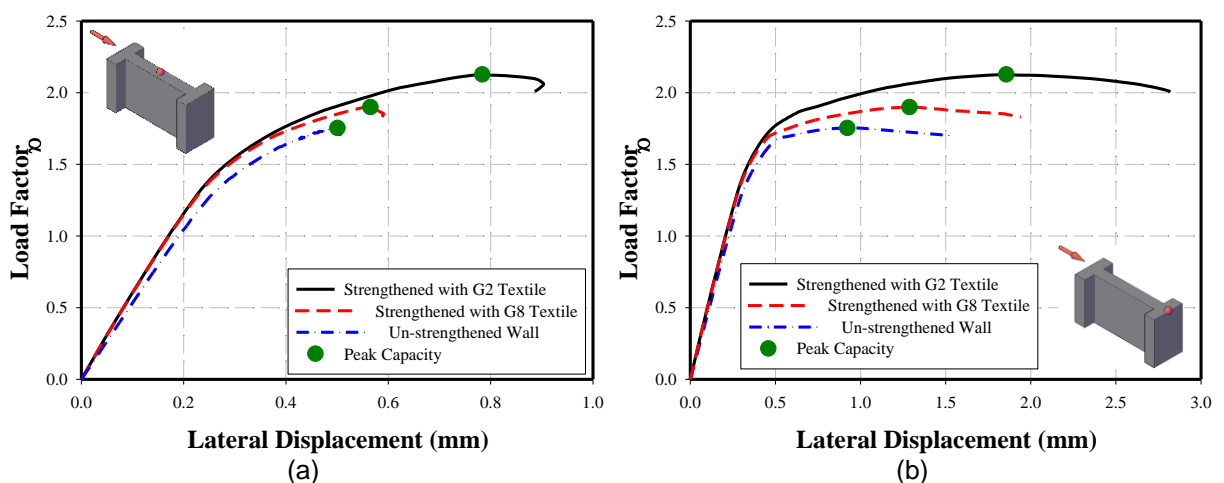


Figure 79 – Comparison between the different LC-TRM strengthening solutions on the seismic response of the in-plane model: (a) control node at the middle section of the web (b) control node at top of the right wing



## 4.5. Modal analyses

The implemented strengthening solution did not significantly increase the mass of the models, while a slight stiffness increment was expected. Therefore, the mode shapes, frequencies, and modal mass participations are expected to change slightly. The modes with the highest effective mass contribution are presented in Table 17 and Table 18, respectively for the strengthened in-plane and out-of-plane models. By comparing the dynamic properties of the strengthened models with corresponding values of the unstrengthened models, it is possible to observe that periods decreased. Moreover, a slight increase on the cumulative effective modal mass was observed. This increment can be due to an improved integrity of the model provided by the adopted strengthening. In other words, some local modes may have been mitigated in the strengthened model.

Table 17 – Dynamic properties of the strengthened in-plane model

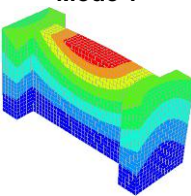
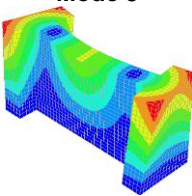
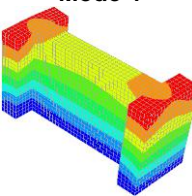
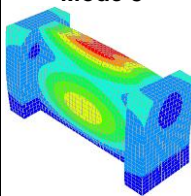
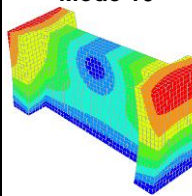
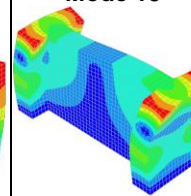
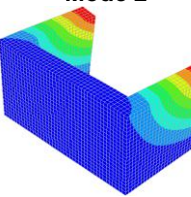
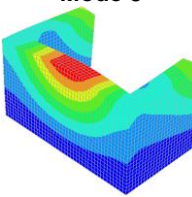
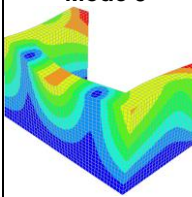
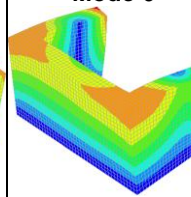
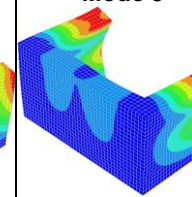
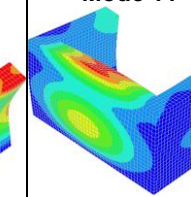
Mode 1	Mode 3	Mode 4	Mode 8	Mode 10	Mode 15
					
$T_1 = 0.0452 \text{ sec}$ EMM <sub>x</sub> = 0.0% CEM <sub>x</sub> = 0.0% EMM <sub>y</sub> = 57.49% CEM <sub>y</sub> = 57.49%	$T_4 = 0.0273 \text{ sec}$ EMM <sub>x</sub> = 0.0% CEM <sub>x</sub> = 0.0% EMM <sub>y</sub> = 5.57% CEM <sub>y</sub> = 63.06%	$T_8 = 0.0248 \text{ sec}$ EMM <sub>x</sub> = 72.32% CEM <sub>x</sub> = 72.32% EMM <sub>y</sub> = 0.0% CEM <sub>y</sub> = 63.06%	$T_{10} = 0.0125 \text{ sec}$ EMM <sub>x</sub> = 0.0% CEM <sub>x</sub> = 72.32% EMM <sub>y</sub> = 16.18% CEM <sub>y</sub> = 79.27%	$T_{10} = 0.0112 \text{ sec}$ EMM <sub>x</sub> = 5.97% CEM <sub>x</sub> = 78.28% EMM <sub>y</sub> = 0.0% CEM <sub>y</sub> = 79.27%	$T_{15} = 0.0094 \text{ sec}$ EMM <sub>x</sub> = 5.77% CEM <sub>x</sub> = 84.05% EMM <sub>y</sub> = 0.0% CEM <sub>y</sub> = 84.59%

Table 18 – Dynamic properties of the strengthened out-of-plane model

Mode 2	Mode 3	Mode 5	Mode 6	Mode 9	Mode 11
					
$T_2 = 0.0459 \text{ sec}$ EMM <sub>x</sub> = 33.86 % CEM <sub>x</sub> = 33.86 % EMM <sub>y</sub> = 0.0 % CEM <sub>y</sub> = 4.5 %	$T_3 = 0.0355 \text{ sec}$ EMM <sub>x</sub> = 0.0 % CEM <sub>x</sub> = 33.86 % EMM <sub>y</sub> = 43.19 % CEM <sub>y</sub> = 47.70 %	$T_5 = 0.0224 \text{ sec}$ EMM <sub>x</sub> = 0.0 % CEM <sub>x</sub> = 37.52 % EMM <sub>y</sub> = 18.56 % CEM <sub>y</sub> = 66.26 %	$T_6 = 0.0218 \text{ sec}$ EMM <sub>x</sub> = 29.48 % CEM <sub>x</sub> = 66.99 % EMM <sub>y</sub> = 0.0 % CEM <sub>y</sub> = 66.26 %	$T_9 = 0.0132 \text{ sec}$ EMM <sub>x</sub> = 8.94 % CEM <sub>x</sub> = 78.81 % EMM <sub>y</sub> = 0.0 % CEM <sub>y</sub> = 67.11 %	$T_{11} = 0.0124 \text{ sec}$ EMM <sub>x</sub> = 0.0 % CEM <sub>x</sub> = 78.81 % EMM <sub>y</sub> = 9.10 % CEM <sub>y</sub> = 76.92 %

## 4.6. Pushover analyses

In this section, the effectiveness of the adopted strengthening solution was assessed by means of pushover analyses. This purpose was achieved by following a similar approach to that used for the

unstrengthened models. Nevertheless, this is only performed for the solid in-plane model with 50 cm wing and the solid out-of-plane model, as discussed in Section 3.8.

#### 4.6.1. In-plane model

The pushover curve of the strengthened in-plane model is compared with the unstrengthened one in Figure 80. Three control nodes were taken into account, namely on the right and left wings, and on middle section of the web. As previously stated, the lateral stiffness of the wall is slightly increased. As it can be seen, in spite of considerable enhancement in displacement and load capacities of the strengthened model, the right wing still sways. In other words, the possible failure mechanism was not changed from the unstrengthened model to the strengthened one.

Due to the possible detachment of the right wing from the web, the control node on the middle section of the web was considered to evaluate the influence of the adopted strengthening technique. With respect to this control node, a 56.5% and 21.3% increases in the lateral displacement and load capacities were observed, respectively.

In addition to the capacity, the damage initiation point is also highlighted in Figure 80. No marked difference was detected between this point in the strengthened model with that of the unstrengthened one. As previously discussed in chapter 3, a very local damage occurs at this point. In conclusion, the onset of the damage in the strengthened model is identical to that of the unstrengthened model, whereas their development was different, as it is following discussed.

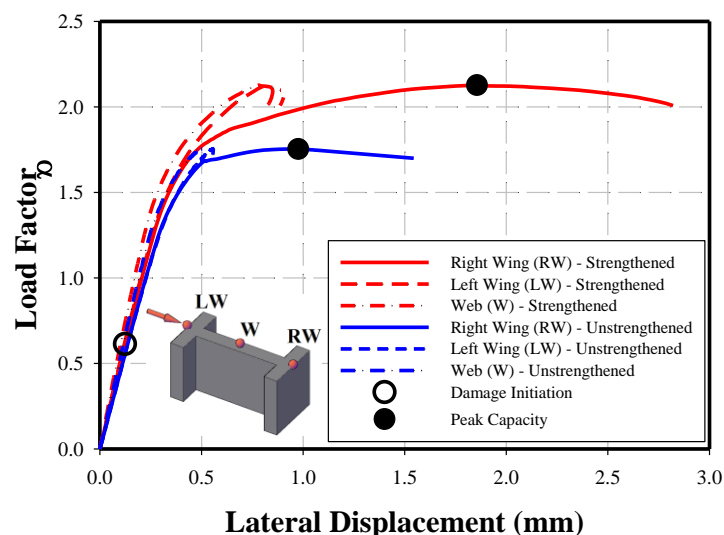


Figure 80 - Pushover curves of the strengthened in-plane model in comparison of those of the unstrengthened one

The contour of the displacements in the in-plane direction was investigated to understand the possible failure mechanism of the strengthened model (see Figure 81). By comparing the experienced lateral displacements of the unstrengthened and strengthened models at the load factor equal to the peak

capacity of the unstrengthened model, it is observed that the strengthened model presents lower deformations, due to the increase in the lateral stiffness and a probable better redistribution capacity.

On the other hand, the contour of the strengthened model at its peak capacity shows important deformations at the right wing and in the region of its connection with the web (see Figure 81c). Therefore, it can be concluded that the failure mechanism of the strengthened model also includes the detachment of the right wing. Furthermore, the adopted strengthening LC-TRM strengthening solution is shown to be efficient on postponing this failure mode.

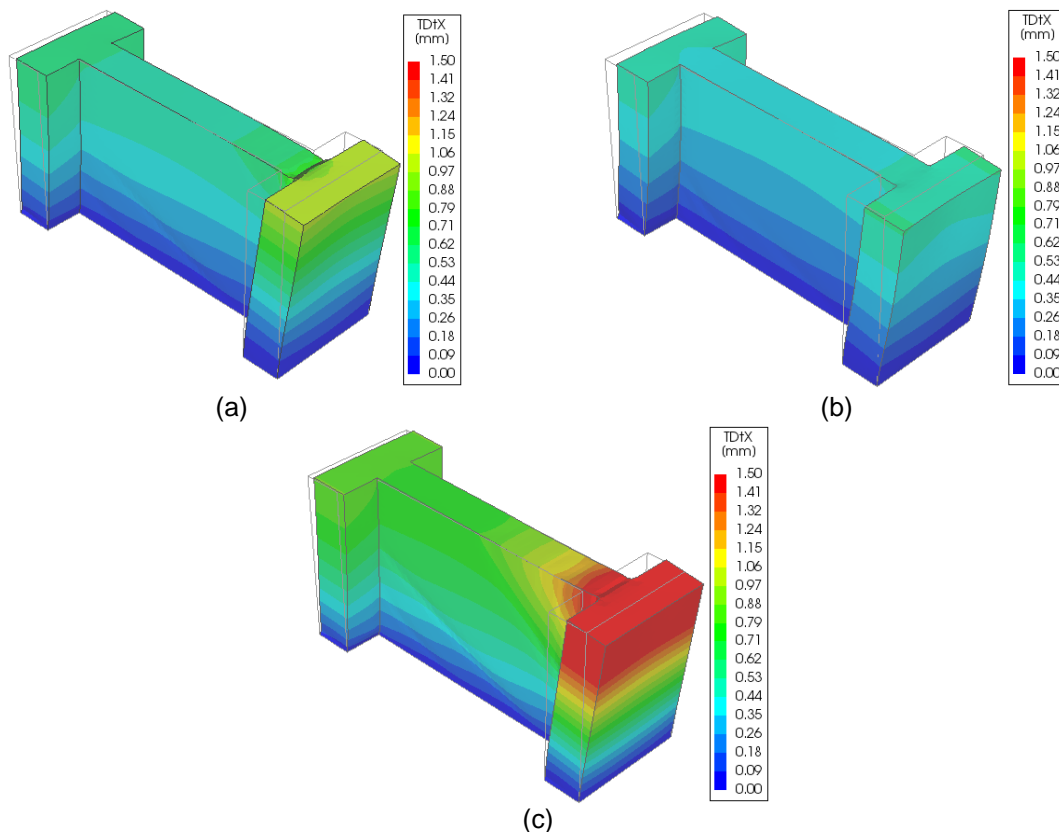


Figure 81 – Lateral displacements of the in-plane models: (a) unstrengthened model at its peak capacity (b) strengthened model at the peak capacity of the unstrengthened model (c) strengthened model at its peak capacity

Moreover, the applied strengthening solution was expected to increase the integrity of the wall, by promoting the redistribution stresses and decreasing stress concentrations in the most vulnerable regions. The contours of the principal compressive stresses for both reinforced and unreinforced models are compared in Figure 82.

A diagonal strut was observed to form at the web of the unstrengthened model at its peak capacity, while this did not occur in the strengthened model at this point. This situation is due to the increased capacity promoted by the application of the LC-TRM composite and by its contribution in transferring the tensile stresses. Furthermore, the reduction in compression stresses of the right wing's toe shows

less detachment between the right wing and the web. Since by preserving the integrity of the wall, its overturning along the toe is reduced, which consequently leads to smaller compressive stresses.

The principal compressive stresses at the peak capacity of the strengthened model show a larger diagonal strut in comparison to the peak capacity of the unstrengthened model, meaning that the strengthening allows further exploring the shear capacity of the web.

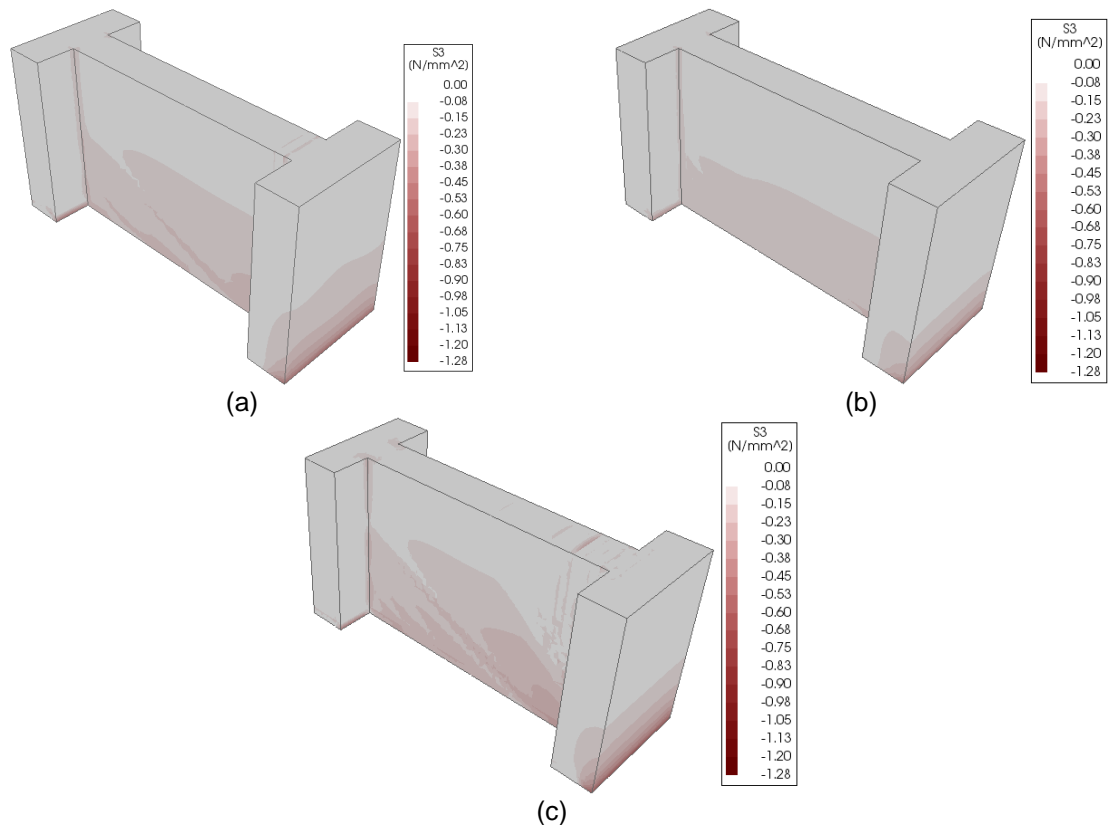


Figure 82 - Principal compressive stresses of the in-plane models: (a) unstrengthened model at its peak capacity (b) strengthened model at the peak capacity of the unstrengthened model (c) strengthened model at its peak capacity

Similar conclusions can be derived from investigating the principal tensile strains of the models (see Figure 83). An apparent improvement in the seismic response is clearly observed from comparison of the principal tensile strains of both strengthened and unstrengthened models at the peak capacity of the unstrengthened wall. At this stage, the detachment between the right wing and the web is completely prevented. This is also true for the developed diagonal shear crack on the web. Only some damage in the toe of the left wing was observed, evidencing the tendency of the wall to overturn. It can also be seen that the strengthened model experiences smaller strains in this region in comparison with the unstrengthened model. This situation can be explained by the improved integrity of the wall due to the application of the strengthening.

The principal tensile strains at the peak capacity of the strengthened model show an important detachment of the right wing, however, a portion of the web follows the wing. From the kinematic point

of the view, this added portion means that a greater load is required to cause the right wing to detach from the wall and overturn. Moreover, a diagonal shear crack was observed in the web, whose development is much more expensive than that evidenced in unstrengthened one. This developed diagonal shear crack illustrates the efficiency of the adopted strengthening solution in improving and exploring the in-plane seismic behavior of rammed earth walls.

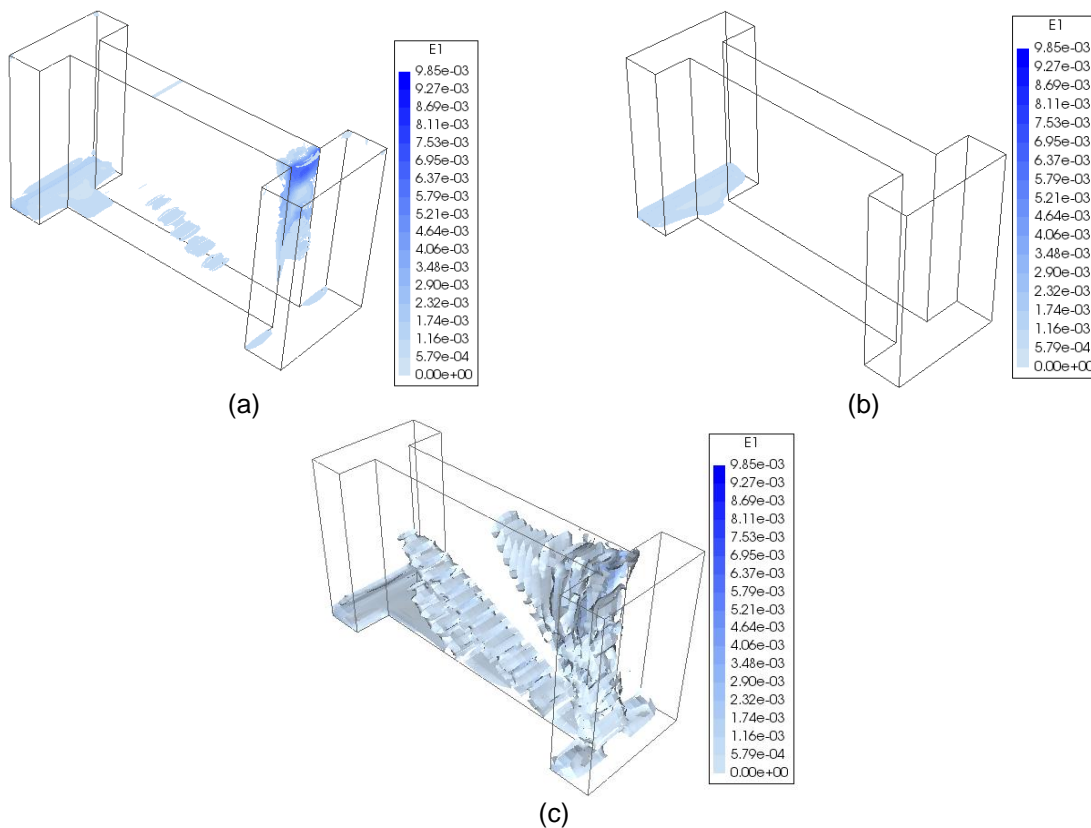


Figure 83 - Principal tensile strains of the in-plane models: (a) unstrengthened model at its peak capacity (b) strengthened model at the peak capacity of the unstrengthened model (c) strengthened model at its peak capacity

Finally, it is also important to investigate the damage state of the applied strengthening. In this regard, the contour of the principal compressive stresses and principal tensile strains at the peak capacity of the strengthened model is presented in Figure 84. As it can be seen, the applied LC-TRM composite significantly contributes to the stress transferring (see Figure 84a). This contribution is apparent on the web and toes of the wings, where the model is likely to overturn. On the other hand, the contour of the principal tensile strains clearly shows the working mode of the strengthening solution. In other words, the efficient strengthening technique should mostly work in regions likely to fail without reinforcement. As previously discussed, these regions for the in-plane model are the connection of the right wing with the web and the diagonal of the web. As it is evident, considerable tensile strains were developed in the strengthening adjacent to the right wing, which postpones its detachment.

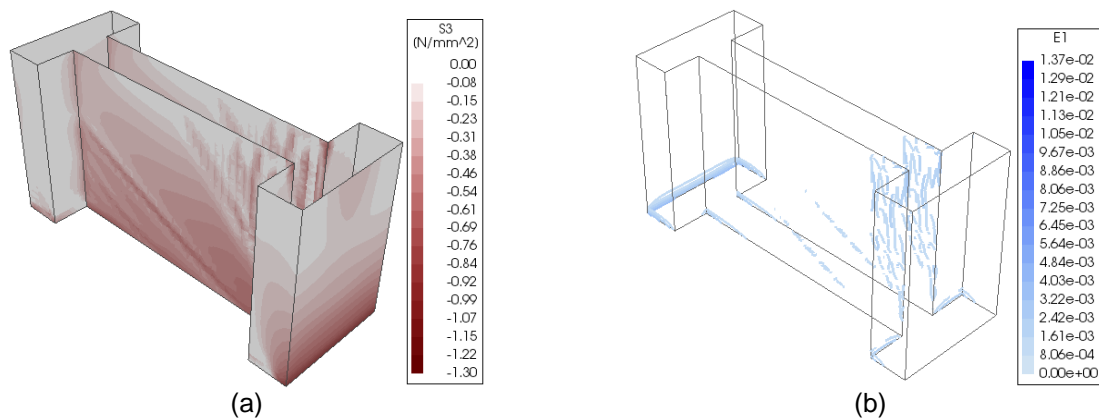


Figure 84 – Damage of the LC-TRM composite in the in-plane strengthened model at its peak capacity: (a) principal compressive stress (b) principal tensile strain

#### 4.6.2. Out-of-plane model

In this section, the influence of LC-TRM strengthening in the out-of-plane model was investigated. Due to the asymmetric geometry of the model, the results are presented for the cases where the model is pushed in the negative and positive directions.

The pushover curve of the strengthened out-of-plane model pushed in the negative Y-direction in comparison with the unstrengthened model is presented in Figure 85. As it can be seen, the strengthening increases the pre-peak stiffness of the model by controlling the cracking process. Moreover, the lateral displacement and the load capacities were increased by 45.1% and 28.5%, respectively. As discussed in the previous section, the applied strengthening solution has no influence on the onset of damage. Furthermore, the strengthened model presents smoother post-peak behavior when compared against the unstrengthened one.

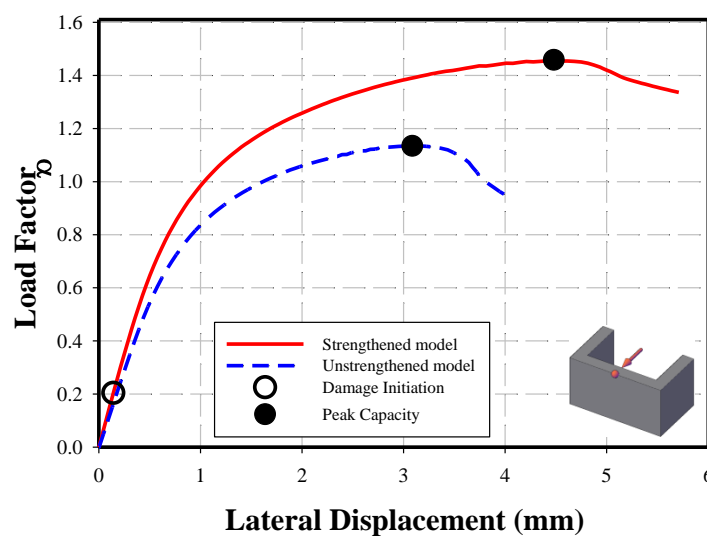


Figure 85 - Pushover curve of the strengthened out-of-plane model pushed in the negative direction in comparison of the unstrengthened one

The contours of the lateral displacements of both strengthened and unstrengthened out-of-plane models pushed in the negative direction are presented in Figure 100. By comparing the experienced lateral displacements of the strengthened model with that of the unstrengthened one, at the peak capacity of the unstrengthened model, it is possible to observe a significant reduction especially in the middle section of the web. This was expected due to previously mentioned increase in the lateral stiffness of the wall. On the other hand, the contour of the strengthened model at its peak capacity exhibits considerable improvements with respect to the unstrengthened case. For instance, the section of the strengthened web deformed by the lateral loading is larger than in the case of the unstrengthened model. Furthermore, a higher contribution of the wing walls was observed in the strengthened case.

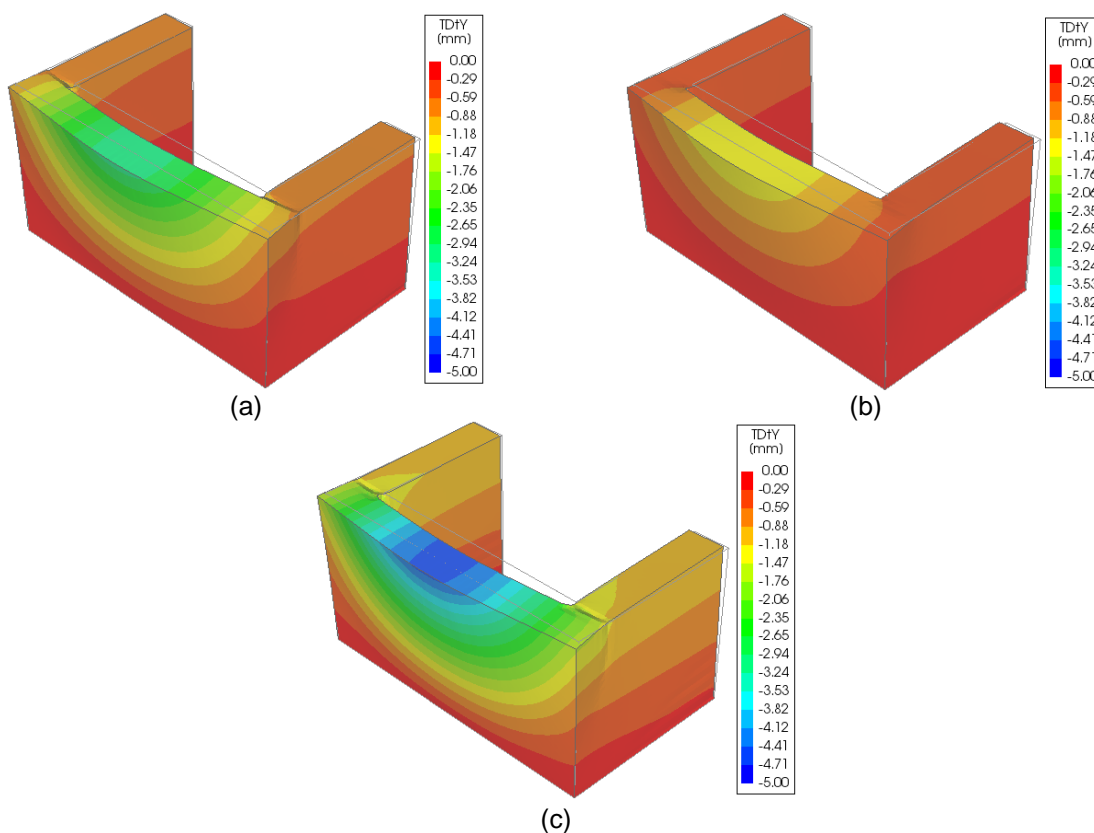


Figure 86 - Lateral displacements of the out-of-plane models pushed in the negative direction: (a) unstrengthened model at its peak capacity (b) strengthened model at the peak capacity of the unstrengthened model (c) strengthened model at its peak capacity

The contours of the principal compressive stresses for both strengthened and unstrengthened out-of-plane models pushed in the negative direction are presented in Figure 87. As it can be observed, a diagonal compressive strut is developed in the unstrengthened model and at the load equal to its capacity. Moreover, the tendency of the web to detach from the wing walls and bend over the mid-section of itself was clear, while the mentioned compressive strut is prevented in the strengthened

model. This strut is likely to develop at the peak capacity of the strengthened model, while it seems to be less severe than in the unstrengthened model.

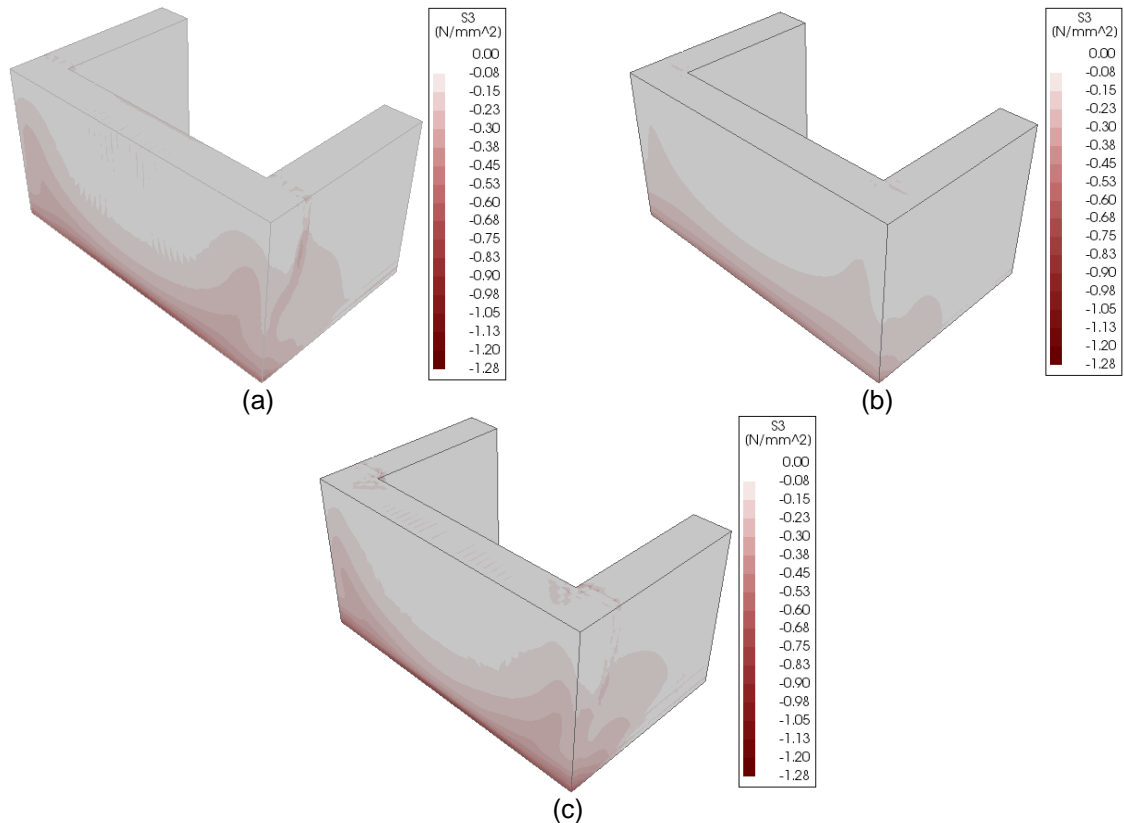


Figure 87 - Principal compressive stresses of the out-of-plane models pushed in the negative direction: (a) unstrengthened model at its peak capacity (b) strengthened model at the peak capacity of the unstrengthened model (c) strengthened model at its peak capacity

The Contours of the principal tensile strains for both strengthened and unstrengthened out-of-plane models pushed in the negative direction are presented in Figure 88. A considerable reduction in the principal tensile strains level was observed for the strengthened model at a lateral load equal to the peak capacity of the unstrengthened one. As it can be seen, the detachment of the web from the wing walls and bending of the web's mid-section were avoided. Furthermore, the tensile strains at the base of the wall were decreased. This situation can be interpreted as an improvement of the integrity and lateral stiffness of the wall due to the application of the strengthening. In other words, the employed strengthening solution enables the wall to redistribute the stresses and decreases its tendency to overturn. Additionally, the contour of the principal tensile strains at the peak capacity of the strengthened model shows that the failure mechanism is similar to that of the unstrengthened model, while a larger mid-section of the web is bending. It should be noted that this larger section means that a higher lateral load is required to initiate the collapse mechanism.



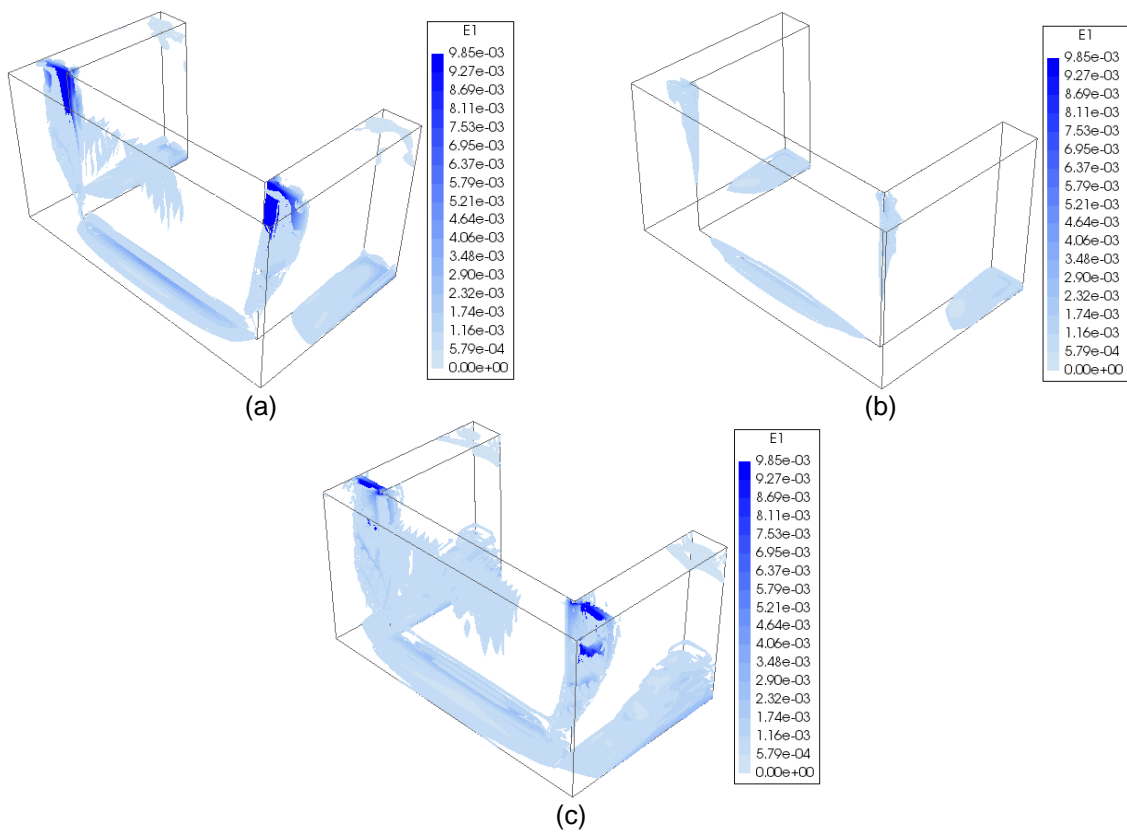


Figure 88 - Principal tensile strains of the out-of-plane models pushed in the negative direction: (a) unstrengthened model at its peak capacity (b) strengthened model at the peak capacity of the unstrengthened model (c) strengthened model at its peak capacity

In the following, the performance of the strengthening was assessed by investigating its principal compressive stresses and principal tensile strains at the peak capacity of the strengthened model. The obtained outcomes are presented in Figure 89. As it can be seen, a diagonal compressive strut was formed in the strengthening in the wing walls (see Figure 89a). This strut prevents development of the previously discussed diagonal shear crack which makes the web to detach from the wing walls. The same conclusion can be derived from the evident high tensile strains in the connections.

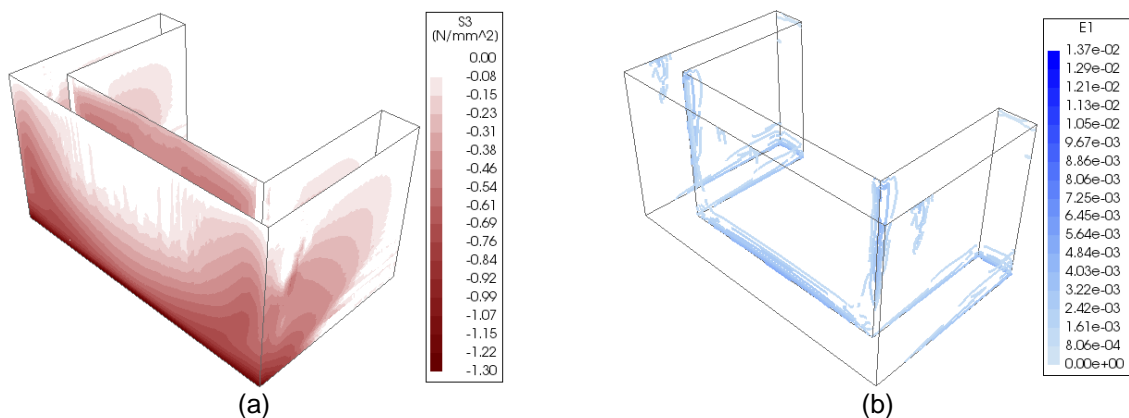


Figure 89 – Damage state of the TRM composite on the out-of-plane strengthened model pushed in the negative direction at its peak capacity: (a) principal compressive stress (b) principal tensile strain

As discussed in the previous chapter, the response of the out-of-plane model pushed in the positive direction is less important than when pushed in the negative direction. However, the pushover curve of the former is presented in Figure 90. As it can be seen, the displacement capacity is improved about 131%. In the case of the load capacity, the improvement is of about 30.5%. Similarly to all previously studied strengthened models, the lateral stiffness was increased, while damage initiation point remains basically unchanged.

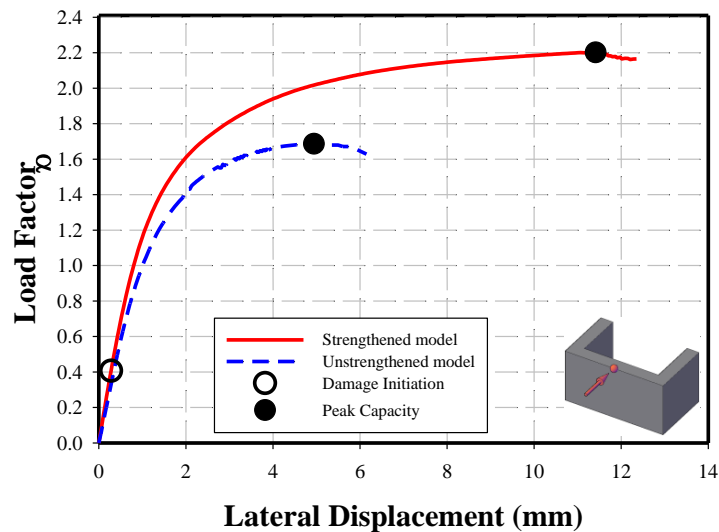


Figure 90 - Pushover curve of the strengthened out-of-plane model pushed in the positive direction in comparison of the unstrengthened one

The contour map of the lateral displacements of the strengthened model subjected to a lateral load equal to the peak capacity of the unstrengthened model shows that the failure mechanism (i.e. bending at mid-section of the web) is controlled by the strengthening. However, the state of the strengthened model at its peak capacity seems to indicate a failure somehow similar to that of the unstrengthened one, although a much larger section is bending. The latter statement requires analyzing the stress and strain fields.

The lateral loads in the web of the unstrengthened out-of-plane model pushed in the positive direction are transferred to the wing walls by the arch effect. This effect is clearly shown by the contour of the principal compressive stresses presented in Figure 92. As it is evidenced, the mentioned stresses are transferred to the base by means of compressive struts in the wing walls. It can be seen that the aforementioned arch seems less developed in the strengthened model under lateral loads equal to the peak capacity of the unstrengthened model. On the other hand, significant compressive stresses were observed at the connections of the web to the wings in the strengthened model. This behavior may be interpreted as a changing from dominant bending at the mid-section (unstrengthened model) to detachment of the web from the wings due to shear cracks (strengthened model).

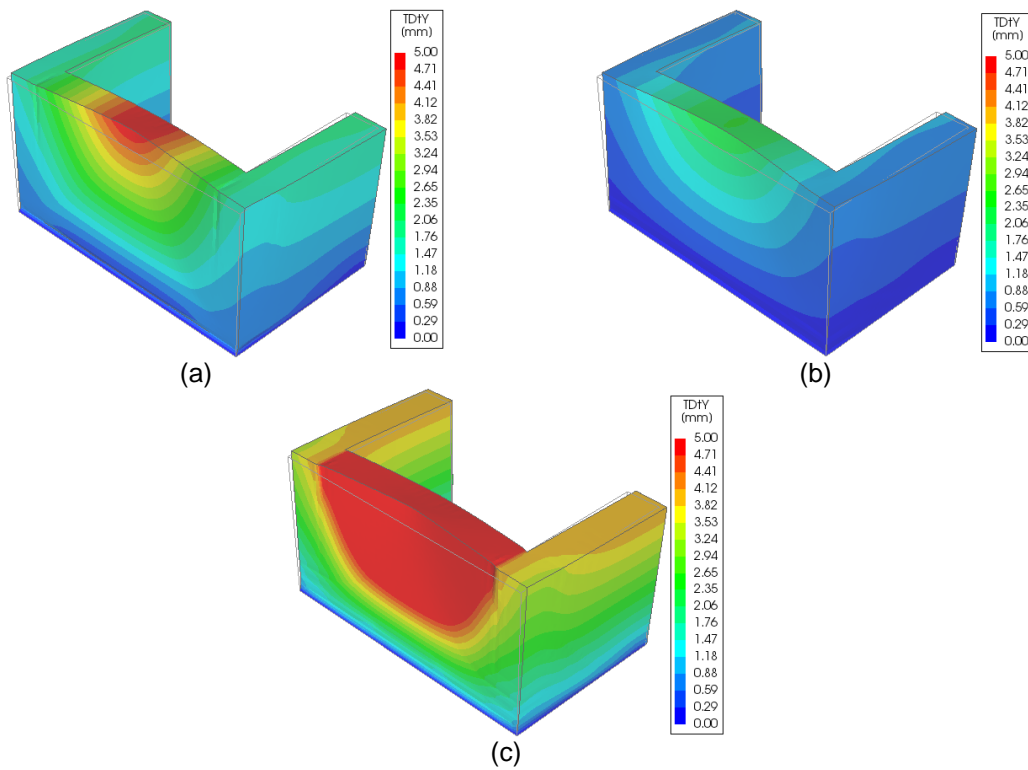


Figure 91 - Lateral displacements of the out-of-plane models pushed in the positive direction: (a) unstrengthened model at its peak capacity (b) strengthened model at the peak capacity of the unstrengthened model (c) strengthened model at its peak capacity

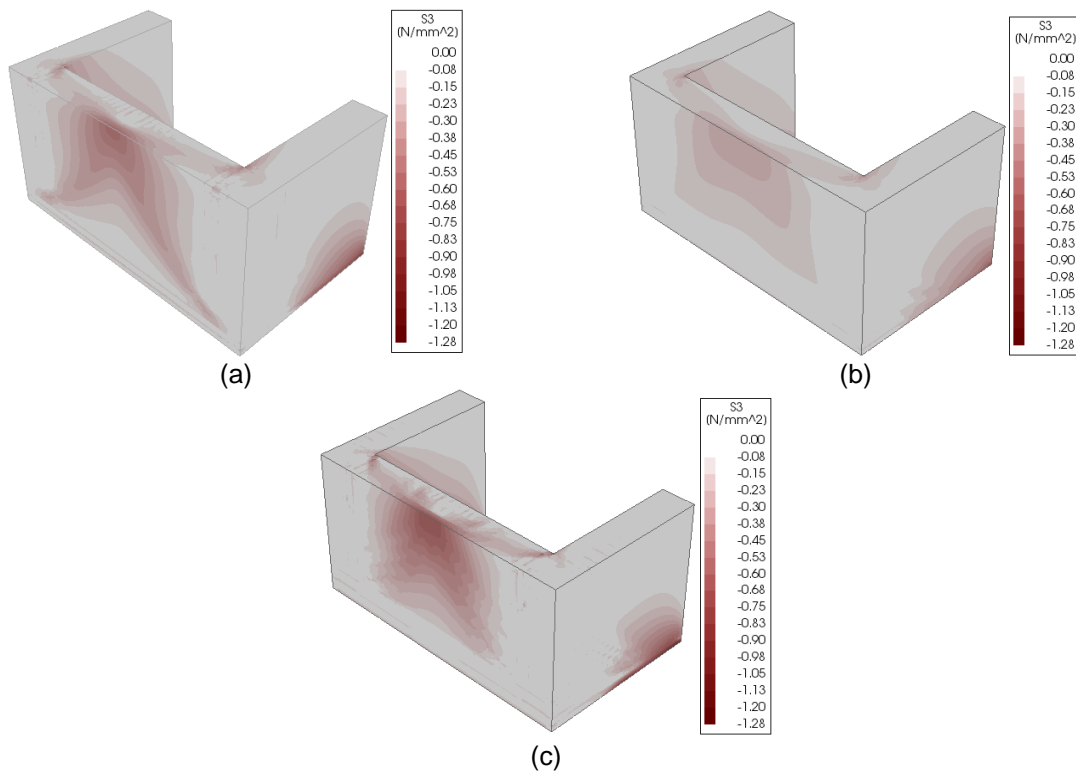


Figure 92 - Principal compressive stresses of the out-of-plane models pushed in the positive direction: (a) unstrengthened model at its peak capacity (b) strengthened model at the peak capacity of the unstrengthened model (c) strengthened model at its peak capacity

The contours of the principal tensile strains of the out-of-plane models (both strengthened and unstrengthened) pushed toward the wing walls are illustrated in Figure 93. As it can be seen, the bending of the web's mid-section and cracks at the connections of the web with wing walls are completely prevented in the strengthened model subjected to a load factor equal to the peak capacity of the unstrengthened model. Moreover, the tensile strains at the base of the strengthened model are less than that of the unstrengthened one, which reveals the efficiency of the adopted strengthening technique in controlling the damage of the wall.

By investigating the principal tensile strains of the strengthened model at its peak capacity it is possible to observe that a considerable portion of the web tends to bend. Significant cracks were also observed in the connection of the web and the wing walls. In conclusion, the adopted strengthening technique may change the failure mechanism of the out-of-plane model pushed in the positive direction from the mid-section bending failure of the web to a mixed mode including the bending of the web and the shear failure of the web at the wings.

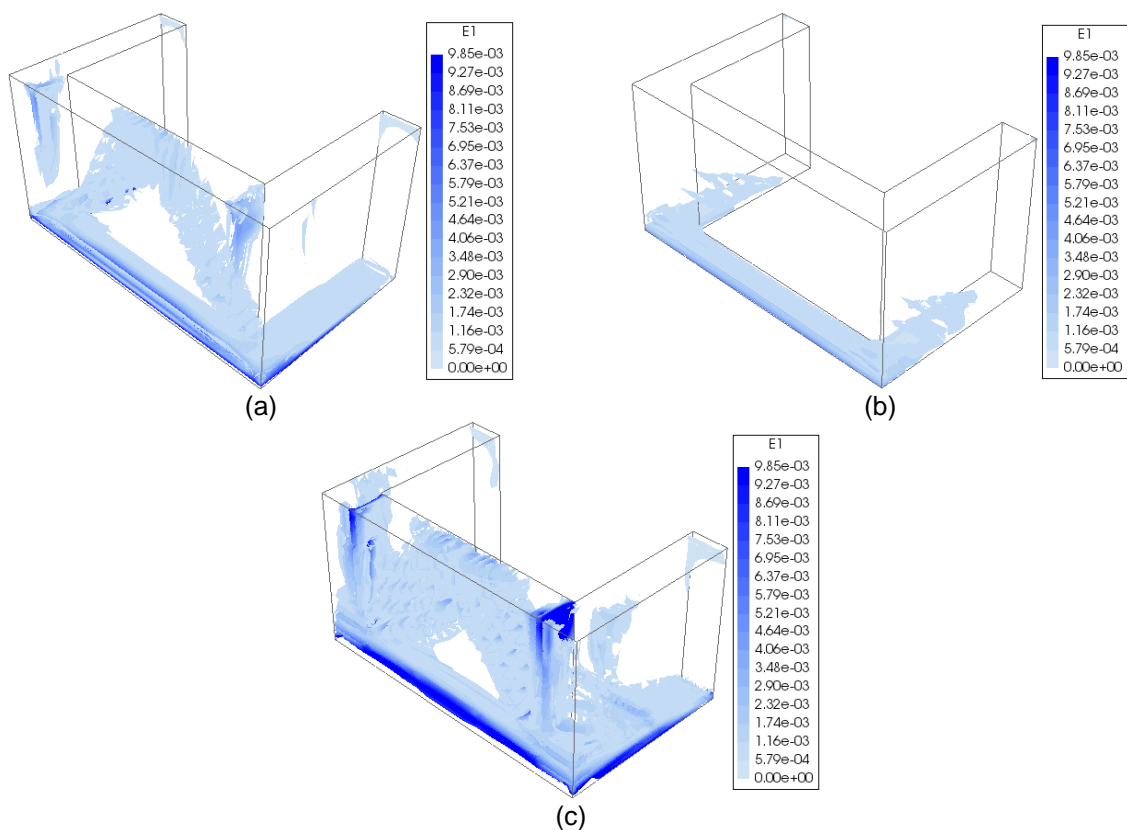


Figure 93 - Principal tensile strains of the out-of-plane models pushed in the positive direction: (a) unstrengthened model at its peak capacity (b) strengthened model at the peak capacity of the unstrengthened model (c) strengthened model at its peak capacity

Finally, the stress and strain states of the strengthening at the peak capacity of the strengthened out-of-plane model pushed in the positive direction is shown in Figure 94. The regions around the

connection between the web and the wings are intensively damaged. Therefore, the employed strengthening technique efficiently works for enhancing out-of-plane seismic performance of rammed earth walls.

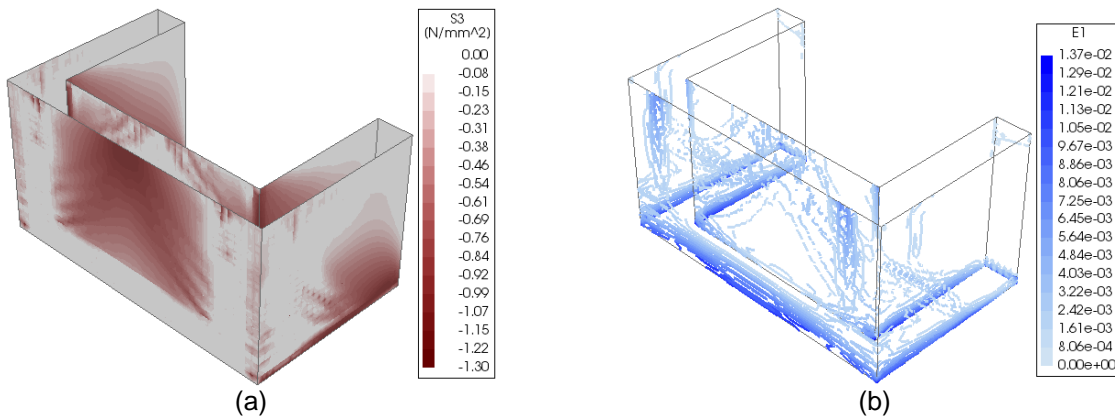


Figure 94 – Damage state of the TRM on the out-of-plane strengthened model pushed in the positive direction at its peak capacity: (a) principal compressive stresses (b) principal tensile strains

#### 4.7. Influence of the damage on the dynamic properties

In this section, a similar approach to that presented in Section 3.9 was followed to investigate the changes in frequencies of the strengthened models. As the damage developed in the models decreases the frequencies, then fewer changes can be interpreted as the efficiency of the strengthening in limiting of damage. The reduction in frequencies of the both in-plane and out-of-plane models are presented in Figure 95. Furthermore, the HMs from the unstrengthened models with the greatest change in frequency are also illustrated for comparison objectives.

By comparing the changes in frequencies of the modes with the highest contribution in the in-plane model it is possible to verify that the highest drop in the unstrengthened model was of 18%, however, this value for the strengthened model at the same lateral displacement equals 12%. This lateral displacement corresponds to the value experienced by the unstrengthened model at its peak capacity. It can be concluded that the adopted strengthening limits the damage development in the wall. Thereported values do not correspond to the same lateral load level since the strengthened model is stiffer than the unreinforced one. Therefore, the strengthened model experiences fewer damages at greater lateral loads. Similarly, the initial frequency of the unstrengthened out-of-plane model pushed in the negative direction experiences about 30% drop, whereas the corresponding value for the strengthened model is about 22%. The strengthening applied in the out-of-plane model pushed in the positive direction caused the drop in frequency to shift from 30% loss to about 19%.

Furthermore, it can be seen for the out-of-plane models that the experienced damage, even at the peak capacity of the strengthened model, are less than that of the unstrengthened model. It should be noted that this thought is not valid for the in-plane model. This situation can be interpreted by the prevention of brittle failures at the out-of-plane models, which cause considerable damages at the walls.

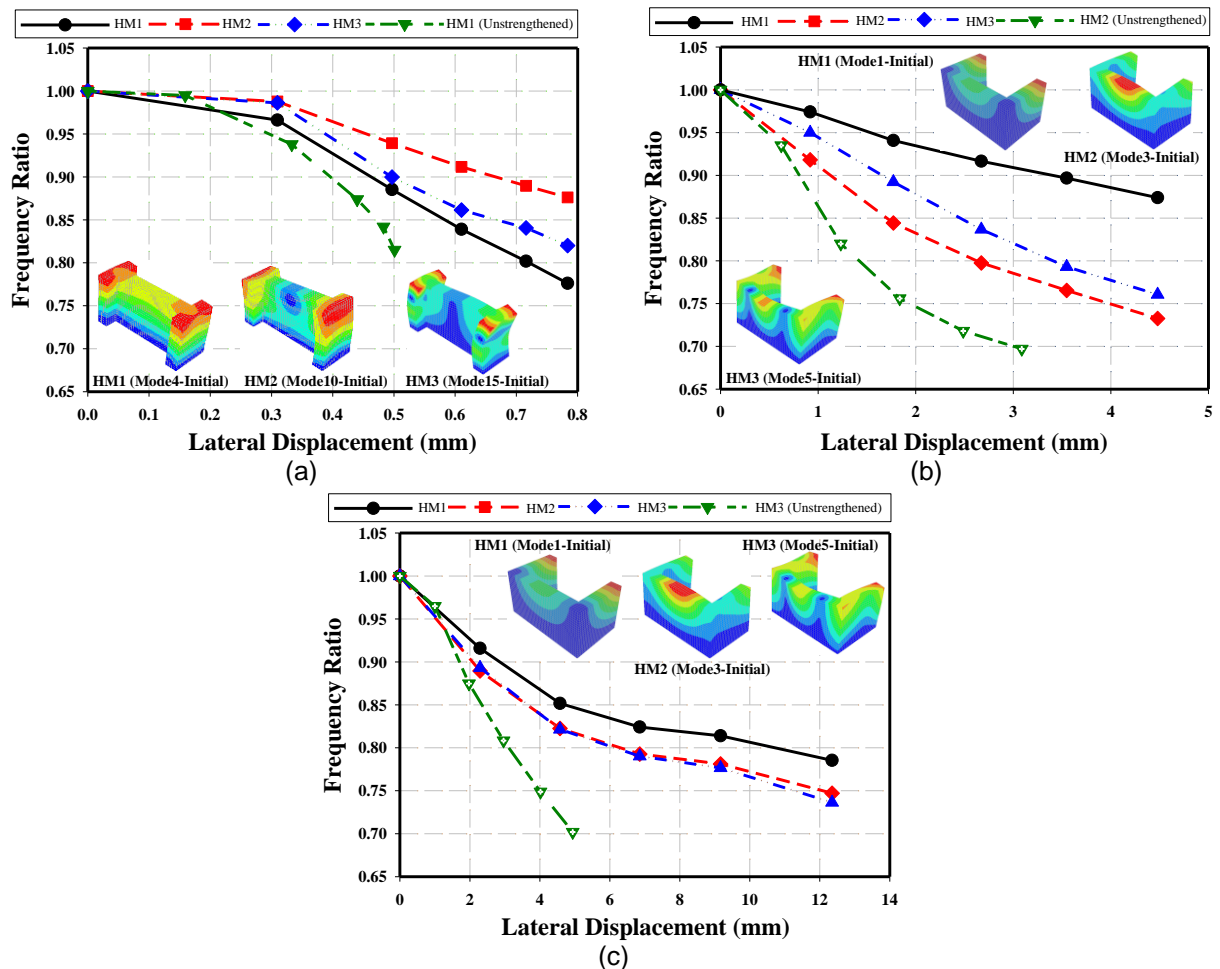


Figure 95 – Changes in frequencies of the strengthened models during the pushover analyses: (a) in-plane model (b) out-of-plane model pushed in the negative direction (c) out-of-plane model pushed in the positive direction

Finally, the changes in the modal mass participation were also investigated (see Figure 96). As it was expected, no significant changes in the modes with respect to the unstrengthened case were observed. However, in the in-plane model the HM2 decreases in spite of the unstrengthened model.

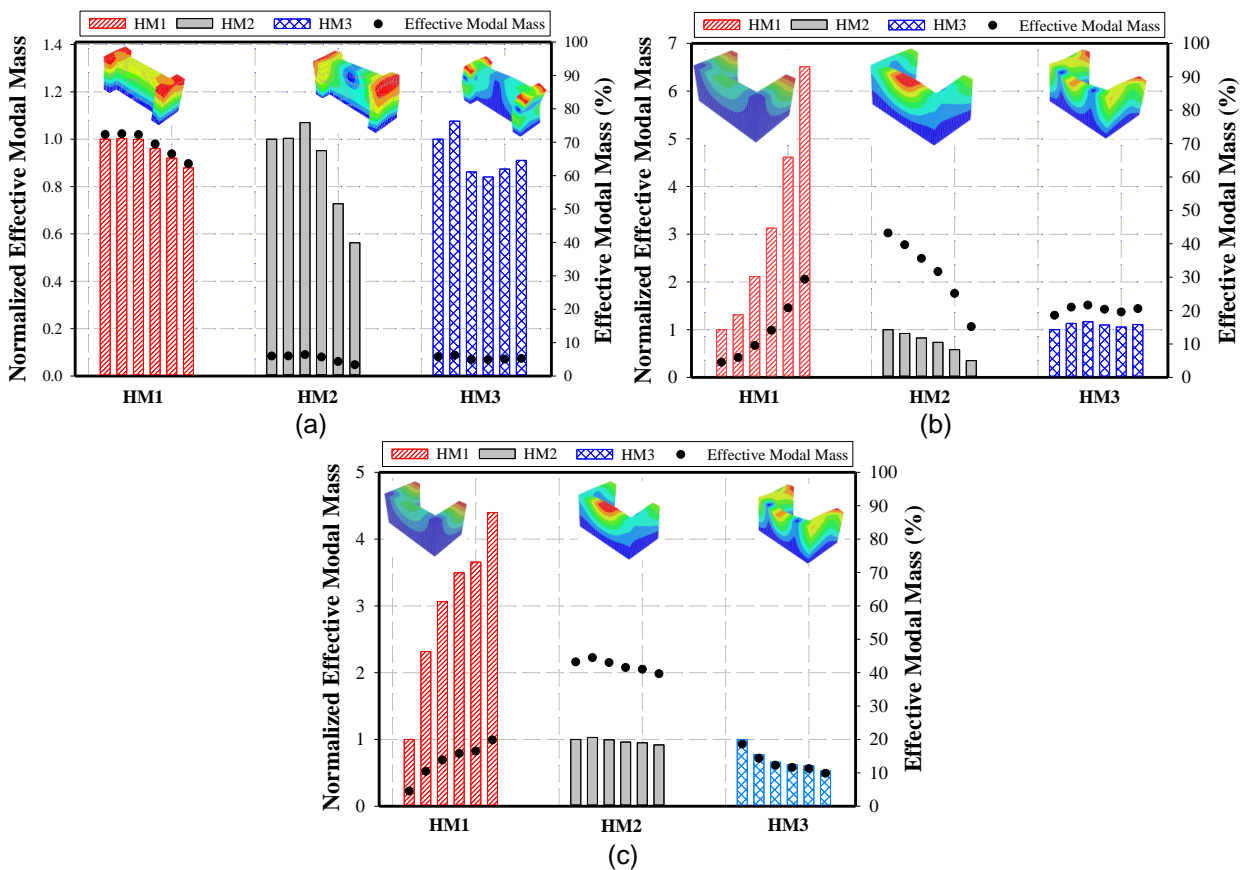


Figure 96 – Changes in the effective modal mass of the strengthened models during the pushover analyses: (a) in-plane model (b) out-of-plane model pushed in the negative direction (c) out-of-plane model pushed in the positive direction

#### 4.8. Concluding remarks

The main remarks of Chapter 4 can be summarized as follows:

- The lateral stiffness was slightly increased in both in-plane and out-of-plane strengthened models with respect to the unstrengthened ones, however the damage initiation state remained basically unchanged.
- The strengthening solution in the in-plane model leads to 56% and 21.3% increases in displacement and load capacities, respectively.
- It was shown that the strengthening controls the formation of the diagonal shear crack in the web and detachment of the right wing from the web in the strengthened in-plane model subjected to a lateral load equal to the peak capacity of the unstrengthened model.
- A larger diagonal shear crack was observed at the web of the strengthened in-plane model at a lateral load equal to its peak capacity in comparison to the peak capacity. Therefore, the

adopted strengthening leads to further exploration of the bearing capacity of larger wall sections against seismic loads. Furthermore, the right wing does not detach from the web exactly in their connection, but also a portion of the web sways with it.

- The adopted strengthening solution leads to 45% and 28% enhancement in displacement and load capacity of the out-of-plane model pushed in the negative direction, respectively.
- The applied strengthening causes much smoother failure (post-peak behavior) in the out-of-plane model pushed in the negative direction.
- The unstrengthened out-of-plane model pushed in the negative direction fails due to the bending of the web's mid-section and its detachment from the wing walls. This failure was completely avoided by the strengthened model at the same load level. On the other hand, a larger section of the web in the strengthened model tends to fail, requiring higher load levels to lead to failure.
- The adopted strengthening solution caused the displacement and load capacities of the out-of-plane model pushed in the positive direction to be increased about 131% and 30%, respectively.
- The Investigation of the principal compressive stresses and tensile strains in the strengthening at the peak capacity of the strengthened models showed an efficient contribution of the TRM composite.
- The Investigation of the frequencies reductions at increasing lateral displacement showed that the strengthened in-plane model experiences less reduction when compared with the unstrengthened model. The same trend was observed for the out-of-plane model pushed in both directions.



This page is left blank on purpose.

## CHAPTER 5

# TIME-HISTORY ANALYSES OF UNSTRENGTHENED AND STRENGTHENED RAMMED EARTH WALLS

### 5.1. Introduction

The current chapter investigates the structural response of considered walls subjected to ground motions, but due to the time-consuming process of nonlinear time-history analyses, where the responses are assessed under excitation of an earthquake. This artificially generated ground motion record is representative of the national code for the region of Odemira, in southern Portugal. In addition, the influences of the adopted strengthening solution on the dynamic responses were evaluated and relevant comparisons with the outcomes obtained from the pushover were made.

### 5.2. Seismic input

Since the considered walls are expected to be tested on a shaking table, it becomes necessary to define proper ground motion records. The applied ground motions can be selected from previous records, artificially with basis on desired characteristics or generated synthetically from seismological models and fault dimensions; although this is not an easy task. Up to now, more than 40 different approaches for seismic input selection have been introduced in the literature (Haselton *et al.*, 2009). They can be generally categorized in the following groups:

- Selection based on Magnitude ( $M$ ) and source to record distance ( $R$ ). This procedure is the most common in seismic design regulations and standards.

- Selection by means of uniform hazard spectrum (UHS) or conditional mean spectrum (CMS). In this method, ground motion records are selected in a way that their spectral shape is similar to that of the target UHS. This is done by calculating epsilon ( $\epsilon$ ) value of the records, which is defined as the logarithmic standard deviation of record's spectral acceleration from the UHS (FEMA P695, 2009). The other method (based on CMS) is relatively similar, but the target spectrum in its process belongs to the expected earthquake.

It should be noted that selecting ground motion records from previous events may not exactly satisfy seismological conditions of the site in study, meaning that scaling them may be required. Furthermore, artificial ground motion records may not precisely represent the frequency and energy contents of a real earthquake. Several scaling methods are proposed in the literature, such as the linear scaling based on the design spectrum in a range of periods around its fundamental period or the spectral matching method. It was observed that different outcomes may be resulted from each scaling method. For instance, linear scaling approach as the most common method in seismic design regulations may cause smaller demands in comparison of those obtained from spectrum matching method (Allahvirdizadeh *et al.*, 2013).

Therefore, the first step for proper earthquake selection is to characterize the design spectrum parameters from the site in study. Since rammed earth constructions are typically found in southern Portugal, namely in the region of Alentejo, this region was considered for the aforementioned objective. The seismic hazard map of the Portugal for earthquakes with 475 years returning period and the location of the region in study, namely Odemira municipality (Alentejo) are illustrated in Figure 97.

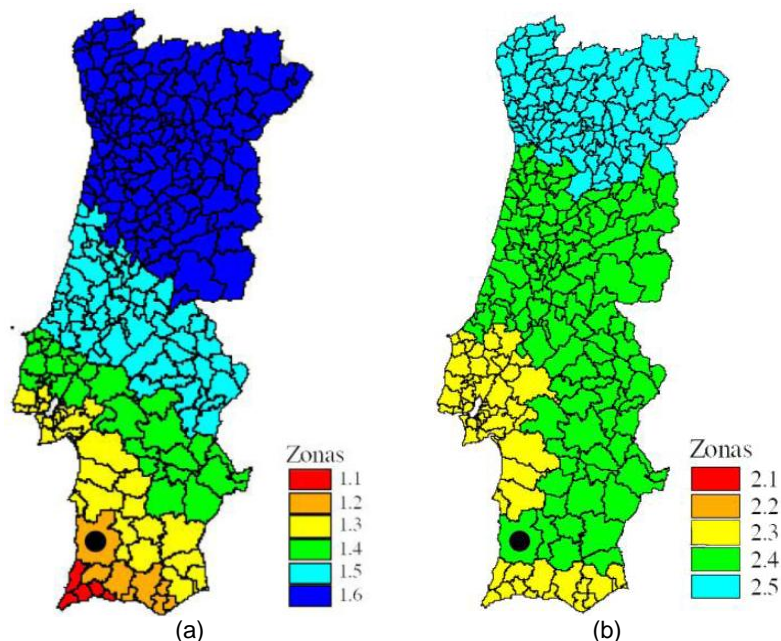


Figure 97 – Portuguese seismic hazard map for earthquakes with 475 years returning period (site in study marked with a black dot): (a) type 1 (far-field earthquakes) (b) type 2 (near-field earthquakes) (Norma Portuguesa, 2009)

Consequently, the seismic parameters and the corresponding design spectra are presented in Table 19 and Figure 98a, respectively. According to the Portuguese national code (Norma Portuguesa, 2009), two types of elastic design spectra must be considered, i.e. far-field (denoted as type 1) and near-field (denoted as type 2). In the present study the artificial ground motion record generation is adopted. In this regard, the *Simqke-gr* software, developed at University of Brescia was employed to generate artificial ground motion records compatible with both elastic design spectra. The ground motion records were generated based on the design spectra of the region, whose parameters are presented in Table 19. These parameters define the backbone of the records as schematized in Figure 98b.

Table 19 – Seismic parameters of Odemira municipality (Alentejo region) for an earthquake with 475 years returning period and respective artificial ground motion duration parameters

Type of Seismic Action	$a_g$ ( $m/s^2$ )	Elastic Response Spectra				Artificial Earthquake Duration			
		$S_{max}$ (sec)	$T_B$ (sec)	$T_c$ (sec)	$T_D$ (sec)	Rise (sec)	Steady (sec)	Fall (sec)	Total (sec)
1 (Far-field)	2.0	1.0	0.1	0.6	2.0	3.0	30.0	3.0	36.0
2 (Near-field)	1.1	1.0	0.1	0.25	2.0	2.0	10.0	2.0	14.0

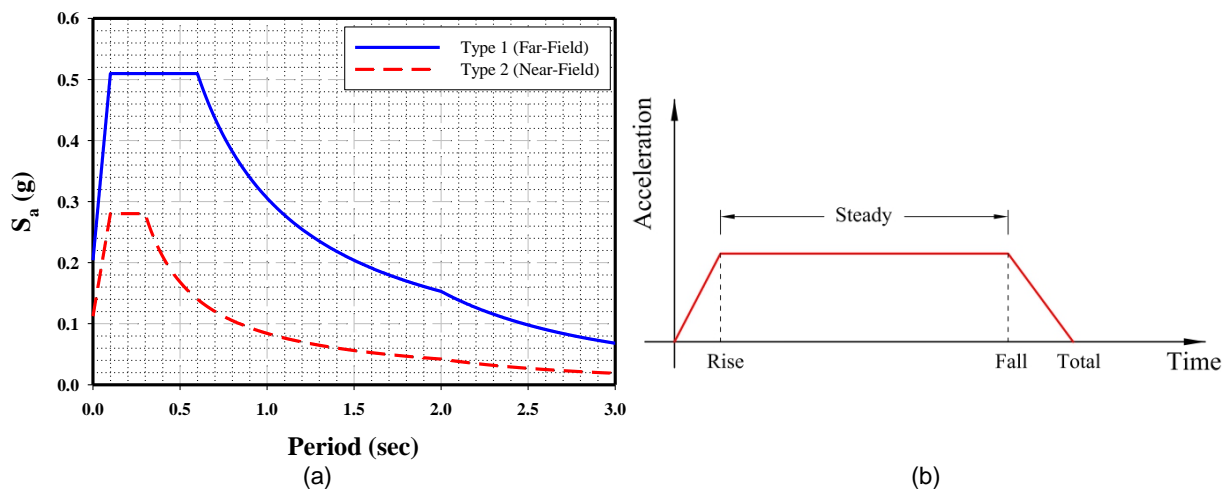


Figure 98 – Definition of the parameters for generating ground motion records: (a) design spectrum for type 1 and 2 earthquakes (b) schematic backbone of the artificially generated records

Subsequently, the *SeismoSignal* software was used to perform a baseline correction on the generated ground motion records by filtering the frequencies below 0.1 Hz and above 20.0 Hz. A sample of generated records is shown Figure 99.

It is recommended that the artificial ground motion records are made compatible with the local elastic design spectra. In this regard, the spectral acceleration and displacement spectra of each of group of records are compared with 5% elastic response spectra of the code (see Figure 100 and Figure 101).

Due to the very demanding time-consuming process associated to nonlinear time-history analysis, only one accelerogram representative of the type 2 earthquake (near-field) was considered in this chapter.

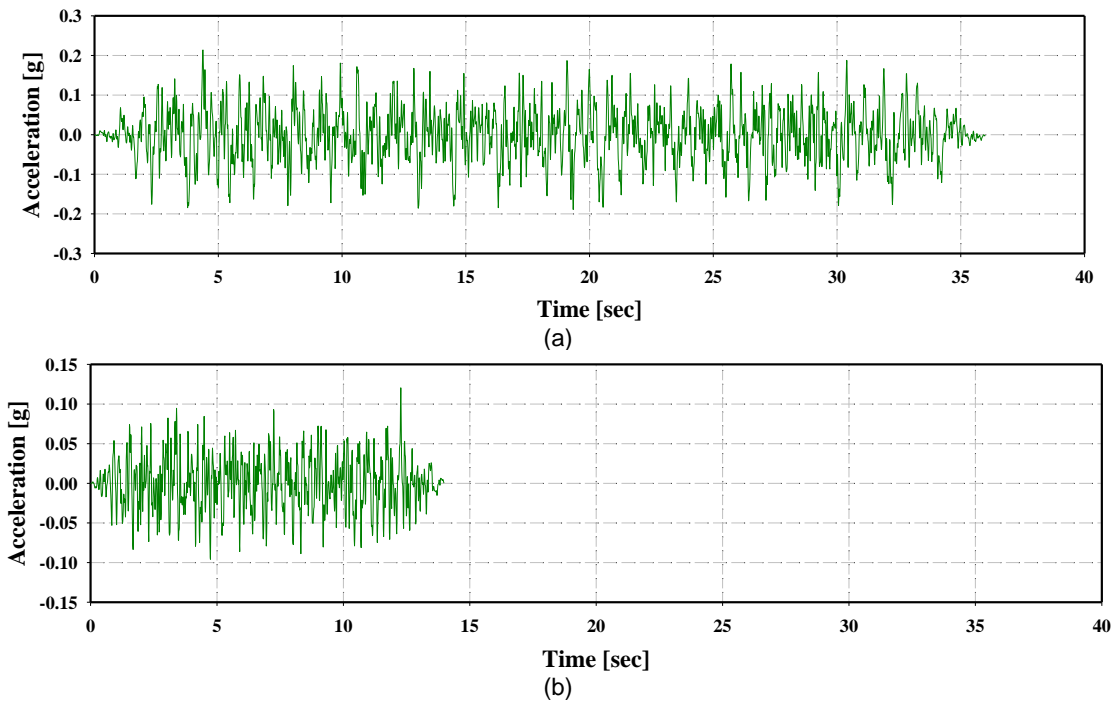


Figure 99- Sample of generated artificial ground motion records: (a) type 1 (b) type 2

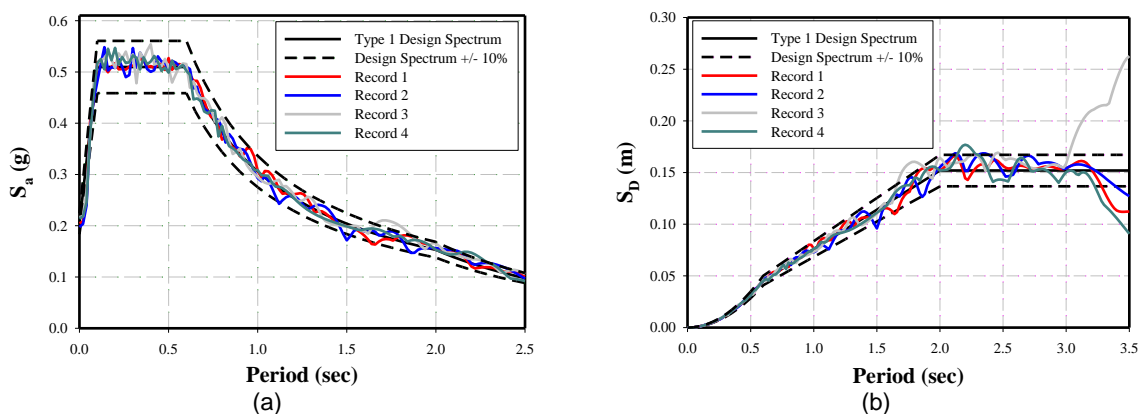


Figure 100- Compatibility of the generated type 1 ground motion records with: (a) spectral design acceleration (b) spectral design displacement

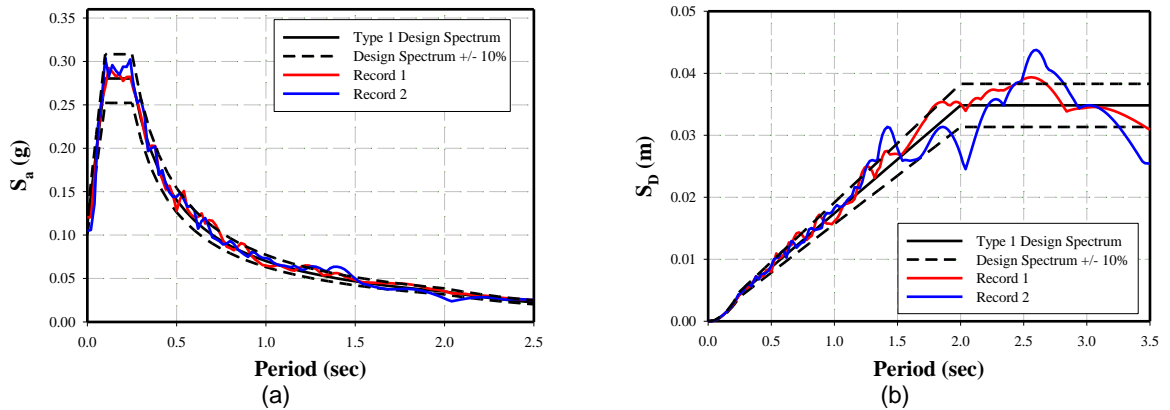


Figure 101- Compatibility of the generated type 2 ground motion records with: (a) spectral design acceleration (b) spectral design displacement

### 5.3. Damping ratio

In order to conduct nonlinear time-history analyses, it is vital to define a proper damping ratio of the system to take into account the energy dissipation. In this regard, the Rayleigh viscous damping approach is adopted, which evaluates the damping matrix based on the linear combination of the mass ( $M$ ) and stiffness ( $K$ ) matrices as presented in equation (10) (Chopra, 2012).

$$C = \alpha M + \beta K \quad (10)$$

Where,  $\alpha$  and  $\beta$  are the coefficients weighting the contribution of the mass and stiffness matrices on the damping matrix. These coefficients are related to the damping ratios associated with the natural frequencies of the dominant modes of vibration. Therefore, their calculation requires selecting the principal modes and assigning the corresponding damping coefficient. Finally, these parameters are calculated using equations (11) and (12):

$$\alpha = \xi \left( \frac{2\omega_i \omega_j}{\omega_i + \omega_j} \right) \quad (11)$$

$$\beta = \xi \left( \frac{2}{\omega_i + \omega_j} \right) \quad (12)$$

Where,  $\omega_i$  and  $\omega_j$  are the natural frequencies of the  $i$ -th and  $j$ -th modes of vibrations, respectively, and  $\xi$  is the damping ratio. These natural frequencies should be chosen in a way that the constructed damping matrix correctly characterizes the dissipative behavior of the components in the desired frequency range. It is recommended that, the selected modes lie in the linear or undamaged state of the structure, while as previously observed the rammed earth walls crack rapidly. In this regard, the modes with significant mass participation are selected. It is worthwhile to mention that, the modes in X-direction were used for the in-plane model and those in Y-direction were used for the out-of-plane model. Furthermore, there is no general consensus about the damping ratio value in rammed earth

constructions. In this regard, it was considered as 3%. Considering all, the selected dominant modes of vibration and corresponding coefficients of Rayleigh damping for both in-plane and out-of-plane models are presented in Table 20.

Table 20- Selected modes and calculated parameters for Rayleigh damping

In-Plane Model					
Mode	Frequency (Hz)	$\omega$ (rad/s)	Effective Mass Participation (%)	$\alpha$	$\beta$
4	38.314	240.61	72.0	9.942	7.764e-5
10	84.746	532.2	6.4		
Out-of-Plane Model					
3	25.641	161.02	40.0	5.952	1.431e-4
5	41.152	258.4	21.4		

Finally, the damping ratio at different frequencies (modes of vibration) was obtained using equation (13):

$$\xi_n = \frac{1}{2}(\beta\omega_n + \alpha\omega_n) \quad (13)$$

Where, all parameters are previously defined. Then, the variation of damping ratio at different frequencies is shown in Figure 102.

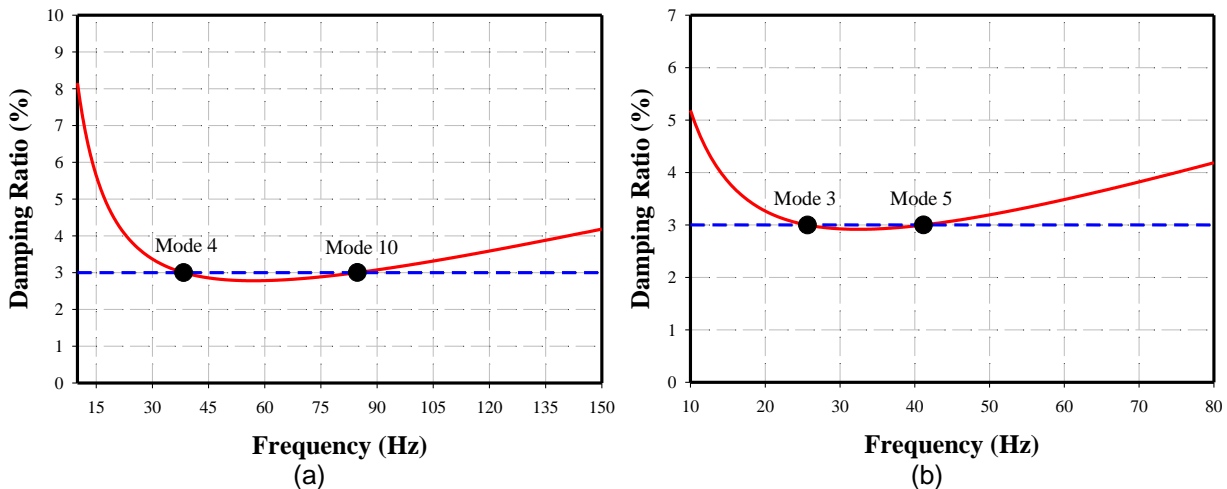


Figure 102- Variation of damping ratio with the frequency of the modes (a) in-plane model (b) out-of-plane model

#### 5.4. Time-integration method

Rapid/high variation of the applied ground motion during transient analyses and the initiation/distribution of nonlinearity in the structure lead to the absence of analytical solutions to be available for nonlinear time-history problems. Therefore, performing a time-integration of the

differential equations of dynamic problems seems to be inevitable. In this regard, several methods have been implemented in the literature; while all should fulfill the following three fundamental criteria:

- Convergence: decreasing the time-step size ( $\Delta t$ ) should lead to exact solution.
- Stability: existence of numerical round-off errors should not affect the stability of the method.
- Accuracy: The obtained outcomes should satisfactorily match with the exact outcomes.

Generally speaking, the proposed numerical methods can be classified in two major groups, i.e. explicit and implicit methods. In the explicit method, unknowns at each step are calculated based on the previous step. It is evident that increasing the time-step size can drastically affect the stability of these approaches. On the other hand, the implicit methods evaluate the response at each step by solving the equations of motion in that step.

In the current study, the Hilber-Huges-Taylor (HHT) method, as one of the proposed implicit approaches, was adopted. This method implements a damping for the possible noises in the captured responses due to rapid stiffness changes. Such issues are likely to happen in rammed earth constructions due to the inherent nonlinear response and probable brittle failures. The proposed finite difference equations in this method are as follows:

$$\dot{u}^{t+\Delta t} = \dot{u}^t + \left[ (1-\gamma)\ddot{u}^t + \gamma\ddot{u}^{t+\Delta t} \right] \Delta t \quad (14)$$

$$u^{t+\Delta t} = u^t + \dot{u}^t \Delta t \left[ \left( \frac{1}{2} - \beta \right) \ddot{u}^t + \beta \ddot{u}^{t+\Delta t} \right] \Delta t^2 \quad (15)$$

Where,  $u$ ,  $\dot{u}$  and  $\ddot{u}$  are displacement, velocity and acceleration at each time step, respectively;  $\gamma$  and  $\beta$  are parameters associated to the Newmark's method. The proper selection of the latter parameters can lead the HHT method to be unconditionally stable. They can be calculated using following equations:

$$\gamma = \frac{1}{2}(1-2\alpha) \quad (16)$$

$$\beta = \frac{1}{4}(1-\alpha)^2 \quad (17)$$

Where,  $\alpha$  is the parameter of HHT method. By eliminating this parameter, the HHT method corresponds to the Newmark's method. This parameter is indirectly related to the aforementioned noise damping of the HHT method and it varies in range of -1/3 to the 1/2. In the current study, the default values of the software were considered.

Consequently, velocity and displacement at each step (obtained from equations (14) and (15)) are substituted in the equations of motion of a multi-degrees-of-freedom system as expressed in equation (18), which results in equation (19):



$$M\ddot{u}^{t+\Delta t} + C\dot{u}^{t+\Delta t} + Ku^{t+\Delta t} = f_{ext}^{t+\Delta t} \quad (18)$$

$$M\ddot{u}^{t+\Delta t} + (1+\alpha)C\dot{u}^{t+\Delta t} - \alpha C\dot{u}^t + (1+\alpha)f_{int}^{t+\Delta t} - \alpha f_{int}^t = (1+\alpha)f_{ext}^{t+\Delta t} + \alpha f_{ext}^t \quad (19)$$

Where,  $M$  is the mass matrix,  $C$  is the damping ratio matrix,  $K$  is the stiffness matrix,  $f_{int}$  is the vector of restoring loads (obtained from equation(20)) and  $f_{ext}$  is the vector of external loads.

$$f_{int} = Ku \quad (20)$$

Finally, it is essential to select the appropriate time-step size, which, is a function of both duration of the applied ground motion record and also of the frequencies of the structure. Nevertheless, it is recommended not being greater than 1/10 of the relevant periods of the model. In the case of the considered models for the rammed earth walls, the fundamental period is considered as that of the mode with the highest mass participation. These selected time-step size for the both in-plane and out-of-plane models are presented in Table 21.

Table 21 – Selected time-step size in the nonlinear time-history analyses

Model	Fundamental Frequency (Hz)	Fundamental Period (sec)	T/10 (sec)	Employed $\Delta t$ (sec)
In-Plane	19.92	0.0502	0.00502	0.001
Out-of-Plane	18.382	0.0544	0.00544	0.001

## 5.5. Time-history analyses

In this section, one of the generated artificial ground motion records, based on type 2 (near-field) design spectrum, was applied to the models to investigate the nonlinear dynamic behavior of the rammed earth walls. The conducted nonlinear time-history analyses revealed to be excessively time-consuming, whereby the results here are presented only for one ground motion record.

### 5.5.1. In-plane models

The time-history of the lateral displacements captured at the control node on the top of the right wing for the both unstrengthened and strengthened models are shown in Figure 103. As it can be seen, the maximum absolute experienced lateral displacement for the unstrengthened model equals 0.0337 mm. With respect to the outcomes of the previously conducted pushover analyses, damage in the unstrengthened in-plane model initiate at a lateral displacement equal to 0.1226 mm. It should be noted that there is no guarantee for the latter displacement to be the damage initiation point under

dynamic loadings. However, it can be understood that the unstrengthened in-plane model will probably remain elastic under excitation of the adopted ground motion. On the other hand, it can be seen that the strengthened model experiences slightly less lateral displacements than the strengthened model (see Figure 103b). This situation is due to the increased lateral stiffness of the wall due to the application of the LC-TRM composite.

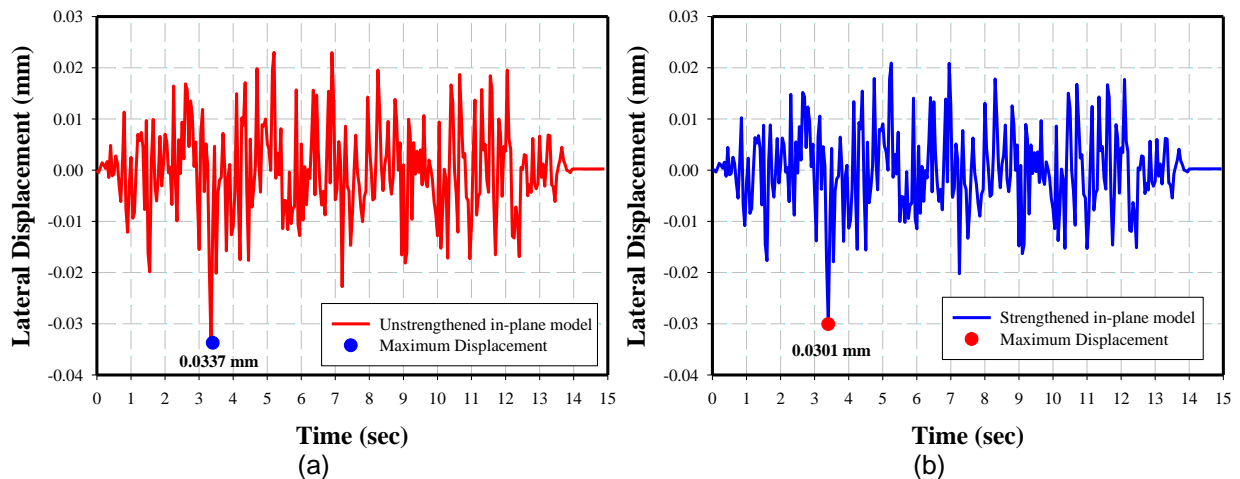


Figure 103 – Time-history of the displacements of the in-plane model: (a) unstrengthened (b) strengthened

Similarly, the time-history of the normalized base shear to the weight of the model (denoted as load factor  $\alpha$ ) for the both unstrengthened and strengthened in-plane models are presented in Figure 104. It should be noted that from the design point of view, it is important to assess the capability of conventional rammed earth components and sections to withstand against possible earthquakes. As it can be seen, the maximum absolute load factor of the unstrengthened model equals 0.15 (see Figure 104a). With respect to the pushover analyses, the unstrengthened in-plane model has a peak capacity equal to 1.75. Thus, rammed earth components from the Alentejo region and with geometry similar to that of the model are expected to easily resist against the lateral design earthquake loads applied within their planes. Nevertheless, it is necessary to take into account that the behavior of the components in cooperation with other elements of the building may differ. Hence, the proposed conclusion cannot be taken as completely valid.

On the other hand, the maximum induced load factor to the strengthened model equals to 0.16 (see Figure 104b). This slight increase is due to the application of the LC-TRM, which increases the mass of the wall and consequently the induced inertial demands. Nevertheless, this load factor is still much lower than the one obtained from the pushover analysis (namely 2.13), it is expected that the strengthened model would be able to resist to stronger earthquakes.

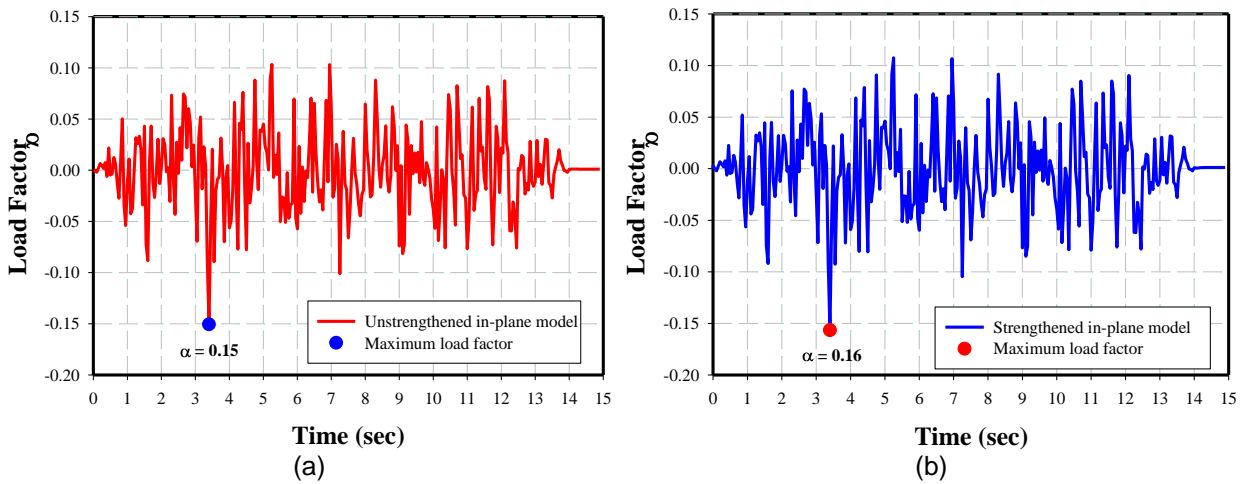


Figure 104 – Time-history of the load factor of the in-plane model: (a) unstrengthened (b) strengthened

Therefore, it is expected for the in-plane model not to surpass elastic limits of the behavior. As it is evident from the shown hysteretic behavior for the both strengthened and unstrengthened models in Figure 105, the behavior remained linear elastic.

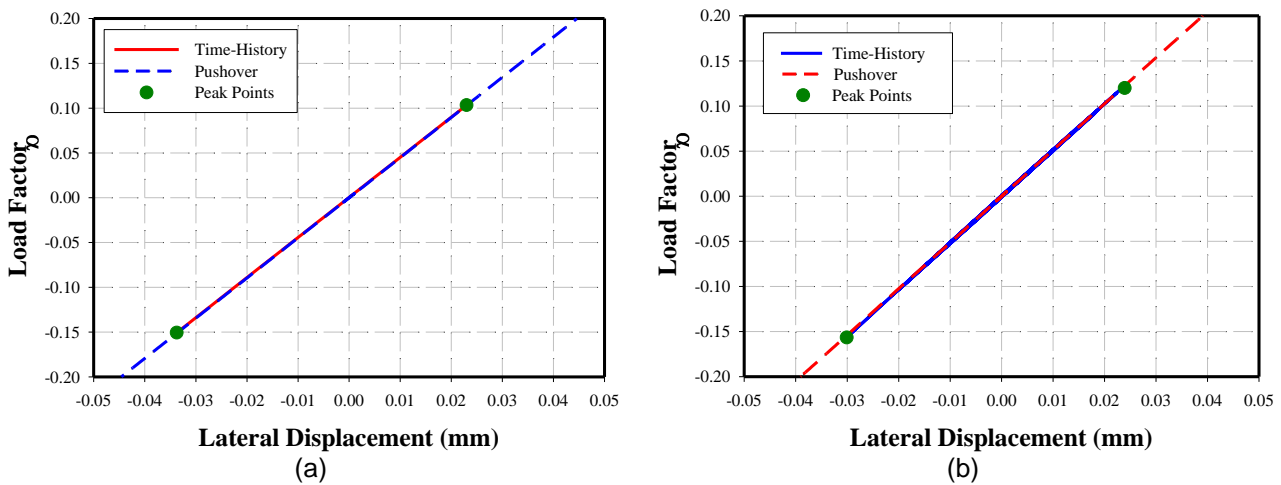


Figure 105 – Hysteretic behavior of the in-plane models: (a) strengthened (b) unstrengthened

In addition, the maximum principal tensile strains experienced during the whole time-history analyses, for the both unstrengthened and strengthened in-plane models are presented in Figure 106. As it can be seen, no crack was developed neither in the strengthened model nor in the unstrengthened one. Therefore, the scale of the contours was set based on the strain at the tensile strength. This enables to understand the most vulnerable regions to damage. As it is evident, the connection between the wing walls and the web are likely to damage.

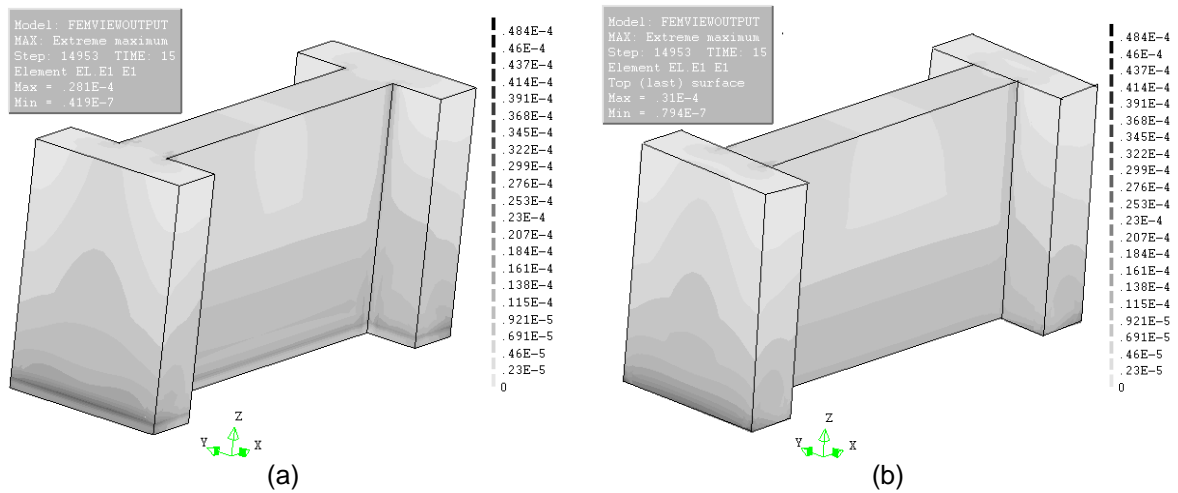


Figure 106 – Maximum principal tensile strains experienced by the in-plane models subjected to the ground motion: (a) unstrengthened (b) strengthened

### 5.5.2. Out-of-plane models

A similar approach to that followed in the previous section is now used to analyze the dynamic behavior of both strengthened and unstrengthened out-of-plane models.

The time-history of the lateral displacements at the control node on top of the web's middle section for both strengthened and unstrengthened out-of-plane models are shown in Figure 107.

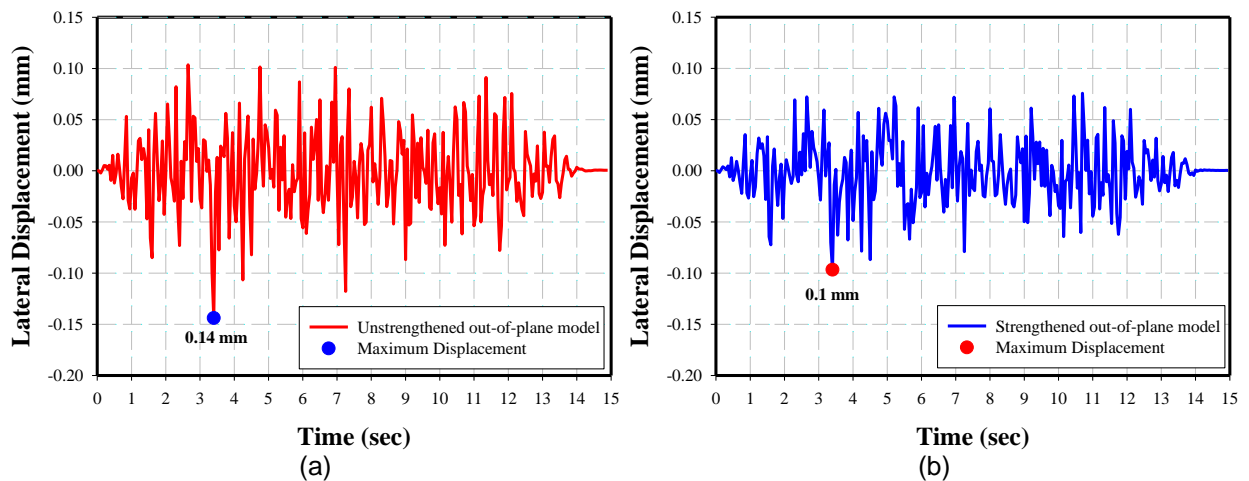


Figure 107 – Time-history of the displacements of the out-of-plane model: (a) unstrengthened (b) strengthened

The lateral displacement corresponding to the damage initiation at the unstrengthened out-of-plane model when pushed in the negative direction (the severe case) was of about 0.17 mm. In the case of the maximum lateral displacement obtained from the nonlinear time-history analysis, it equals 0.14 mm, which gets close to the static damage initiation one. In this regard, the unstrengthened out-of-plane model may experience some cracks. This statement requires investigating the principal tensile

strains at the model. On the other hand, the maximum absolute lateral displacement of the strengthened model equals 0.1 mm. This reduction is due to the increased lateral stiffness by application of LC-TRM strengthening on the wall.

Furthermore, the hysteretic curves of both strengthened and unstrengthened models are presented in Figure 108. These curves evidence that the model underwent under nonlinear behavior. In order to compare the obtained responses from the nonlinear time-history analyses with those obtained from the pushover analyses, the envelope of the hysteretic behavior and peak points were distinguished. A series of peak points were selected following two different approaches, namely the point with the highest load factor and the point with the highest lateral displacement. The points obtained from both approaches are highlighted in the curves.

As it can be understood from the curves, the negative direction (direction to the outside of the wing walls) experiences higher deformations. This behavior was somehow expected considering the results from the pushover. As it can be seen, the lateral displacements in the negative direction are considerably decreased in the strengthened model. In other words, the nonlinear behavior observed in the envelope of the unstrengthened model is reduced substantially in the strengthened one. On the other hand, no major change in the positive side was observed, which can be interpreted as no relevant damage occurs in this direction for both models.

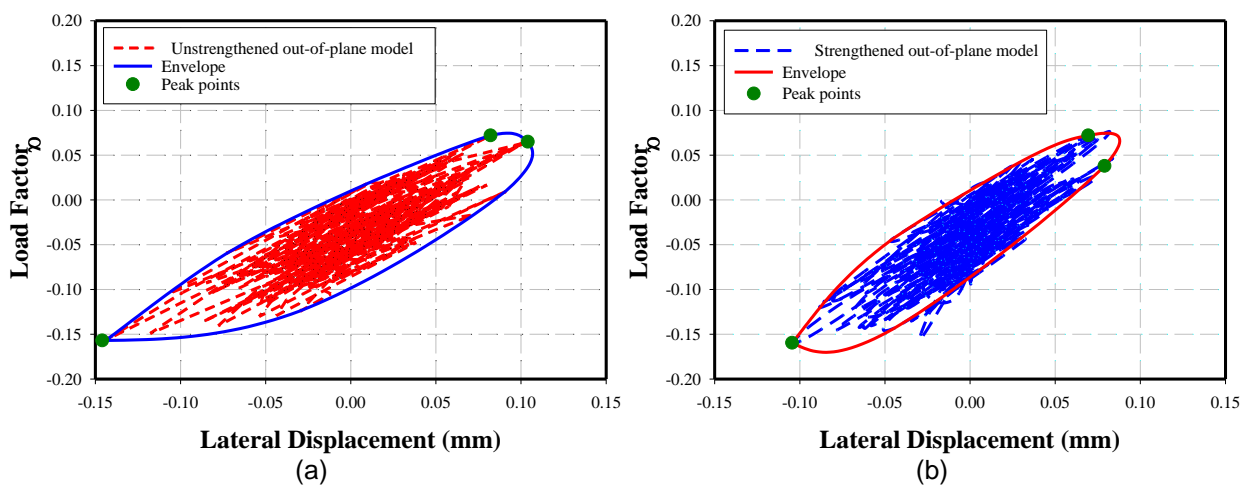


Figure 108 – Hysteretic behavior of the out-of-plane models: (a) unstrengthened (b) strengthened

In order to investigate damaged regions, the maximum principal tensile strains experienced during the whole time-history analyses, for the both unstrengthened and strengthened out-of-plane models, are presented in Figure 109. The results are shown for the both front and back views of the models to better understand the possible damaged regions. As it can be seen, damage in the unstrengthened model is likely to occur at the connections of the web to the wing walls. The tendency of the web's middle section to bend is also clear, nevertheless the section's capacity was far from being achieved with respect to the out-of-plane demands. The same vulnerable regions can be distinguished in the

strengthened model, but the principal tensile strains are decreased considerably. Therefore, fewer cracks were likely to develop, but still, the connection of the wing walls and the web are critical sections in the exploration of the out-of-plane behavior.

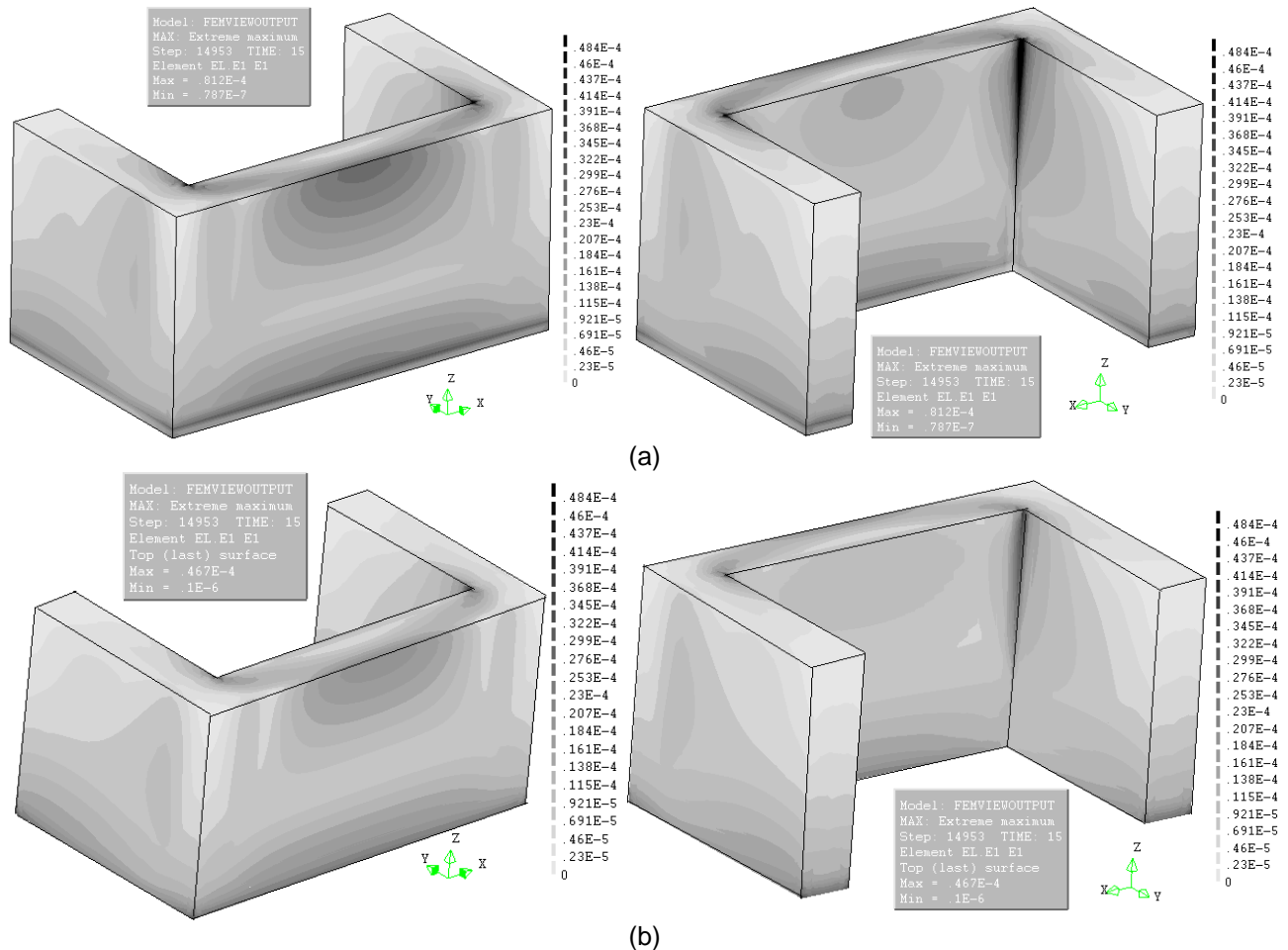


Figure 109 – Maximum principal tensile strains experienced by the out-of-plane model subjected to the ground motion: (a) unstrengthened (b) strengthened

Finally, the envelope obtained from the time-history analyses is compared with the pushover curve. These comparisons are presented in Figure 110. It should be noted that the adopted ground motion is not strong enough to cause the out-of-plane model to reach its peak capacity. Therefore, the axis boundaries of the graph are adjusted in the region of the responses captured from the time-history analyses.

The pushover analyses can acceptably predict the response of the walls. Although, in the positive side of the response, the results of the pushover analyses are in better agreement with the peak points corresponding to the maximum load factor. On the other hand, there is no guarantee that the pushover analysis is equally accurate also for higher damage levels.

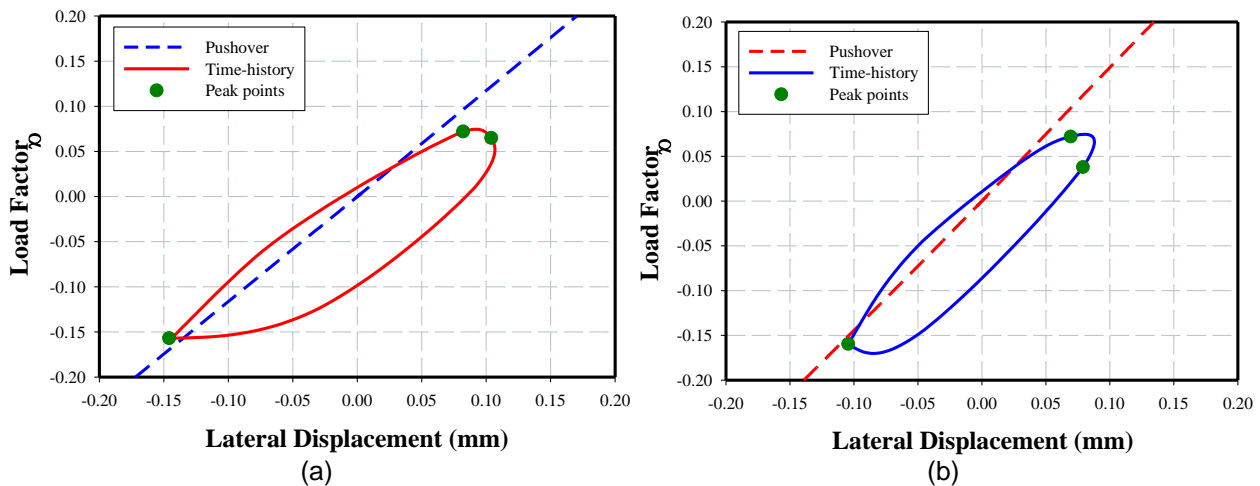


Figure 110 – Hysteretic behavior of the out-of-plane models in comparison with the pushover curve: (a) unstrengthened (b) strengthened

## 5.6. Concluding remarks

The main remarks of Chapter 5 can be summarized as follows:

- The in-plane model experiences approximately no damage under excitation of an earthquake proposed in the Portuguese seismic design code for Odemira (Alentejo region; earthquake type 2). This is even true for the unstrengthened wall.
- The adopted strengthening solution leads to a slightly increase in the induced seismic demands; however the experienced lateral displacements decrease.
- The maximum principal tensile strains obtained during the whole time-history analyses, of the on-plane and out-of-plane models, revealed that the pushover analyses can precisely predict vulnerable regions.
- The out-of-plane model cracks even under the excitation of a moderate earthquake.
- The envelope of the hysteretic curve obtained for the out-of-plane model acceptably matches with its pushover curve for the level of displacements reached dynamically. Its validation for higher displacement levels requires further investigation.

## CHAPTER 6

# CONCLUSIONS AND FURTHER RESEARCH

### 6.1. Main conclusions

The present thesis aimed at investigating the seismic performance of selected structural assemblages of rammed earth walls, here termed simply as walls. This objective was achieved by evaluating their in-plane and out-of-plane responses. In addition, the influence of the strengthening with textile reinforced mortars (TRM composites) on their behavior was also assessed.

Firstly, pushover analyses were conducted on the unstrengthened models to understand possible failure mechanisms, evaluate their load and displacement capacities, and select the proper geometrical dimensions and modelling approaches. It was observed that the failure in the in-plane models is mainly due to sway of the wing wall. A shear diagonal crack may also initiate and develop on the web. It was clear, that the shear crack on the web resulted mainly from the in-plane behavior of the wall. Furthermore, the obtained outcomes of the pushover analyses lead to select the wall with smaller wing walls. With respect to the out-of-plane models, detachment of the web from the wing walls and bending of the web's mid-section were the main reasons of the failure. The asymmetric geometry of the out-of-plane models caused the captured capacities to be different regarding the direction of pushing. It was observed that pushing the out-of-plane model to the outside of the wing walls results in a brittle failure, while the supporting contribution of the wing walls in the reverse pushing direction leads to ductile failure with much greater load and displacement capacities. In the latter case, the arch effect in the web was observed.

Subsequently, the comparison between shell and solid elements highlighted the higher representativeness of the models prepared with solid elements. Disregarding the thickness of



elements in the shell element modeling approach, particularly that of the web resulted in greater lateral displacements. However, in most of the cases the load capacity has been decreased. Moreover, unrealistic stress concentrations on the connections of the wing walls and the web, and evaluations of the stress contours led to select the solid element modeling approach for further investigations.

Later on, the LC-TRM strengthening technique was implemented in the models to assess the influence of this technique on seismic performance of the rammed earth walls. In this regard, two different LC-TRM solutions with different textile materials (glass and nylon) and relatively similar costs were selected. The glass textile presented higher tensile strength, while the nylon presented an extremely larger deformation capacity. The outcomes obtained from the in-plane model strengthened with each of the textiles showed that the glass mesh leads to a larger improvement on both load and displacement capacities.

The further investigation showed that the previously discussed failure modes were controlled at the strengthened models for a lateral load equal to the peak capacity of the unstrengthened wall. The observed stress and strain states of the adopted strengthening showed its proper and efficient contribution to the behavior of the wall. It should be noted that the applied strengthening technique had no influence on the damage initiation point, but made it more difficult to develop. Moreover, the final failure mechanism of the strengthened model is relatively similar to the unstrengthened one, but it allowed achieving higher capacity and ductility.

In addition to the aforementioned studies, the changes in frequencies and dynamic properties of the both strengthened and unstrengthened models were also investigated. It was observed that the modes with the highest contribution may change during the pushover analysis and at different damage states. Furthermore, a considerable reduction in the frequencies of the modes with highest contribution was observed for the unstrengthened models. The largest reduction belongs to the out-of-plane model pushed to outside of the wing walls.

The aforementioned study was also carried out for the strengthened models. In all cases, the behavior was considerably improved for the same lateral displacement level of the unstrengthened models. In other words, the adopted strengthening technique controls the damage development and softening of the wall.

Finally, an artificially generated code-compatible ground motion record was applied to the models to investigate their dynamic behavior. The generated record satisfies the Eurocode 8 regulations (near-field earthquakes) for the municipality of Odemira in southern Portugal. It was observed that, the in-plane model remains elastic when subjected to that record. The additional induced mass to the wall by the strengthening caused slightly higher loads to be applied, while its higher stiffness leads to smaller lateral displacements. In the case of the out-of-plane model, even such moderate earthquake causes damage to be initiated. The outcomes of the nonlinear time-history analyses showed that the pushover analyses may precisely predict the vulnerable regions, at least for the level of dynamic displacement

imposed. Moreover, it was seen that the pushover analyses can lead to relatively accurate load and displacement predictions for slightly damaged walls.

## **6.2. Opportunities for further research**

As part of the present study, a number of areas for further research have been identified. With respect to the modelling part, it may be important to take into account the influence of the interaction between the applied LC-TRM composite and the substrate, and also the interaction between the mesh and the mortar matrix. In the latter case, it is required to obtain previously the bond stress-slip behavior. By considering these behaviors in the numerical analyses, it is expected to allow obtaining a more comprehensive prediction of the capacity and possible failure modes.

The current thesis only focused the seismic performance of two types of structural assemblages, while, more complicated cases may occur by investigating the behavior of the full structure. For instance, the interaction between walls, the influence of existing openings, the effects of lintel and ring beams and also loads from the roof should be further investigated. Furthermore, the efficiency of the adopted strengthening technique on the building should be assessed in comparison to the other available methods.

Moreover, it is recommended to conduct incremental dynamic analyses (IDA) to obtain a more precise load and displacement capacities from the dynamic behavior. Nevertheless, the outcomes obtained may be used for comparison with those reported in the current study from the pushover analyses. Therefore, the reliability of the pushover analysis at different damage states can be assessed. In addition, the outcomes of the IDA may lead to generate fragility curves of the rammed earth walls. It should be noted that several aspects of the nonlinear time-history analyses of the rammed earth components and buildings are still uncertain, such as the cyclic behavior and the damping ratio.

This page is left blank on purpose.

## REFERENCES

- Allahvirdizadeh, R., Khanmohammadi, M., Marefat, M.S., "Investigating Effects of Scaling and Selecting Earthquake Ground Motions on Performance-Based Design of RC Buildings", *4<sup>th</sup> International Conference on Concrete & Development*, Tehran, Iran, 2013.
- Allahvirdizadeh, R., Gholipour, Y., "Reliability Evaluation of Predicted Structural Performances Using Nonlinear Static Analysis", *Bulletin of Earthquake Engineering*, 15(5), 2129-2148, 2017.
- Ascione, L., de Felice, G., De Santis, S., "A Qualification Method for Externally Bonded Fiber Reinforced Cementitious Matrix (FRCM) Strengthening Systems", *Composites Part B: Engineering*, 78, 497-506, 2015.
- Barroso, C.A., "Reforço Sismico Inovador de Construcao de Taipa", M.Sc. Thesis, University of Minho, Guimarães, Portugal, 2017.
- Basili, M., Marcari, G., Vestroni, F., "Nonlinear Analysis of Masonry Panels Strengthened With Textile Reinforced Mortar", *Engineering Structures*, 113, 245-258, 2016.
- Bui, Q.B., Morel, J.C., "Assessing the anisotropy of rammed earth", *Construction and Building Materials*, 23(9), 3005-3011, 2009.
- Bui, Q.B., Hans, S., Morel, J.C., Do, A.P., "First Exploratory Study on Dynamic Characteristics of Rammed Earth Buildings", *Engineering Structures*, 33, 3690-3695, 2011.
- Bui, T.T., Bui, Q.B., Limam, A., Morel, J.C., "Modeling rammed earth wall using discrete element method", *Continuum Mechanics and Thermodynamics*, 28 (1), 523-538, 2015.
- Candeias, P.X., Costa, A.C., Mendes, N., Costa, A.A., Lourenço, P.B., "Experimental Assessment of the Out-of-Plane Performance of Masonry Buildings through Shaking Table Tests", *International Journal of Architectural Heritage*, 11(1), 31-58, 2016.
- Chopra, A.K., *Dynamics of Structures: Theory and Applications to Earthquake Engineering*, Prentice-Hall Publications, 2012.
- Ciancio, D., Augarde, C., "Capacity of Unreinforced Rammed Earth Walls Subjected to Lateral Wind Force: Elastic Analysis versus Ultimate Strength Analysis", *Materials and Structures*, 46 (9), 1569-1585, 2013.
- Correia, M.R., *Rammed Earth in Alentejo*, ARGUMENTUM, Lisbon, Portugal, 2007.
- Correia, M.R., Varum, H., Lourenço, P.B., *Common damages and recommendations for the seismic retrofitting of vernacular dwellings*, *Seismic Retrofitting: Learning from Vernacular Architecture*, Taylor & Francis Group, London, 2015.

- De Felice, G., Santis, S.D., Garmendia, L., Ghiassi, B., Larrinaga, P., Lourenço, P.B., Oliveira, D.V., Paolacci, F., Papanicolaou, C.G., "Mortar-Based Systems for Externally Bonded Strengthening of Masonry", *Materials and Structures*, 47 (12), 2021-2037, 2014.
- De Sensi, B., Terraccrua, *La Diffusione Dell'architettura Di Terra-Soil*, Dissemination of Earth Architecture, 2003.
- DIANA FEA BV, *Displacement method ANALyser*, Release 10.1, Netherlands, 2017.
- EN 1998-1:2004, *Eurocode 8: Design of Structures for Earthquake Resistance*, European Committee for Standardization, 1998.
- FEMA P695, *Quantification of Buildings Seismic Performance Factors*, Applied Technology Council, Federal Emergency Management Agency, 2009.
- Figueiredo, A., Varum, H., Costa, A., Silveira, D., Oliveira, C., "Seismic Retrofitting Solution of an Adobe Masonry Wall", *Materials and Structures*, 46(1), 203-219, 2013.
- Garofano, A., Ceroni, F., Pecce, M., "Modeling of the In-plane Behavior of Masonry Walls Strengthened with Polymeric Grids Embedded in Cementitious Mortar Layers", *Composites Part B: Engineering*, 85, 243-258, 2016.
- Haselton, C. B. et al., *Evaluation of Ground Motion Selecting and Modification Methods: Predicting Median Inter-story Drift Response of Buildings*, PEER Ground Motion Selection and Modification Working Group, Department of Civil Engineering, California State University, Chico, USA, 2009.
- Houben, H., Guillaud, H., *Earth Construction – a Comprehensive Guide*, CRATerre – EAG, Intermediate Technology Publication, London, 1994.
- ICOMOS Charter, "Principals for the Analysis, Conservation and Structural Restoration of Architectural Heritage", *ICOMOS 14<sup>th</sup> General Assembly*, 2003.
- Jaquin, P.A., Augarde, C.E., Gerrard, C.M., "A chronological description of the spatial development of rammed earth techniques", *International Journal of Architectural Heritage*, 2 (4): 377-400, 2008.
- Librici, C., "Modeling of the Seismic Performance of a Rammed Earth Building", Master Thesis, University of Minho, Guimarães, Portugal, 2016.
- Lilley, D.M., Robinson, J., "Ultimate Strength of Rammed Earth Walls with Openings", *Proceedings of the Institution of Civil Engineers-Structures and Buildings*, 110(3), 278-287, 1995.
- LNEC, <http://www.lnec.pt/organizacao/de/nesde>, 2010.
- Maniatidis, V., Walker, P., *A Review of Rammed Earth Constructions for DTi Partners in Innovative Project "Developing Rammed Earth for UK Housing"*, Natural Building Technology Group, Department of Architecture & Civil Engineering, University of Bath, Bath, 2003.

- Maniatidis, V., Walker, P., Heath, A., Hayward, S., “Mechanical and thermal characteristics of rammed earth”, *Proceeding of international symposium on earthen structures*, Bangalore, India, 2007.
- Mendes, N., “Seismic Assessment of Ancient Masonry Buildings: Shaking Table Tests and Numerical Analysis”, PhD Dissertation, University of Minho, Guimarães, Portugal, 2012.
- Mendes, N., Costa, A.A., Lourenço, P.B., Bento, R., Beyer, K., Felice, G.D., Gams, M., Griffith, M.C., Ingham, J.M., Lagomarsino, S., Lemos, J.V., Liberatore, D., Modena, C., Oliveira, D.V., Penna, A., Sorrentino, L. “Methods and Approaches for Blind Test Predictions of Out-of-Plane Behavior of Masonry Walls: A Numerical Comparative Study”, *International Journal of Architectural Heritage*, 11(1), 59-71, 2017.
- Miccoli, L., Müller, U., Fontana, P., “Mechanical behavior of earthen materials: A comparison between earth block masonry, rammed earth and cob”, *Construction and Building Materials*, 61, 327-339, 2014.
- Miccoli, L., Oliveira, D. V., Silva, R. A., Müller, U., Schueremans, L., “Static Behaviour of rammed earth: experimental testing and finite element modeling”, *Materials and Structures*, 48 (10), 3443-3456, 2015.
- Mininno, G., “Modeling of the behavior of TRM-strengthened masonry walls”, Master Thesis, University of Minho, Guimaraes, Portugal, 2016.
- Minke, G., *Building with Earth-Design and Technology of a Sustainable Architecture*, Birkhäuser – Publisher for Architecture, 2006.
- Mordanova, A., Santis, S.D., de Felice, G., “State-of-the-art Review of Out-of-plane Strengthening of Masonry Walls with Mortar-Based Composites”, *10<sup>th</sup> International Conference on Structural Analysis of Historical Constructions: Anamnesis, Diagnosis, Therapy, Controls (SAHC)*, Leuven, Belgium, 2016.
- Norma Portuguesa, *Eurocódigo 8: Projecto de estruturas para Resistência aos sismos Parte 1: Regras gerais, acções sísmicas e regras para edifícios*, NP EN 1998-1, 2009.
- NZS 4297:1998, *New Zealand Standard: Engineering Design of Earth Buildings*, Standard New Zealand, Wellington, New Zealand, 1998.
- NZS 4298:1998, *New Zealand Standard: Materials and Workmanship for Earth Buildings*, Standard New Zealand, Wellington, New Zealand, 1998.
- Oliveira, D.V., Silva, R.A., Barroso, C., Lourenço, P.B., “Characterization of a Compatible Low Cost Strengthening Solution Based on the TRM Technique for Rammed Earth”, *Key Engineering Materials*, 747, 150-157, 2017.
- Parreira, S.D.J., *Seismic Analysis of a Rammed Earth Building* in Seismic Analysis of a Rammed Earth Building, 2005.

- Schueremans, L., Özlem, C., Janssens, E., Serré, G., Van Balen, K., "Characterization of Repair Mortars for the Assessment of Their Compatibility in Restoration Projects: Research and Practice", *Construction and Building Materials*, 25(12), 4338-4350, 2011.
- Silva, R.A., "Repair of Earth Constructions by Means of Grout Injection", PhD Dissertation, University of Minho, Guimarães, Portugal, 2013.
- Silva, R.A., Oliveira, D.V., Schueremans, L., Lourenco, P.B., Miranda, T., "Modelling the Structural Behaviour of Rammed Earth Components", *Proceedings of the 12<sup>th</sup> International Conference on Computational Structures Technology*, Civil-Comp Press, Stirlingshire, Scotland, 2014a.
- Silva, V., Crowley, H., Varum, H., Pinho, R., "Seismic Hazard and Risk Assessment of Portugal", 2<sup>nd</sup> *European Conference on Earthquake Engineering and Seismology*, Istanbul, Turkey, 2014b.
- Standards Australia, *the Australian earth building handbook*, Standards Australia, Sydney, Australia, 2002.
- SAZS 724:2001 *Rammed Earth Structures*, Standards Association of Zimbabwe, 2001.
- Valluzzi, M.R., Modena, C., Felice, G.D., "Current Practice and Open Issues in Strengthening Historical buildings With Composites", *Materials and Structures*, 47(12), 1971-1985, 2014.
- Wang, Y., Wang, M., Liu, K., Pan, W., Yang, X., "Shaking Table Tests on Seismic Retrofitting of Rammed Earth Structures", *Bulletin of Earthquake Engineering*, 15(3), 1037-1055, 2016.
- Yamin, L.E., Philips, C.A., Reyes, J.C., Ruiz, D.M., "Seismic Behavior and Rehabilitation Alternatives for Adobe and Rammed Earth Buildings", 13<sup>th</sup> *World Conference on Earthquake Engineering*, Vancouver, B.C., Canada, 2004.

## APPENDIX A: OUTCOMES OF MODAL ANALYSIS

Table A 1 - Dynamic properties (20 modes) of the solid unstrengthened in-plane model with 80 cm wing

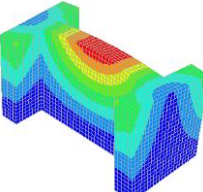
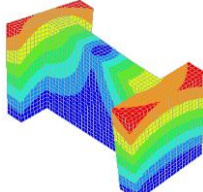
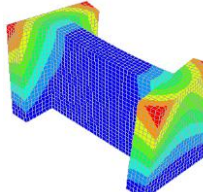
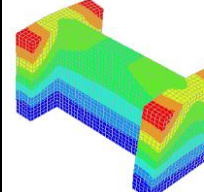
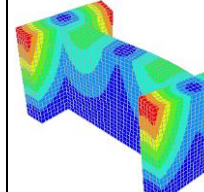
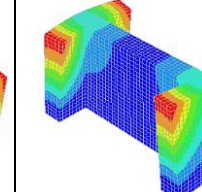
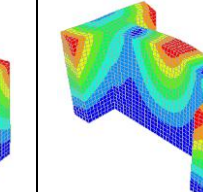
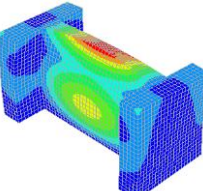
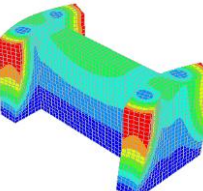
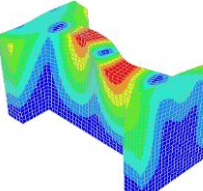
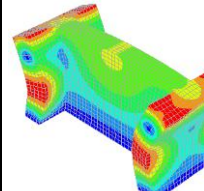
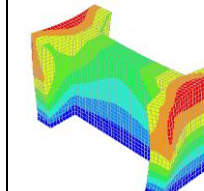
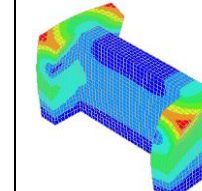
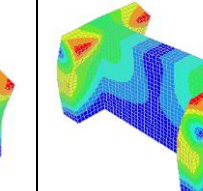
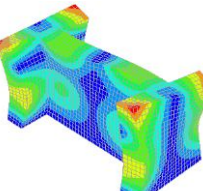
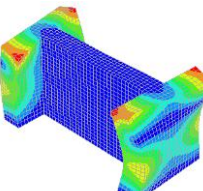
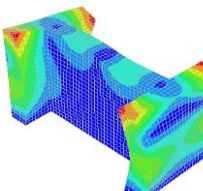
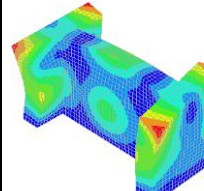
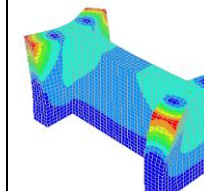
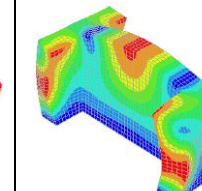
<p><b>Mode 1</b></p>  <p><math>T_1 = 0.0448</math> sec CEM<sub>X</sub> = 0.0% CEM<sub>Y</sub> = 39.6%</p>	<p><b>Mode 2</b></p>  <p><math>T_2 = 0.0316</math> sec CEM<sub>X</sub> = 0.0% CEM<sub>Y</sub> = 39.6%</p>	<p><b>Mode 3</b></p>  <p><math>T_3 = 0.0306</math> sec CEM<sub>X</sub> = 0.0% CEM<sub>Y</sub> = 62.8%</p>	<p><b>Mode 4</b></p>  <p><math>T_4 = 0.0289</math> sec CEM<sub>X</sub> = 69.6% CEM<sub>Y</sub> = 62.8%</p>	<p><b>Mode 5</b></p>  <p><math>T_5 = 0.0283</math> sec CEM<sub>X</sub> = 69.6% CEM<sub>Y</sub> = 62.8%</p>	<p><b>Mode 6</b></p>  <p><math>T_6 = 0.0204</math> sec CEM<sub>X</sub> = 69.6% CEM<sub>Y</sub> = 62.8%</p>	<p><b>Mode 7</b></p>  <p><math>T_7 = 0.0204</math> sec CEM<sub>X</sub> = 69.6% CEM<sub>Y</sub> = 64.1%</p>
<p><b>Mode 8</b></p>  <p><math>T_8 = 0.0135</math> sec CEM<sub>X</sub> = 69.6% CEM<sub>Y</sub> = 75.4%</p>	<p><b>Mode 9</b></p>  <p><math>T_9 = 0.0134</math> sec CEM<sub>X</sub> = 70.6% CEM<sub>Y</sub> = 75.4%</p>	<p><b>Mode 10</b></p>  <p><math>T_{10} = 0.0125</math> sec CEM<sub>X</sub> = 70.6% CEM<sub>Y</sub> = 75.4%</p>	<p><b>Mode 11</b></p>  <p><math>T_{11} = 0.0123</math> sec CEM<sub>X</sub> = 70.6% CEM<sub>Y</sub> = 75.4%</p>	<p><b>Mode 12</b></p>  <p><math>T_{12} = 0.01204</math> sec CEM<sub>X</sub> = 82.3% CEM<sub>Y</sub> = 75.4%</p>	<p><b>Mode 13</b></p>  <p><math>T_{13} = 0.01199</math> sec CEM<sub>X</sub> = 82.3% CEM<sub>Y</sub> = 75.4%</p>	<p><b>Mode 14</b></p>  <p><math>T_{14} = 0.0113</math> sec CEM<sub>X</sub> = 83.1% CEM<sub>Y</sub> = 75.4%</p>
<p><b>Mode 15</b></p>  <p><math>T_{15} = 0.0112</math> sec CEM<sub>X</sub> = 83.1% CEM<sub>Y</sub> = 75.4%</p>	<p><b>Mode 16</b></p>  <p><math>T_{16} = 0.01104</math> sec CEM<sub>X</sub> = 83.1% CEM<sub>Y</sub> = 79.3%</p>	<p><b>Mode 17</b></p>  <p><math>T_{17} = 0.01097</math> sec CEM<sub>X</sub> = 83.1% CEM<sub>Y</sub> = 79.3%</p>	<p><b>Mode 18</b></p>  <p><math>T_{18} = 0.0103</math> sec CEM<sub>X</sub> = 83.1% CEM<sub>Y</sub> = 84.2%</p>	<p><b>Mode 19</b></p>  <p><math>T_{19} = 0.0101</math> sec CEM<sub>X</sub> = 83.1% CEM<sub>Y</sub> = 84.2%</p>	<p><b>Mode 20</b></p>  <p><math>T_{20} = 0.0095</math> sec CEM<sub>X</sub> = 83.1% CEM<sub>Y</sub> = 84.2%</p>	



Table A 2 - Dynamic properties (20 modes) of the solid unstrengthened in-plane model with 50 cm wing

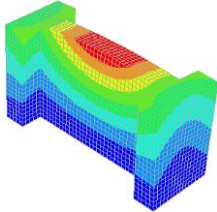
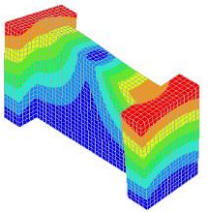
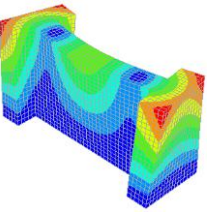
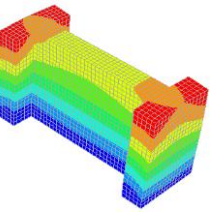
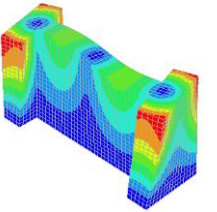
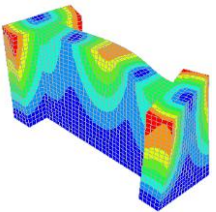
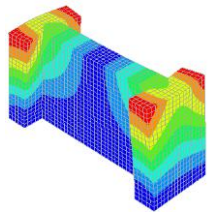
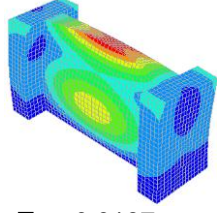
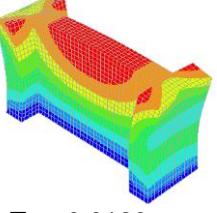
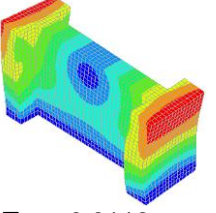
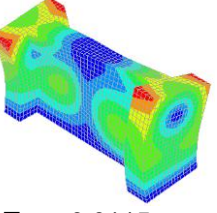
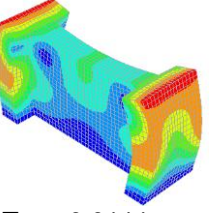
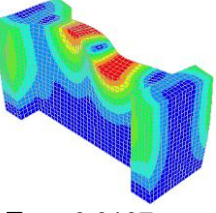
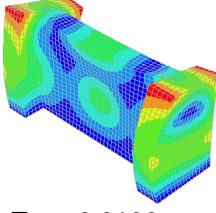
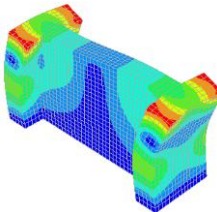
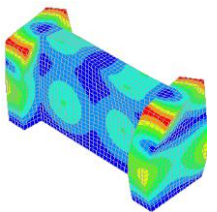
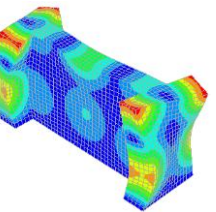
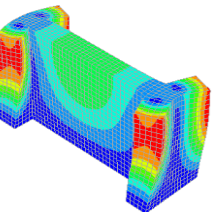
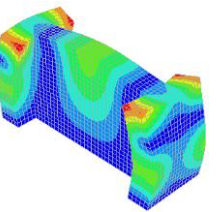
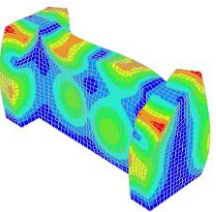
<p><b>Mode 1</b></p>  <p><math>T_1 = 0.0502</math> sec  <math>CEM_x = 0.0\%</math>  <math>CEM_y = 55.8\%</math></p>	<p><b>Mode 2</b></p>  <p><math>T_2 = 0.0375</math> sec  <math>CEM_x = 0.0\%</math>  <math>CEM_y = 55.8\%</math></p>	<p><b>Mode 3</b></p>  <p><math>T_3 = 0.0304</math> sec  <math>CEM_x = 0.0\%</math>  <math>CEM_y = 62.5\%</math></p>	<p><b>Mode 4</b></p>  <p><math>T_4 = 0.0261</math> sec  <math>CEM_x = 72.2\%</math>  <math>CEM_y = 62.5\%</math></p>	<p><b>Mode 5</b></p>  <p><math>T_5 = 0.0220</math> sec  <math>CEM_x = 72.2\%</math>  <math>CEM_y = 62.5\%</math></p>	<p><b>Mode 6</b></p>  <p><math>T_6 = 0.0159</math> sec  <math>CEM_x = 72.2\%</math>  <math>CEM_y = 62.5\%</math></p>	<p><b>Mode 7</b></p>  <p><math>T_7 = 0.0158</math> sec  <math>CEM_x = 72.2\%</math>  <math>CEM_y = 62.5\%</math></p>
<p><b>Mode 8</b></p>  <p><math>T_8 = 0.0137</math> sec  <math>CEM_x = 72.2\%</math>  <math>CEM_y = 77.6\%</math></p>	<p><b>Mode 9</b></p>  <p><math>T_9 = 0.0120</math> sec  <math>CEM_x = 72.2\%</math>  <math>CEM_y = 77.6\%</math></p>	<p><b>Mode 10</b></p>  <p><math>T_{10} = 0.0118</math> sec  <math>CEM_x = 78.6\%</math>  <math>CEM_y = 77.6\%</math></p>	<p><b>Mode 11</b></p>  <p><math>T_{11} = 0.0115</math> sec  <math>CEM_x = 78.6\%</math>  <math>CEM_y = 77.6\%</math></p>	<p><b>Mode 12</b></p>  <p><math>T_{12} = 0.0111</math> sec  <math>CEM_x = 78.6\%</math>  <math>CEM_y = 77.6\%</math></p>	<p><b>Mode 13</b></p>  <p><math>T_{13} = 0.0107</math> sec  <math>CEM_x = 78.6\%</math>  <math>CEM_y = 77.6\%</math></p>	<p><b>Mode 14</b></p>  <p><math>T_{14} = 0.0106</math> sec  <math>CEM_x = 78.6\%</math>  <math>CEM_y = 84.0\%</math></p>
<p><b>Mode 15</b></p>  <p><math>T_{15} = 0.0100</math> sec  <math>CEM_x = 83.5\%</math>  <math>CEM_y = 84.0\%</math></p>	<p><b>Mode 16</b></p>  <p><math>T_{16} = 0.0094</math> sec  <math>CEM_x = 83.5\%</math>  <math>CEM_y = 84.1\%</math></p>	<p><b>Mode 17</b></p>  <p><math>T_{17} = 0.0087</math> sec  <math>CEM_x = 83.5\%</math>  <math>CEM_y = 84.1\%</math></p>	<p><b>Mode 18</b></p>  <p><math>T_{18} = 0.0087</math> sec  <math>CEM_x = 84.2\%</math>  <math>CEM_y = 84.1\%</math></p>	<p><b>Mode 19</b></p>  <p><math>T_{19} = 0.0084</math> sec  <math>CEM_x = 84.2\%</math>  <math>CEM_y = 84.1\%</math></p>	<p><b>Mode 20</b></p>  <p><math>T_{20} = 0.0077</math> sec  <math>CEM_x = 84.2\%</math>  <math>CEM_y = 84.1\%</math></p>	

Table A 3 - Dynamic properties (20 modes) of the solid unstrengthened out-of-plane model

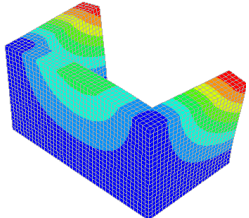
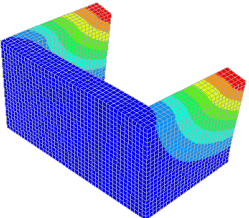
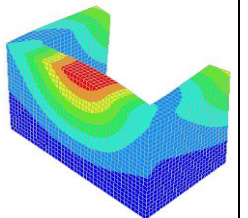
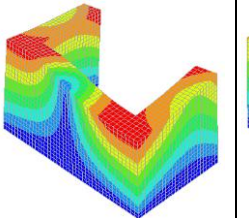
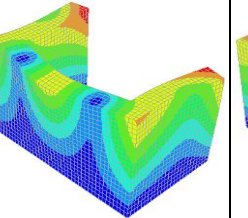
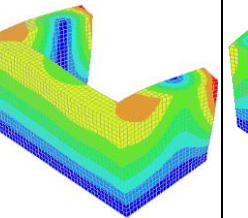
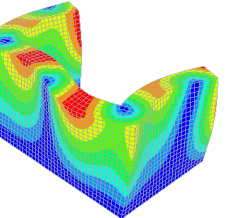
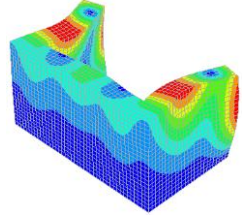
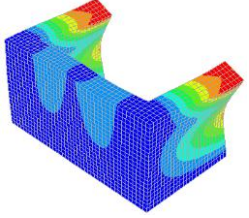
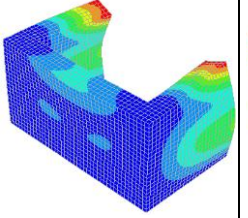
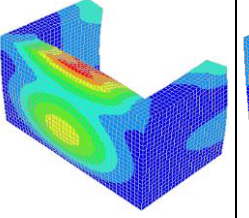
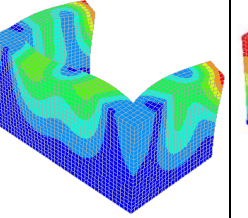
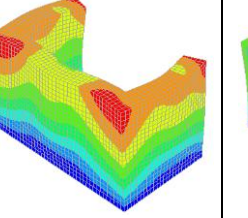
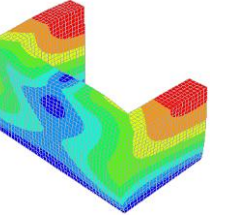
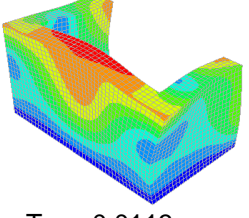
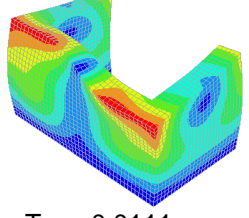
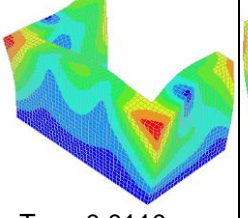
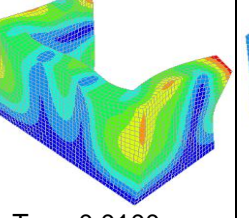
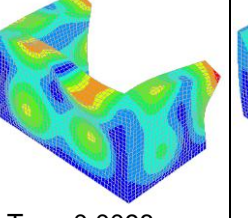
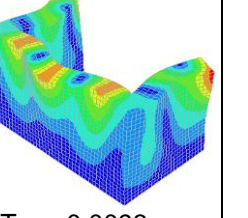
<p><b>Mode 1</b></p>  <p><math>T_1 = 0.0544</math> sec CEM<sub>X</sub> = 0.0% CEM<sub>Y</sub> = 4.4%</p>	<p><b>Mode 2</b></p>  <p><math>T_2 = 0.0518</math> sec CEM<sub>X</sub> = 32.1% CEM<sub>Y</sub> = 4.4%</p>	<p><b>Mode 3</b></p>  <p><math>T_3 = 0.0390</math> sec CEM<sub>X</sub> = 32.1% CEM<sub>Y</sub> = 44.4%</p>	<p><b>Mode 4</b></p>  <p><math>T_4 = 0.0292</math> sec CEM<sub>X</sub> = 36.5% CEM<sub>Y</sub> = 44.4%</p>	<p><b>Mode 5</b></p>  <p><math>T_5 = 0.0243</math> sec CEM<sub>X</sub> = 36.5% CEM<sub>Y</sub> = 65.8%</p>	<p><b>Mode 6</b></p>  <p><math>T_6 = 0.0232</math> sec CEM<sub>X</sub> = 65.3% CEM<sub>Y</sub> = 65.8%</p>	<p><b>Mode 7</b></p>  <p><math>T_7 = 0.0173</math> sec CEM<sub>X</sub> = 69.8% CEM<sub>Y</sub> = 65.8%</p>
<p><b>Mode 8</b></p>  <p><math>T_8 = 0.0171</math> sec CEM<sub>X</sub> = 69.8% CEM<sub>Y</sub> = 66.7%</p>	<p><b>Mode 9</b></p>  <p><math>T_9 = 0.0147</math> sec CEM<sub>X</sub> = 78.1% CEM<sub>Y</sub> = 66.7%</p>	<p><b>Mode 10</b></p>  <p><math>T_{10} = 0.0145</math> sec CEM<sub>X</sub> = 78.1% CEM<sub>Y</sub> = 67.3%</p>	<p><b>Mode 11</b></p>  <p><math>T_{11} = 0.0136</math> sec CEM<sub>X</sub> = 78.1% CEM<sub>Y</sub> = 75.8%</p>	<p><b>Mode 12</b></p>  <p><math>T_{12} = 0.0125</math> sec CEM<sub>X</sub> = 78.1% CEM<sub>Y</sub> = 75.8%</p>	<p><b>Mode 13</b></p>  <p><math>T_{13} = 0.0122</math> sec CEM<sub>X</sub> = 78.1% CEM<sub>Y</sub> = 75.9%</p>	<p><b>Mode 14</b></p>  <p><math>T_{14} = 0.0119</math> sec CEM<sub>X</sub> = 79.5% CEM<sub>Y</sub> = 75.9%</p>
<p><b>Mode 15</b></p>  <p><math>T_{15} = 0.0113</math> sec CEM<sub>X</sub> = 79.5% CEM<sub>Y</sub> = 77.4%</p>	<p><b>Mode 16</b></p>  <p><math>T_{16} = 0.0111</math> sec CEM<sub>X</sub> = 81.2% CEM<sub>Y</sub> = 77.4%</p>	<p><b>Mode 17</b></p>  <p><math>T_{17} = 0.0110</math> sec CEM<sub>X</sub> = 81.2% CEM<sub>Y</sub> = 82.7%</p>	<p><b>Mode 18</b></p>  <p><math>T_{18} = 0.0100</math> sec CEM<sub>X</sub> = 81.2% CEM<sub>Y</sub> = 82.7%</p>	<p><b>Mode 19</b></p>  <p><math>T_{19} = 0.0098</math> sec CEM<sub>X</sub> = 81.8% CEM<sub>Y</sub> = 82.7%</p>	<p><b>Mode 20</b></p>  <p><math>T_{20} = 0.0093</math> sec CEM<sub>X</sub> = 81.8% CEM<sub>Y</sub> = 83.1%</p>	

Table A 4 - Dynamic properties (20 modes) of the shell unstrengthened in-plane model with 80 cm wing

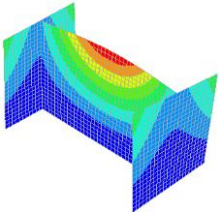
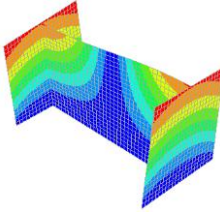
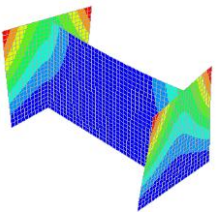
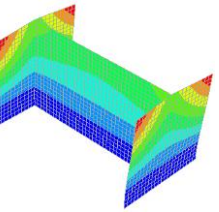
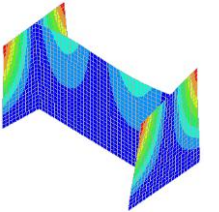
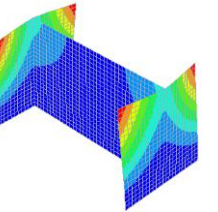
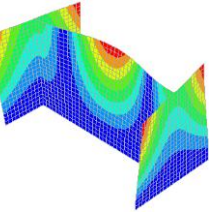
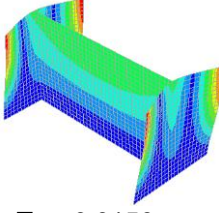
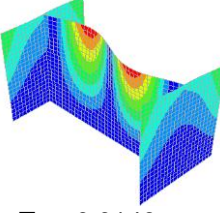
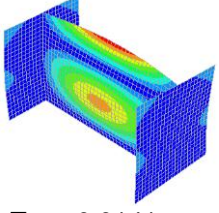
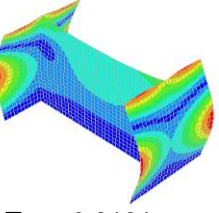
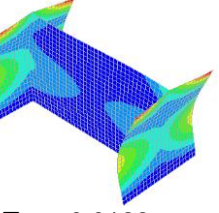
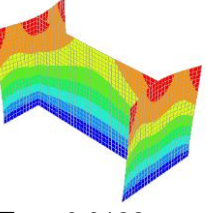
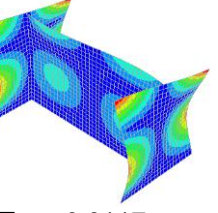
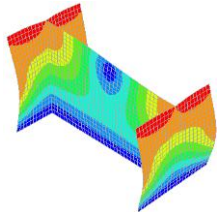
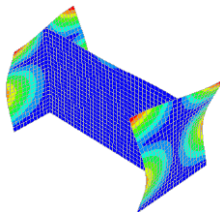
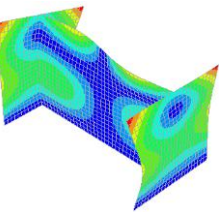
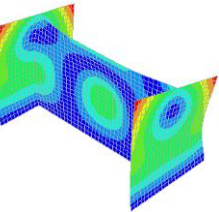
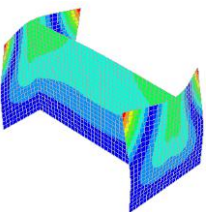
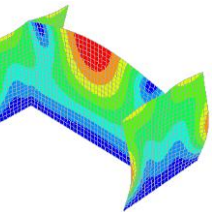
<p><b>Mode 1</b></p>  <p><math>T_1 = 0.0479</math> sec CEM<sub>x</sub> = 0.0% CEM<sub>y</sub> = 40.1%</p>	<p><b>Mode 2</b></p>  <p><math>T_2 = 0.0328</math> sec CEM<sub>x</sub> = 0.0 % CEM<sub>y</sub> = 40.1 %</p>	<p><b>Mode 3</b></p>  <p><math>T_3 = 0.0318</math> sec CEM<sub>x</sub> = 0.0 % CEM<sub>y</sub> = 61.1 %</p>	<p><b>Mode 4</b></p>  <p><math>T_4 = 0.0313</math> sec CEM<sub>x</sub> = 67.2 % CEM<sub>y</sub> = 61.1 %</p>	<p><b>Mode 5</b></p>  <p><math>T_5 = 0.0306</math> sec CEM<sub>x</sub> = 67.2 % CEM<sub>y</sub> = 61.1 %</p>	<p><b>Mode 6</b></p>  <p><math>T_6 = 0.0235</math> sec CEM<sub>x</sub> = 67.2 % CEM<sub>y</sub> = 61.1 %</p>	<p><b>Mode 7</b></p>  <p><math>T_7 = 0.0232</math> sec CEM<sub>x</sub> = 67.2 % CEM<sub>y</sub> = 64.1 %</p>
<p><b>Mode 8</b></p>  <p><math>T_8 = 0.0150</math> sec CEM<sub>x</sub> = 70.4 % CEM<sub>y</sub> = 64.1 %</p>	<p><b>Mode 9</b></p>  <p><math>T_9 = 0.0146</math> sec CEM<sub>x</sub> = 70.4 % CEM<sub>y</sub> = 64.1 %</p>	<p><b>Mode 10</b></p>  <p><math>T_{10} = 0.0141</math> sec CEM<sub>x</sub> = 70.4 % CEM<sub>y</sub> = 75.3 %</p>	<p><b>Mode 11</b></p>  <p><math>T_{11} = 0.0131</math> sec CEM<sub>x</sub> = 70.4 % CEM<sub>y</sub> = 75.3 %</p>	<p><b>Mode 12</b></p>  <p><math>T_{12} = 0.0128</math> sec CEM<sub>x</sub> = 82.3 % CEM<sub>y</sub> = 75.3 %</p>	<p><b>Mode 13</b></p>  <p><math>T_{13} = 0.0122</math> sec CEM<sub>x</sub> = 82.3 % CEM<sub>y</sub> = 75.3 %</p>	<p><b>Mode 14</b></p>  <p><math>T_{14} = 0.0117</math> sec CEM<sub>x</sub> = 82.3 % CEM<sub>y</sub> = 75.3 %</p>
<p><b>Mode 15</b></p>  <p><math>T_{15} = 0.0117</math> sec CEM<sub>x</sub> = 82.7 % CEM<sub>y</sub> = 75.3 %</p>	<p><b>Mode 16</b></p>  <p><math>T_{16} = 0.0116</math> sec CEM<sub>x</sub> = 82.7 % CEM<sub>y</sub> = 76.2 %</p>	<p><b>Mode 17</b></p>  <p><math>T_{17} = 0.0114</math> sec CEM<sub>x</sub> = 82.7 % CEM<sub>y</sub> = 76.2 %</p>	<p><b>Mode 18</b></p>  <p><math>T_{18} = 0.0108</math> sec CEM<sub>x</sub> = 82.7 % CEM<sub>y</sub> = 83.7 %</p>	<p><b>Mode 19</b></p>  <p><math>T_{19} = 0.0107</math> sec CEM<sub>x</sub> = 82.7 % CEM<sub>y</sub> = 83.7 %</p>	<p><b>Mode 20</b></p>  <p><math>T_{20} = 0.0101</math> sec CEM<sub>x</sub> = 82.7 % CEM<sub>y</sub> = 83.7 %</p>	

Table A 5 - Dynamic properties (20 modes) of the shell unstrengthened in-plane model with 50 cm wing

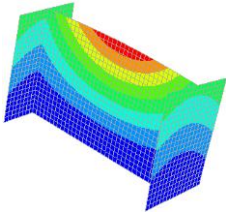
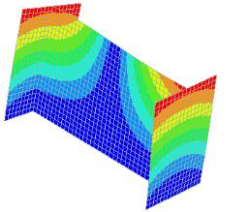
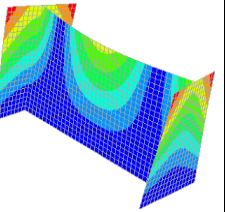
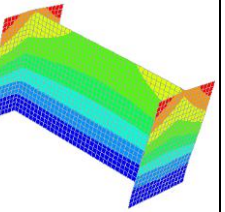
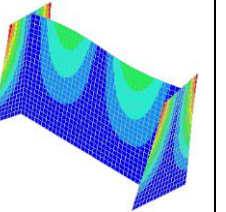
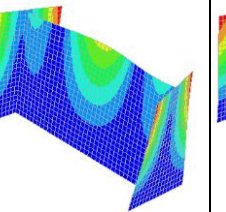
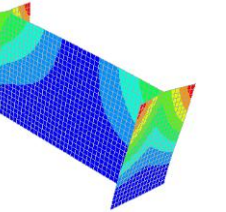
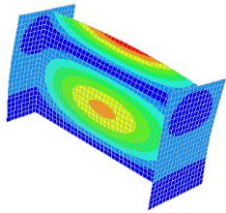
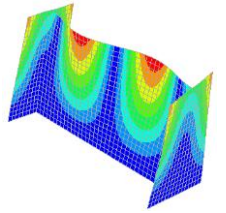
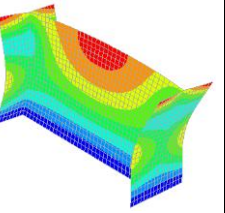
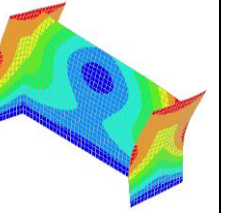
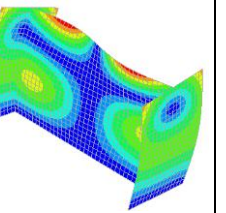
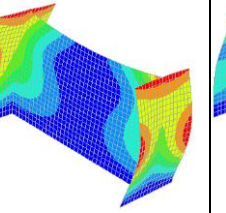
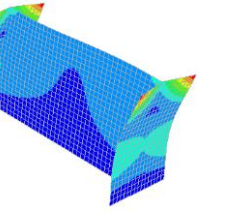
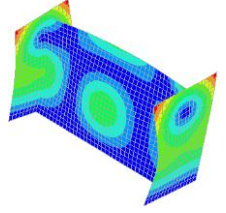
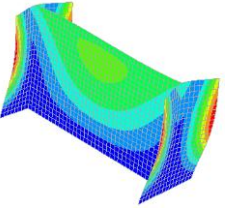
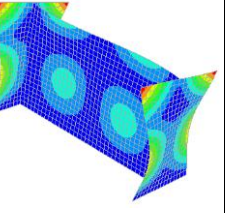
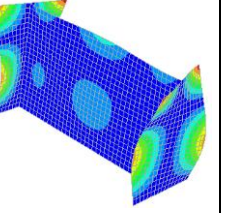
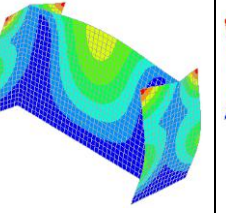
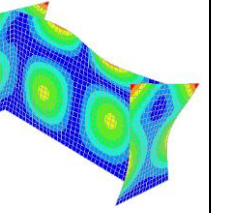
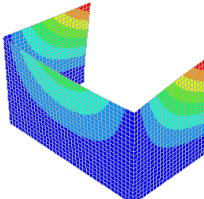
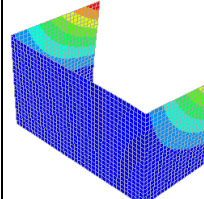
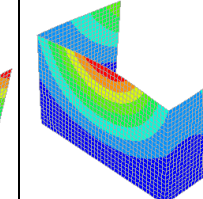
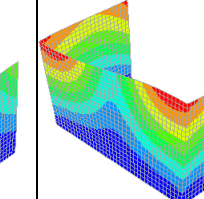
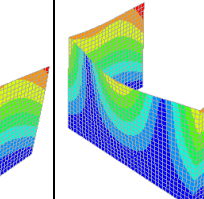
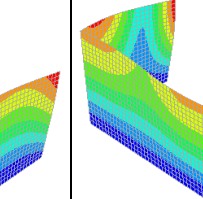
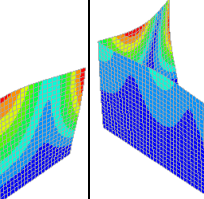
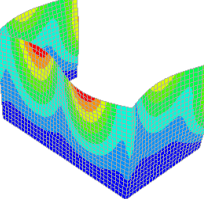
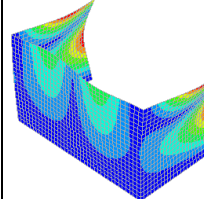
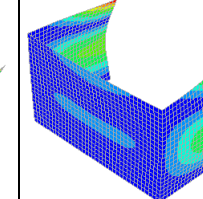
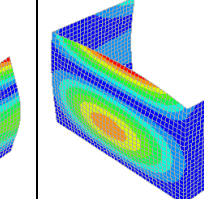
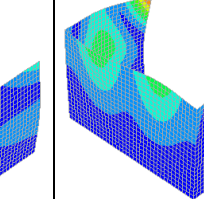
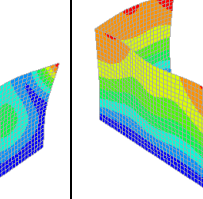
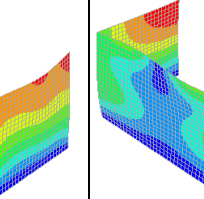
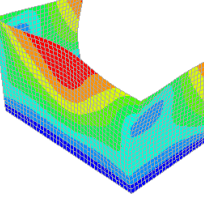
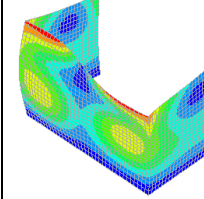
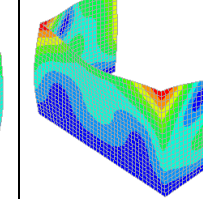
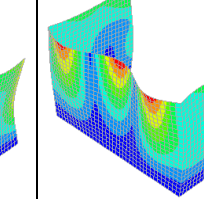
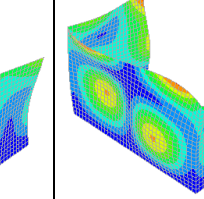
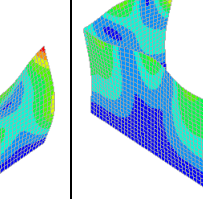
<p><b>Mode 1</b></p>  <p><math>T_1 = 0.0533</math> sec CEM<sub>x</sub> = 0.0% CEM<sub>y</sub> = 54.7%</p>	<p><b>Mode 2</b></p>  <p><math>T_2 = 0.0391</math> sec CEM<sub>x</sub> = 0.0 % CEM<sub>y</sub> = 54.7 %</p>	<p><b>Mode 3</b></p>  <p><math>T_3 = 0.0316</math> sec CEM<sub>x</sub> = 0.0 % CEM<sub>y</sub> = 62.7 %</p>	<p><b>Mode 4</b></p>  <p><math>T_4 = 0.0280</math> sec CEM<sub>x</sub> = 71.1 % CEM<sub>y</sub> = 62.7 %</p>	<p><b>Mode 5</b></p>  <p><math>T_5 = 0.0236</math> sec CEM<sub>x</sub> = 71.1 % CEM<sub>y</sub> = 62.7 %</p>	<p><b>Mode 6</b></p>  <p><math>T_6 = 0.0186</math> sec CEM<sub>x</sub> = 71.1 % CEM<sub>y</sub> = 62.7 %</p>	<p><b>Mode 7</b></p>  <p><math>T_7 = 0.0181</math> sec CEM<sub>x</sub> = 71.1 % CEM<sub>y</sub> = 62.7 %</p>
<p><b>Mode 8</b></p>  <p><math>T_8 = 0.0143</math> sec CEM<sub>x</sub> = 71.1 % CEM<sub>y</sub> = 77.2 %</p>	<p><b>Mode 9</b></p>  <p><math>T_9 = 0.0133</math> sec CEM<sub>x</sub> = 71.1 % CEM<sub>y</sub> = 77.2 %</p>	<p><b>Mode 10</b></p>  <p><math>T_{10} = 0.0122</math> sec CEM<sub>x</sub> = 71.1 % CEM<sub>y</sub> = 77.2 %</p>	<p><b>Mode 11</b></p>  <p><math>T_{11} = 0.0120</math> sec CEM<sub>x</sub> = 78.0 % CEM<sub>y</sub> = 77.2 %</p>	<p><b>Mode 12</b></p>  <p><math>T_{12} = 0.0118</math> sec CEM<sub>x</sub> = 78.0 % CEM<sub>y</sub> = 77.2 %</p>	<p><b>Mode 13</b></p>  <p><math>T_{13} = 0.0117</math> sec CEM<sub>x</sub> = 78.0 % CEM<sub>y</sub> = 77.2 %</p>	<p><b>Mode 14</b></p>  <p><math>T_{14} = 0.0112</math> sec CEM<sub>x</sub> = 82.7 % CEM<sub>y</sub> = 77.2 %</p>
<p><b>Mode 15</b></p>  <p><math>T_{15} = 0.0109</math> sec CEM<sub>x</sub> = 82.7 % CEM<sub>y</sub> = 83.7 %</p>	<p><b>Mode 16</b></p>  <p><math>T_{16} = 0.0105</math> sec CEM<sub>x</sub> = 83.5 % CEM<sub>y</sub> = 83.7 %</p>	<p><b>Mode 17</b></p>  <p><math>T_{17} = 0.0100</math> sec CEM<sub>x</sub> = 83.5 % CEM<sub>y</sub> = 83.7 %</p>	<p><b>Mode 18</b></p>  <p><math>T_{18} = 0.0096</math> sec CEM<sub>x</sub> = 83.5 % CEM<sub>y</sub> = 83.8 %</p>	<p><b>Mode 19</b></p>  <p><math>T_{19} = 0.0094</math> sec CEM<sub>x</sub> = 83.5 % CEM<sub>y</sub> = 83.8 %</p>	<p><b>Mode 20</b></p>  <p><math>T_{20} = 0.0088</math> sec CEM<sub>x</sub> = 83.5 % CEM<sub>y</sub> = 83.8 %</p>	

Table A 6 - Dynamic properties (20 modes) of the shell unstrengthened out-of-plane model

<p><b>Mode 1</b></p>  <p><math>T_1 = 0.071</math> sec CEM<sub>x</sub> = 0.0% CEM<sub>y</sub> = 5.1%</p>	<p><b>Mode 2</b></p>  <p><math>T_2 = 0.0546</math> sec CEM<sub>x</sub> = 33.4 % CEM<sub>y</sub> = 5.1 %</p>	<p><b>Mode 3</b></p>  <p><math>T_3 = 0.0422</math> sec CEM<sub>x</sub> = 37.5 % CEM<sub>y</sub> = 42.6 %</p>	<p><b>Mode 4</b></p>  <p><math>T_4 = 0.0302</math> sec CEM<sub>x</sub> = 37.5 % CEM<sub>y</sub> = 42.6 %</p>	<p><b>Mode 5</b></p>  <p><math>T_5 = 0.0248</math> sec CEM<sub>x</sub> = 37.5 % CEM<sub>y</sub> = 65.6 %</p>	<p><b>Mode 6</b></p>  <p><math>T_6 = 0.0239</math> sec CEM<sub>x</sub> = 63.5 % CEM<sub>y</sub> = 65.6 %</p>	<p><b>Mode 7</b></p>  <p><math>T_7 = 0.0182</math> sec CEM<sub>x</sub> = 63.5 % CEM<sub>y</sub> = 66.4 %</p>
<p><b>Mode 8</b></p>  <p><math>T_8 = 0.0175</math> sec CEM<sub>x</sub> = 69.0 % CEM<sub>y</sub> = 66.4 %</p>	<p><b>Mode 9</b></p>  <p><math>T_9 = 0.0152</math> sec CEM<sub>x</sub> = 78.0 % CEM<sub>y</sub> = 66.4 %</p>	<p><b>Mode 10</b></p>  <p><math>T_{10} = 0.0149</math> sec CEM<sub>x</sub> = 78.0 % CEM<sub>y</sub> = 66.9 %</p>	<p><b>Mode 11</b></p>  <p><math>T_{11} = 0.0142</math> sec CEM<sub>x</sub> = 78.0 % CEM<sub>y</sub> = 75.9 %</p>	<p><b>Mode 12</b></p>  <p><math>T_{12} = 0.0139</math> sec CEM<sub>x</sub> = 78.4 % CEM<sub>y</sub> = 75.9 %</p>	<p><b>Mode 13</b></p>  <p><math>T_{13} = 0.0122</math> sec CEM<sub>x</sub> = 78.4 % CEM<sub>y</sub> = 75.9 %</p>	<p><b>Mode 14</b></p>  <p><math>T_{14} = 0.0119</math> sec CEM<sub>x</sub> = 79.4 % CEM<sub>y</sub> = 75.9 %</p>
<p><b>Mode 15</b></p>  <p><math>T_{15} = 0.0114</math> sec CEM<sub>x</sub> = 79.4 % CEM<sub>y</sub> = 77.8 %</p>	<p><b>Mode 16</b></p>  <p><math>T_{16} = 0.0114</math> sec CEM<sub>x</sub> = 81.3 % CEM<sub>y</sub> = 77.8 %</p>	<p><b>Mode 17</b></p>  <p><math>T_{17} = 0.0110</math> sec CEM<sub>x</sub> = 81.3 % CEM<sub>y</sub> = 81.8 %</p>	<p><b>Mode 18</b></p>  <p><math>T_{18} = 0.0103</math> sec CEM<sub>x</sub> = 81.3 % CEM<sub>y</sub> = 81.8 %</p>	<p><b>Mode 19</b></p>  <p><math>T_{19} = 0.0102</math> sec CEM<sub>x</sub> = 82.0 % CEM<sub>y</sub> = 81.8 %</p>	<p><b>Mode 20</b></p>  <p><math>T_{20} = 0.0098</math> sec CEM<sub>x</sub> = 82.0 % CEM<sub>y</sub> = 82.6 %</p>	

## APPENDIX B

### OUTCOMES OF PUSHOVER ANALYSES

This appendix includes the contour maps of the principal tensile strains of the solid models from different views at their peak capacities obtained from the pushover analyses.

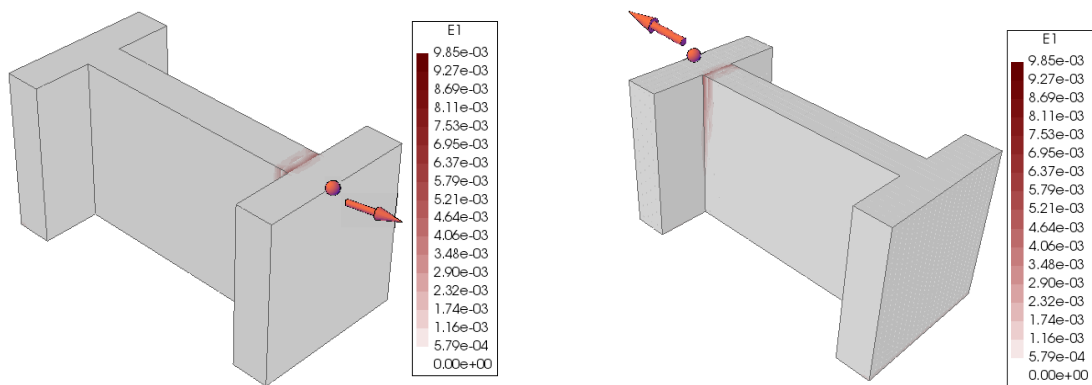


Figure B 1 – Principal tensile strains of the solid unstrengthened in-plane model with 80 cm wing at its peak capacity from different views

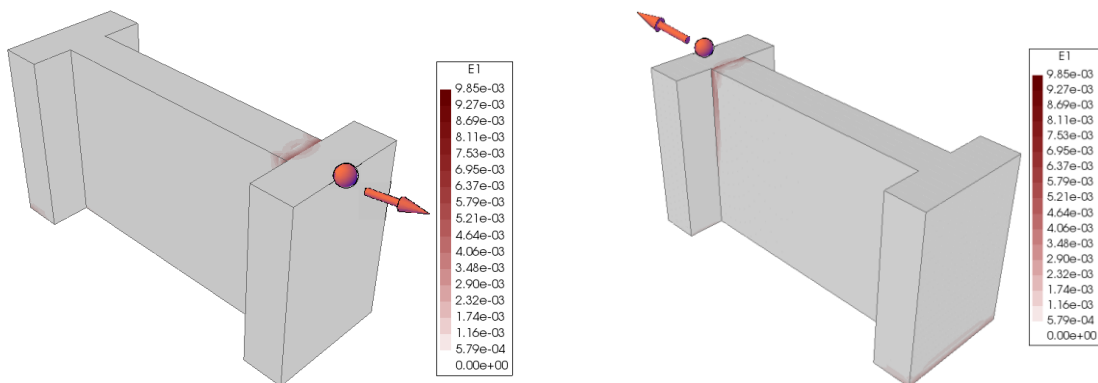


Figure B 2- Different views of the principal tensile strains of the solid in-plane unstrengthened model with 50 cm wing at its peak capacity

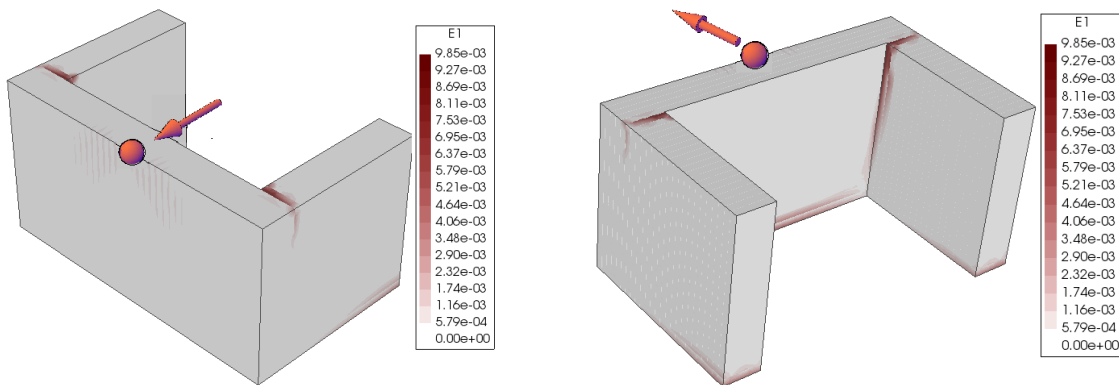


Figure B 3- Different views of the principal tensile strains of the solid out-of-plane unstrengthened model pushed in the negative direction

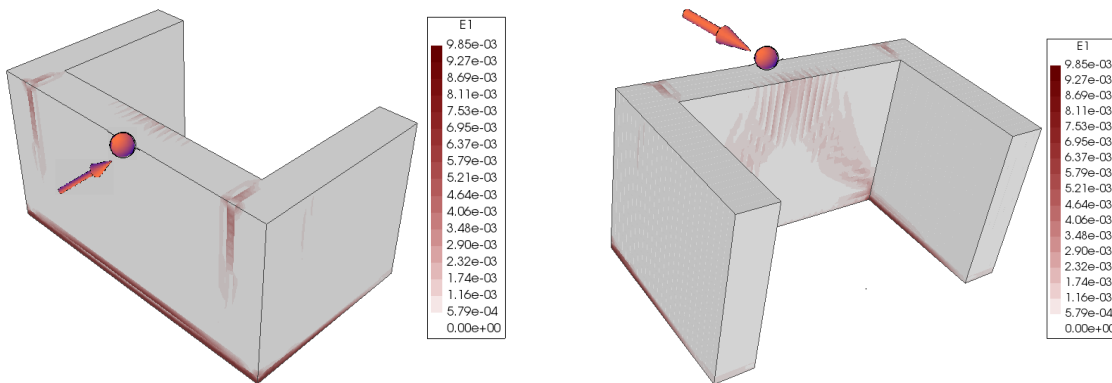


Figure B 4- Different views of the principal tensile strains of the solid out-of-plane unstrengthened model pushed in the positive direction

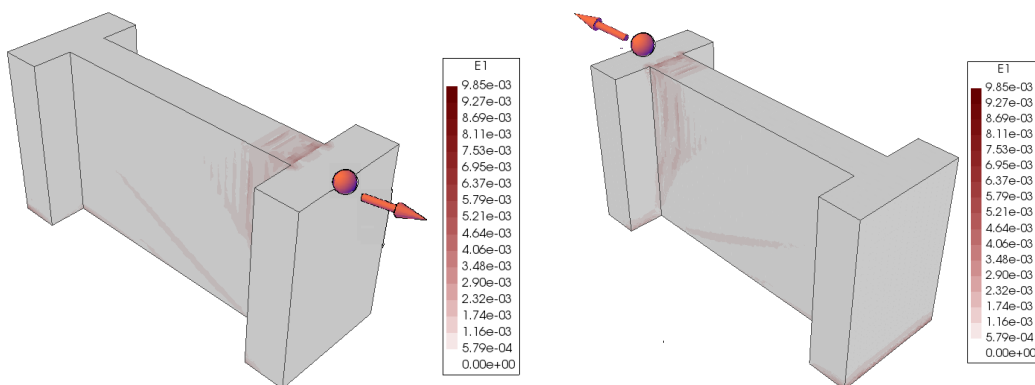


Figure B 5- Different views of the principal tensile strains of the solid in-plane strengthened model with 50 cm wing at its peak capacity

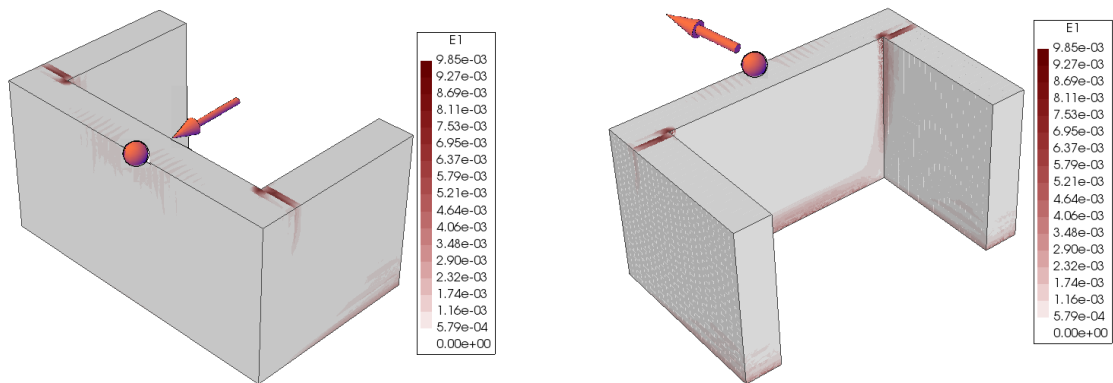


Figure B 6- Different views of the principal tensile strains of the solid out-of-plane strengthened model pushed in the negative direction

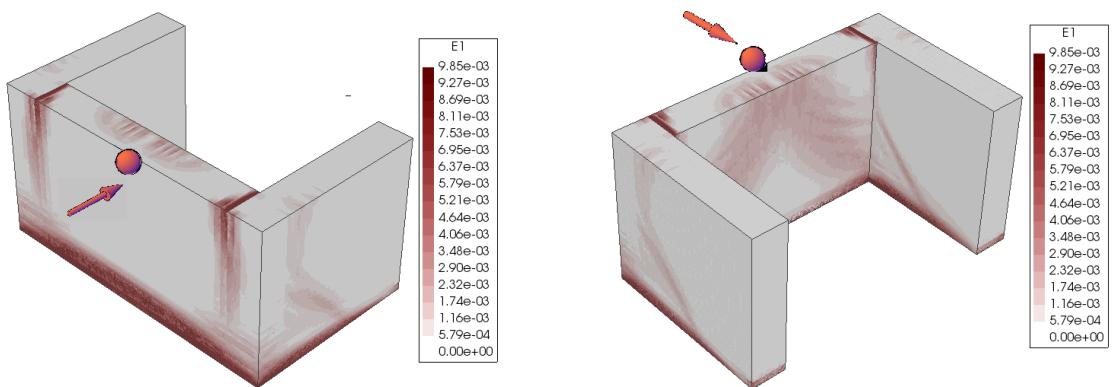


Figure B 7- Different views of the principal tensile strains of the solid out-of-plane strengthened model pushed in the positive direction